

AN ABSTRACT OF A THESIS

PERFORMANCE ANALYSIS AND NONLINEAR FEEDBACK CONTROL OF INTERIOR PERMANENT MAGNET SYNCHRONOUS MOTOR

Olufemi A. Osaloni

Masters of Science in Electrical Engineering

A two horsepower interior permanent magnet (IPM) synchronous machine was used in the modeling, analysis, and nonlinear controller technique implementation in this research. This thesis presents an accurate model of the interior permanent magnet synchronous machine, which considers iron-loss resistance in parallel with the inductance of the machine to account for the core loss. The q-d equivalent circuits with shunt iron-loss resistance are given. The influence of magnetic saturation and armature reaction on the performance of the interior permanent magnet synchronous machine was investigated by simulations and experiments. Ansoft's RMxprt was found to be an excellent tool for the finite element analysis of the machine. The parameters of the machine were validated with result obtained experimentally by using this software.

Different fault conditions for star- and delta-connected stator windings of the IPM and induction motor were investigated both experimentally (for feasible faults) and simulation using Matlab (Simulink). The faults considered are those which occur either at the terminal of the machine or in the winding of the machine. The necessary conditions for different faults were derived; dynamic simulations and some experimental results are used to show the response of the machines during faults. The fault tolerance of these machines were studied for different fault conditions.

For continuous operation, reconfiguration of the modulation scheme of the VSI-PWM when one inverter phase leg is damaged was derived. The faulted leg is replaced with a split dc capacitor once fault in one of the phase legs is detected and the modulation scheme is reconfigure for this topology. By this scheme, the reliability of the system is improved. Simulation results are used to confirm this scheme for different speed of operation.

The principles of nonlinear control input-output linearization with decoupling are used to design the controllers for speed (or torque) control of the IPM with minimization of the total loss along the line. The machine was modeled with the inclusion of iron loss resistance to account for the iron loss in the machine; by this, the total loss comprising the copper loss and iron loss are being minimized as one of the objectives and speed (or torque) as the other objective to be controlled. Simulation results show some improvement in the performance of the machine when compared to the torque per ampere operation. Experimental results are expected to confirm same results.

**PERFORMANCE ANALYSIS AND NONLINEAR FEEDBACK CONTROL OF
INTERIOR PERMANENT MAGNET SYNCHRONOUS MOTOR**

A Thesis

Presented to

The Faculty of the Graduate School

Tennessee Technological University

By

Olufemi A. Osaloni

In Partial Fulfillment

Of the Requirements for the Degree

MASTER OF SCIENCE

Electrical Engineering

August 2003

CERTIFICATE OF APPROVAL OF THESIS

**PERFORMANCE ANALYSIS AND NONLINEAR FEEDBACK CONTROL OF
INTERIOR PERMANENT MAGNET SYNCHRONOUS MOTOR**

By

Olufemi A. Osaloni

Graduate Advisory Committee:

Chairperson

Date

Member

Date

Member

Date

Approved for the Faculty:

Associate Vice President for Research
and Graduate Studies

Date

STATEMENT OF PERMISSION TO USE

In presenting this thesis in partial fulfillment of the requirements for a Master of Science degree at Tennessee Technological University, I agree that the University Library shall make it available to borrowers under rules of the Library. Brief quotations from this thesis are allowable without special permission, provided that accurate acknowledgement of the source is made.

My major professor may grant permission for extensive quotation from or reproduction of this thesis when the proposed use of the material is for scholarly purposes. Any copying or use of the material in this thesis for financial gain shall not be allowed without my written permission.

Signature _____

Date _____

DEDICATION

This Thesis is dedicated to

God

and to my parents

Festus

and

Deborah

ACKNOWLEDGEMENTS

I would like to express my appreciation to Dr. Joseph Olorunfemi Ojo, my major professor and chairman of the advisory committee, for his valuable direction and assistance. Most of all, I would like to thank him for giving me the opportunity to pursue a graduate degree.

I would like to thank Dr. Mike Omoigui for his fatherly role in my academic work, and being my motivator in my decision to pursue my graduate program.

I would also like to thank Dr. Prit Chowdhuri and Dr. Gadir. Radman for their willingness to be on my advisory committee.

I would also like to thank my folks and my fiancée, Olaide Komolafe, for their love, constant encouragement, and support throughout my academic career. I would like to thank all my friends for their help and support. My debt of gratitude to the almighty, who has been my fortress in all my endeavours.

I acknowledge the financial support of the Centre for Electric Power at Tennessee Technological University for the assistantship given in pursuit of my Masters degree program.

TABLE OF CONTENTS

	Page
LIST OF TABLES.....	x
LIST OF FIGURES	xi
CHAPTER 1	1
INTRODUCTION	1
1.1. Introduction.....	1
1.2. Literature Review.....	4
1.3. Research Motivation.....	12
1.4. Scope of Work	14
CHAPTER 2	18
INTERIOR PERMANENT MAGNET MACHINE UNDER VARIOUS FAULTS.....	18
2.1. Introduction.....	18
2.2. Derivation of Machine Equations	19
2.3. Delta-Connected Stator.....	26
2.4. Fault Analysis using Stationary Reference Frame Unbalance in Delta- Connected IPMSM.....	29
2.4.1 Supply Line “A” Open-Circuit Response.....	29
2.4.2 Stator Phase “A” Open-Circuit Response.....	34
2.4.3 Shorted Stator Phase “A” Open-Circuit Response	37
2.5. Star-Connected Stator	40

2.6	Fault Analysis using Stationary Reference Frame Unbalance in Star-Connected IPMSM.....	43
2.6.1	Supply Line “A” Open-Circuit Response	43
2.6.2	Supply Line-to-Line Fault Response	47
2.6.3	Shorted Stator Phases.....	48
CHAPTER 3		52
INDUCTION MACHINE UNDER VARIOUS FAULTS.....		52
3.1	Introduction.....	52
3.2	Voltage Equations.....	52
3.3	Unbalances in Star-Connected Induction Machine.....	59
3.3.1	Supply Line “A” Open-Circuit Response	59
3.3.2	Stator Line to Line Fault.....	63
3.3.3	Stator Line “B” and “C” Shorted to Supply Line Voltage “C”	66
3.4	Delta Connected Stator	67
3.5	Unbalances in Delta-Connected Induction Machine	72
3.5.1	Supply Line “A” Open-Circuit Response	72
3.5.2	Stator Phase “A” Open-Circuit Response.....	74
3.5.3	Supply Line “B” Open and Stator Phase “A” Shorted	78
CHAPTER 4.....		81
A THREE-PHASE VOLTAGE SOURCE INVERTER WITH A FAULTED LEG.....		81
4.1	Introduction.....	81
4.2	System Model	81

4.3	Simulation Results	85
CHAPTER 5	93
PARAMETER DETERMINATION	93
5.1	Introduction.....	93
5.2	Experiments to Determine the Parameters.....	94
CHAPTER 6	104
THE INFLUENCE OF MAGNETIC SATURATION AND ARMATURE REACTION ON THE PERFORMANCE INTERIOR PERMANENT	104
MAGNET MACHINES	104
6.1	Introduction.....	104
6.2	Parameters Determination using Finite Element Method.....	105
6.3	Determination of Iron Loss Resistance.....	115
6.4	Influence of the Iron Loss and Parameter Variations on the Efficiency of IPMSM.....	117
CHAPTER 7	124
EFFICIENCY OPTIMIZATION OF THE INTERIOR PERMANENT MAGNET SYNCHRONOUS MACHINE.....	124
7.1	Introduction.....	124
7.2	Interior Permanent Magnet Synchronous Machine (IPMSM) Model including Iron Losses.....	125
7.3	Steady State Conditions	128
7.4	Power Losses of the IPMSM	129

7.5	Input-Output Feedback Linearization Control and Speed Controller Design	130
7.6	Input-Output Feedback Linearization Control and Torque Controller Design	137
7.7	Controller Structure	139
7.8	Simulation Results	142
CHAPTER 8		150
CONCLUSIONS		150
REFERENCES		152
APPENDIX A.....		161

LIST OF TABLES

	Page
Table 2. 1 Interior Permanent Magnet Synchronous Machine Parameters	28
Table 3. 1 Induction Machine Parameters	59
Table 4. 1 Induction Machine Parameters	86
Table 5. 1 Experimental measurements at no-load condition.....	99
Table 5. 2 Experimental measurements of the load test	103
Table A. 1: Nameplate data for the two horsepower buried magnet test machine.	162
Table A. 2: Stator Dimensions.....	164
Table A. 3: Damper Data.....	166
Table A. 4: Rotor Data.....	168
Table A. 5 Permanent Magnet Data.....	169

LIST OF FIGURES

	Page
Figure 1. 1 One pole cross section of a four pole, buried magnet, permanent magnet synchronous machine showing material boundaries.....	3
Figure 2. 1 Shows fault in (a) Delta-connected IPMSM (b) Star-connected IPMSM.....	27
Figure 2. 2 Shows Delta-connected Stator Interior Permanent Magnet Machine	28
Figure 2. 3 Shows the starting transient of a delta-connected IPMSM with normal three-phase supply, from top: phase 'a' current, phase 'b' current, phase 'c' current, rotor speed, torque, phase 'a' voltage.....	30
Figure 2. 4 Shows the steady state of a delta-connected IPMSM with normal three-phase supply, from top: phase 'a' current, phase 'b' current, phase 'c' current, rotor speed, torque, phase 'a' voltage.....	30
Figure 2. 5 Shows starting transient of a delta-connected IPMSM with PWM-VSI supply under Transient from top: phase 'a' current, phase 'b' current, phase 'c' current, rotor speed, torque, phase 'a' voltage.....	31
Figure 2. 6 Shows steady state of a delta-connected IPMSM with PWM-VSI supply, from top: phase 'a' current, phase 'b' current, phase 'c' current, rotor speed, torque, phase 'a' voltage.....	31
Figure 2. 7 Shows delta-connected IPMSM with a supply line open feeded with a normal three-phase supply, from top: phase 'a' current, phase 'b' current, phase 'c' current, rotor speed, torque, phase 'a' voltage.....	33

Figure 2. 8 Shows delta-connected IPMSM with a supply line open with PWM-VSI supply, from top: phase ‘a’ current, phase ‘b’ current, phase ‘c’ current, rotor speed, torque, phase ‘a’ voltage. 33

Figure 2. 9 Experimental results of phase ‘a’ line open for delta connection. (1) Inverter line-line voltage @ $V_{dc} = 90V$, (2) $I_{as} = 7A$ before and after fault, (3) $I_{cs} = 7A$ before and after fault, (4) $I_{bs} = 7A$ before and 13A after fault. 34

Figure 2. 10 Shows Delta-connected IPMSM for stator phase open with Normal three-phase supply from top: phase ‘a’ current, phase ‘b’ current, phase ‘c’ current, rotor speed, torque, phase ‘a’ voltage. 38

Figure 2. 11 Shows Delta-connected IPMSM for stator phase open with PWM-VSI from top: phase ‘a’ current, phase ‘b’ current, phase ‘c’ current, rotor speed, torque, phase ‘a’ voltage. 38

Figure 2. 12 Experimental results of phase ‘a’ winding open for delta connection. (1) Inverter line-line voltage @ $V_{dc} = 90V$, (2) $I_{as} = 5A$ before and 0A after fault, (3) $I_{cs} = 5A$ before and 6.5A after fault, (4) $I_{bs} = 5A$ before and 13A after fault. 39

Figure 2. 13 Shows Delta-connected IPMSM for shorted stator phase with Normal three-phase supply from top: phase ‘a’ current, phase ‘b’ current, phase ‘c’ current, rotor speed, torque, phase ‘a’ voltage. 39

Figure 2. 14 Shows Delta-connected IPMSM for shorted stator phase with PWM-VSI from top: phase ‘a’ current, phase ‘b’ current, phase ‘c’ current, rotor speed, torque, phase ‘a’ voltage. 40

Figure 2. 15 Shows Star-connected stator Interior Permanent Magnet Machine 41

Figure 2. 16 Shows starting transient of a star-connected IPMSM with normal three-phase supply, from top: phase ‘a’ current, phase ‘b’ current, phase ‘c’ current, rotor speed, torque.	41
Figure 2. 17 Shows steady state of a star-connected IPMSM with normal three-phase supply under Steady-state from top: phase ‘a’ current, phase ‘b’ current, phase ‘c’ current, rotor speed, torque.	42
Figure 2. 18 Shows starting transient of a star-connected IPMSM with PWM-VSI supply, from top: phase ‘a’ current, phase ‘b’ current, phase ‘c’ current, rotor speed, torque.	42
Figure 2. 19 Shows steady state of a star-connected IPMSM with PWM-VSI supply, from top: phase ‘a’ current, phase ‘b’ current, phase ‘c’ current, rotor speed, torque, phase ‘a’ voltage, line voltage.....	43
Figure 2. 20 Shows star-connected IPMSM for supply line open with normal three-phase supply from top: phase ‘a’ current, phase ‘b’ current, phase ‘c’ current, rotor speed, torque.	46
Figure 2. 21 Shows star-connected IPMSM for supply line open with PWM-VSI from top: phase ‘a’ current, phase ‘b’ current, phase ‘c’ current, rotor speed, torque, phase ‘a’ voltage, line voltage.....	46
Figure 2. 22 Experimental results of three-leg IPM motor with phase ‘a’ open. (1) Inverter line-line voltage @ $V_{dc} = 250V$, (2) $I_{as} = 3A$ before and $5A$ after fault, (3) $I_{ca} = 3A$ before and $0A$ after fault, (4) $I_{bc} = 3A$ before and $5A$ after fault.	47

Figure 2. 23 Shows star-connected IPMSM for line-line fault with normal three-phase supply from top: phase ‘a’ current, phase ‘b’ current, phase ‘c’ current, rotor speed, torque, phase ‘a’ voltage, line voltage.	49
Figure 2. 24 Shows star-connected IPMSM for line-line fault with PWM-VSI from top: phase ‘a’ current, phase ‘b’ current, phase ‘c’ current, rotor speed, torque, phase ‘a’ voltage, line voltage.	49
Figure 2. 25 Shows star-connected IPMSM for shorted stator phase with normal three-phase supply from top: phase ‘a’ current, phase ‘b’ current, phase ‘c’ current, rotor speed, torque, phase ‘a’ voltage, line voltage.	51
Figure 2. 26 Shows Star-connected IPMSM for shorted stator phase with PWM-VSI from top: phase ‘a’ current, phase ‘b’ current, phase ‘c’ current, rotor speed, torque, phase ‘a’ voltage, line voltage.....	51
Figure 3.1 Shows starting transient of a star connected Induction machine with 220V(rms) three-phase supply with load from top: phase currents ‘a’, ‘b’, ‘c’, mechanical speed, torque, phase voltage.	57
Figure 3.2 Shows the steady state characteristics of a star connected Induction machine with 220V(rms) three-phase supply with load from top: phase currents ‘a’, ‘b’, ‘c’, mechanical speed, torque, phase voltage.	57
Figure 3.3 Shows a star-connected Induction machine with PWM-VSI supply with 280V V_{dc} with load from top: phase currents ‘a’, ‘b’, ‘c’, mechanical speed, torque, phase voltage.....	58

Figure 3.4 Shows the steady state characteristics of a star-connected Induction machine with PWM-VSI supply with 280V V_{dc} with load from top: phase currents ‘a’, ‘b’, ‘c’, mechanical speed, torque, phase voltage..... 58

Figure 3. 5 Shows star-connected stator Induction machine with supply line ‘a’ open. .. 60

Figure 3.6 Shows a star-connected Induction machine with supply line ‘a’ open-circuited with 220V(rms) three-phase supply with load, from top: phase currents ‘a’, ‘b’, ‘c’, mechanical speed, torque, phase voltage. 62

Figure 3.7 Shows a star-connected Induction machine with supply line ‘a’ open-circuited with PWM-VSI supply with load, from top: phase currents ‘a’, ‘b’, ‘c’, mechanical speed, torque, phase voltage. 62

Figure 3. 8 Shows star-connected stator Induction machine with 2 stator phases shorted. 63

Figure 3.9 Shows from top: Phase voltage Torque Speed Phase current without 64

Figure 3.10 Shows a star-connected Induction machine with 2 stators winding shorted with 220V(rms) three-phase supply with load, from top: phase currents ‘a’, ‘b’, ‘c’, mechanical speed, torque, phase voltage. 65

Figure 3. 11 Shows a star-connected Induction machine with 2 stators winding shorted with PWM-VSI supply with load, from top: phase currents ‘a’, ‘b’, ‘c’, mechanical speed, torque, phase voltage. 65

Figure 3. 12 Shows star-connected stator Induction machine with a phase open-circuited and 2 shorted stator phases. 68

Figure 3. 13 Shows a star-connected Induction machine with 2 stators winding shorted while a phase is open-circuited, with 220V(rms) three-phase supply with load, from top: phase currents ‘a’, ‘b’, ‘c’, mechanical speed, torque, phase voltage.	68
Figure 3. 14 Shows a star-connected Induction machine with 2 stators winding shorted while a phase is open-circuited, with PWM-VSI supply with load, from top: phase currents ‘a’, ‘b’, ‘c’, mechanical speed, torque, phase voltage.....	69
Figure 3. 15 Shows an Induction machine with delta-connected stator.	69
Figure 3. 16 Shows delta-connected Induction machine with 104V three-phase supply with load from top: phase currents ‘a’, ‘b’, ‘c’, mechanical speed, torque, phase voltage.....	70
Figure 3. 17 Shows the steady state characteristics of an Induction machine with 104V three-phase supply with load from top: phase currents ‘a’, ‘b’, ‘c’, mechanical speed, torque, phase voltage.	70
Figure 3. 18 Shows Induction machine with PWM-VSI supply with 208V V_{dc} with load from top: phase currents ‘a’, ‘b’, ‘c’, mechanical speed, torque, phase voltage.....	71
Figure 3. 19 Shows the steady state characteristics of an Induction machine with PWM-VSI supply with 208V V_{dc} with load from top: phase currents ‘a’, ‘b’, ‘c’, mechanical speed, torque, phase voltage.	71
Figure 3. 20 Shows a delta-connected Induction machine with supply line ‘a’ open-circuited.....	72

Figure 3.21 Shows a delta-connected Induction machine with supply line ‘a’ open-circuited with 104V three-phase supply with load, from top: phase currents ‘a’, ‘b’, ‘c’, mechanical speed, torque, phase voltage..... 75

Figure 3. 22 Shows a delta-connected Induction machine with supply line ‘a’ open-circuited with PWM-VSI supply with load, from top: phase currents ‘a’, ‘b’, ‘c’, mechanical speed, torque, phase voltage. 75

Figure 3. 23 Shows a delta-connected Induction machine with phase ‘a’ open-circuited. 77

Figure 3.24 Shows a delta-connected Induction machine with phase ‘a’ open-circuited with 104V three-phase supply with load applied, from top: phase currents ‘a’, ‘b’, ‘c’, mechanical speed, torque, phase voltage..... 77

Figure 3.25 Shows a delta-connected Induction machine with phase ‘a’ open-circuited with PWM-VSI supply with load applied, from top: phase currents ‘a’, ‘b’, ‘c’, mechanical speed, torque, phase voltage. 78

Figure 3. 26 Shows a delta-connected Induction machine with phase ‘a’ short-circuited. 79

Figure 3. 27 Shows a delta-connected Induction machine with phase ‘a’ short-circuited with 104Vthree-phase supply with load applied, from top: phase currents ‘a’, ‘b’, ‘c’, mechanical speed, torque, phase voltage..... 80

Figure 3. 28 Shows a delta-connected Induction machine with phase ‘a’ short-circuited with PWM-VSI supply with load applied, from top: phase currents ‘a’, ‘b’, ‘c’, mechanical speed, torque, phase voltage. 80

Figure 4. 1 Conventional PWM-VSI inverter system.....	82
Figure 4. 2 PWM-VSI topology with a split DC capacitor replacing the faulted phase of the PWM-VSI inverter system.....	82
Figure 4. 3 Shows free acceleration characteristic of the Induction Machine (a) top: Speed, bottom: Torque (b) Stator phase Voltages from top: a,b,c (c) Steady state Stator current (d) Transient response of the stator current (e) Modulating signal top: M_b , bottom: M_c (f) Top: upper capacitor v_{a2} , middle: lower capacitor v_{a1} , bottom: difference of the two-capacitor $v_{a2}-v_{a1}$	87
Figure 4. 4 Shows Induction Machine with load 10N.m at steady state and remove afterwards (a) top: Speed, bottom: Torque (b) Stator phase Voltages from top: a,b,c (c) From Top: lower capacitor v_{a1} , upper capacitor v_{a2} , difference of the two-capacitor $v_{a2}-v_{a1}$, Modulating signal M_b , Modulating signal M_c (d) Steady state Stator current.....	88
Figure 4. 5 Shows free acceleration characteristic of the Induction Machine at 30Hz (a) top: Speed, bottom: Torque (b) Stator phase Voltages from top: a,b,c (c) From Top: lower capacitor v_{a1} , upper capacitor v_{a2} , difference of the two-capacitor $v_{a2}-v_{a1}$, Modulating signal M_b , Modulating signal M_c (d) Steady state Stator current.	89
Figure 4. 6 Shows free acceleration characteristic of the Induction Machine at 5Hz (a) top: Speed, bottom: Torque (b) Stator phase Voltages from top: a,b,c (c) From Top: lower capacitor v_{a1} , upper capacitor v_{a2} , difference of the two-capacitor $v_{a2}-v_{a1}$, Modulating signal M_b , Modulating signal M_c (d) Steady state Stator current.	90

Figure 4. 7 Shows free acceleration characteristic of the Induction Machine at 70Hz (a) top: Speed, bottom: Torque (b) Stator phase Voltages from top: a,b,c (c) From Top: lower capacitor v_{a1} , upper capacitor v_{a2} , difference of the two-capacitor $v_{a2}-v_{a1}$, Modulating signal M_b , Modulating signal M_c (d) Steady state Stator current.	91
Figure 4. 8 Shows the transient and steady state response of the Induction Machine at 60Hz (a) top: phase “a” current; phase “b” current; phase “c” current; Speed w_{rm} ; Torque, T_e (b) From Top: lower capacitor v_{a1} , upper capacitor v_{a2} , difference of the two-capacitor $v_{a2}-v_{a1}$, Modulating signal M_b , Modulating signal M_c (c) Steady state Stator current.....	92
Figure 5. 1 Electric equivalent circuit model of an Interior Permanent Magnet Synchronous Motor (IPMSM) without iron-loss.....	95
Figure 5. 2 schematic diagram of dc test used to determine the stator resistance	96
Figure 5. 3 Measured line to neutral terminal generator voltage (rms) vs air gap voltage for no load condition for machine connected in high and low voltage stator connections	98
Figure 5. 4 Stator q and d axis inductances and magnet flux (a) L_{qs} , (b) L_{ds} , (c) λ_m	102
Figure 6. 1 Electric equivalent circuit model of an Interior Permanent Magnet Synchronous Motor (IPMSM) with core-loss included.....	106
Figure 6. 2 Experimental and Finite Element Analysis results for a 2hp IPM. (a) q-axis inductance, (b) d-axis inductance, (c) magnet flux linkage.....	110
Figure 6. 3 Shows the cross section of the four-pole 2hp interior permanent magnet motor.....	111

Figure 6. 4(a-c): flux path and air-gap flux density, (b) no-load current, (c) q-axis rated current, (d) d-axis rated current.	112
Figure 6. 5: (a) Torque vs. speed, (b) power factor vs. torque angle (c) Input line current vs. torque angle (d) efficiency vs. torque angle.....	113
Figure 6. 6: (a) Air gap power vs. torque angle (b) Induced winding voltage at no-load vs. electrical degree (c) Air gap flux density at no-load vs. electric degree (d) Induced coil voltage vs. electric degree.....	114
Figure 6. 7: (a) Iron loss against input voltage (b) Input power against input voltage..	116
Figure 6. 8: Performance curves of the IPM. (a) Total losses, (b) efficiency (c) core loss (d) q-d current for torque values of 4Nm, 5Nm, 6Nm, and 7Nm for 60 Hz supply frequency.....	122
Figure 6. 9: Measured performance curves of the IPM for supply frequency of 60 Hz. (a) No-load loss against input voltage, (b) efficiency against input current, (c) total loss against input current, (d) Input power against input current (e) input current against input voltage, (d) core losses against input current.	123
Figure 7.1: Electric equivalent circuit model of an Interior Permanent Magnet Synchronous Motor (IPMSM) with core-loss included.....	126
Figure 7. 2: Controller Structure for the IPM Motor Drive.....	140
Figure 7. 3: The structure of the Controllers.....	141
Figure 7. 4: Stator q and d axis inductances and magnet flux (a) L_q , (b) L_d , (c) λ_m	144

Figure 7. 5 Shows from top: (a) reference speed, and rotor speed, (b) γ^* , γ minimization constraint (c) electromagnetic torque, (d) total loss, (e) q-axis current, (f) d-axis current.....	145
Figure 7. 6 Shows from top: (a)reference speed, and rotor speed, (b) speed error (c) γ^* , γ minimization constraint (d) minimization error.....	145
Figure 7. 7 shows from top: (a) q-axis inductance, (b) d-axis inductance (c) magnet flux	146
Figure 7. 8 shows from top: (a)q-axis voltage, (b) d-axis voltage.....	146
Figure 7. 9 shows total loss minimization control using constant parameters from top: (a) reference speed, and rotor speed, (b) γ^* , γ minimization constraint (c) electromagnetic torque, (d) total loss, (e) q-axis current, (f) d-axis current	147
Figure 7. 10: Torque control and minimum total loss tracking of IPM motor drive, from top: (a) reference torque, and electromagnetic torque, (b) speed, (c) total loss, (d) q-axis current, (e) d-axis current	148
Figure 7. 11 shows from top: (a) reference torque, and electromagnetic torque, (b) torque error (c) γ^* , γ minimization constraint (d) minization error	148
Figure 7. 12 shows from top: (a) q-axis inductance, (b) d-axis inductance (c) magnet flux	149
Figure A. 1 One pole cross section of a four pole, buried magnet, permanent magnet synchronous machine showing material boundaries.....	163
Figure A. 2: Stator slot dimensions of the buried magnet test motor.	165
Figure A. 3: Rotor slot dimensions of the buried magnet test motor.....	167

Figure A. 4: Magnet duct dimensions of the buried magnet test motor. 169

Figure A. 5: Stator and rotor lamination steel BH curve 170

Figure A. 6: Solid rotor shaft BH curve (Stator_def) 170

CHAPTER 1

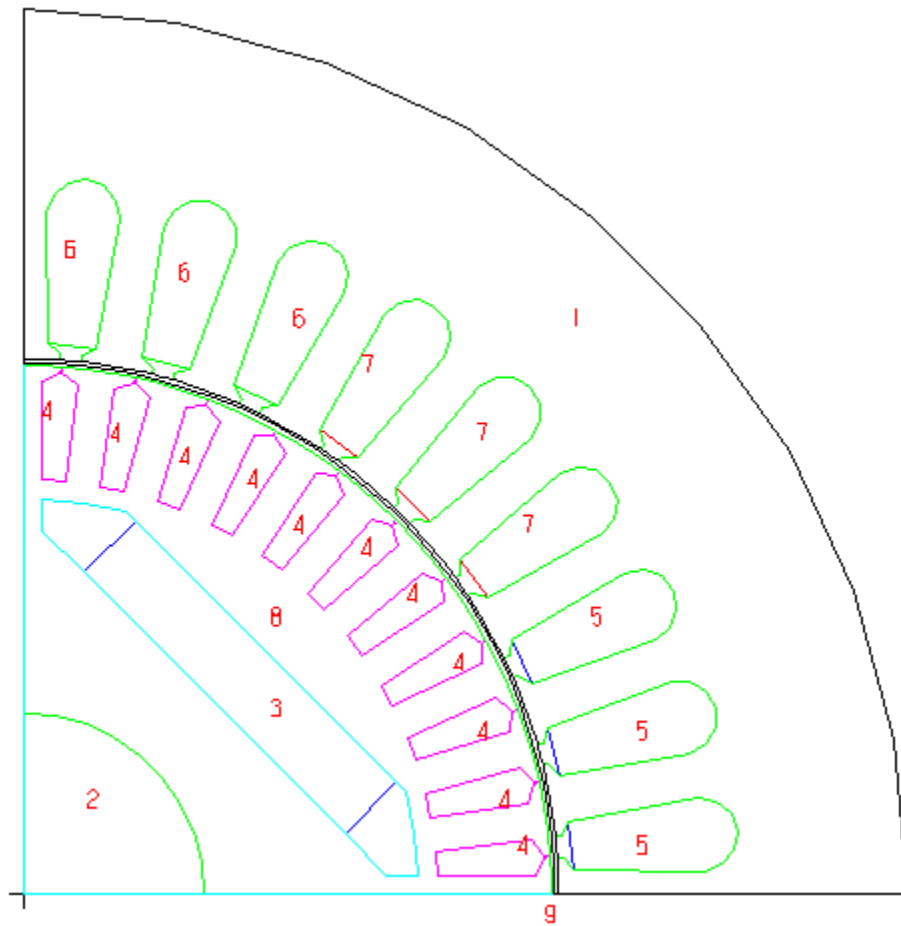
INTRODUCTION

1.1. Introduction

The availability of modern permanent magnet (PM) with considerable energy density led to the development of dc machines with PM field excitation in the 1950s. Introduction of PM to replace electromagnets, which have windings and require an external electric energy source, resulted in compact dc machines. The synchronous machine, with its conventional field excitation in the rotor, is replaced by the PM excitation; the slip rings and brush assembly are dispensed with. With the advent of switching power transistors and silicon-controlled-rectifier devices in the latter part of 1950s, the replacement of the mechanical commutator with an electronic commutator in the form of an inverter was achieved. These two developments contributed to the development of PM synchronous and brushless dc machines. The armature of the dc machine need not be on the rotor if the mechanical commutator is replaced by its electronic version. Therefore, the armature of the machine can be on the stator, enabling better cooling and allowing higher voltages to be achieved; significant clearance space is available for insulation in the stator. The excitation field that used to be on the stator is transferred to the rotor with PM poles. These machines are nothing but “an inside out dc machine” with the field and armature interchanged from the stator to rotor and rotor to stator, respectively [1].

A sample geometry of an interior permanent magnet (IPM) synchronous machine is shown in Figure 1.1. As the name implies, interior permanent magnet synchronous machine is a type of synchronous machine with interesting characteristics due to the presence of permanent magnets mounted inside the steel rotor core in either radial or circumferential orientations. Although this may at first be a relatively modest variation of the surface permanent magnet geometry, the process of covering each magnet with a steel pole piece in the IPM geometry produces several significant effects on the motor's operating characteristics. For example, burying the magnets inside the rotor provides the basis for a mechanically robust rotor construction capable of high speeds since the magnets are physically contained and protected.

This thesis contains the description of the Interior Permanent Magnet (IPM) synchronous machine; derivation of its dynamic models with and without iron losses; parameters determination; performance and influence of iron loss, armature reaction and magnetic flux saturation; analysis of the machine under fault situation; and torque and speed controller design.



Materials

1. Stator iron
2. Solid iron shaft
3. Permanent magnet
4. Rotor conductors
5. "A" phase conductors
6. "B" phase conductors
7. "-C" phase conductors
8. Rotor iron
9. Air gap

Figure 1. 1 One pole cross section of a four pole, buried magnet, permanent magnet synchronous machine showing material boundaries.

1.2. Literature Review

The basic IPM rotor configuration has been known for many years. The introduction of Alnico magnets nearly 65 years ago created a considerable interest in permanent magnet alternator development using interior permanent magnet motor geometries [2]. Soft iron pole shoes in these alternators provided a means of concentrating the flux of the thick Alnico magnets. Improvements in PM materials in following years turned attention to integral-horsepower applications for PM synchronous motors. A combination of an induction motor squirrel cage and the interior permanent magnet geometry provided possibilities for efficient steady-state operation as well as robust line starting. Work in this area accelerated during the past decade, following dramatic increase in the cost of energy.

The first commercially available rare earth permanent magnet was the samarium cobalt magnet which was introduced in 1970. This magnet have coercive forces three to five times that of Alnico magnet and, from a technical standpoint, are ideally suited for rotating electric machines; however, their cost was prohibitively high and is expected to remain so.

In order to understand the operating characteristics of an IPM synchronous motor drive, it is necessary first to appreciate the distinguishing electromagnetic properties of the interior PM motor itself. In particular, it is important to recognize that burying the magnets inside the rotor introduces saliency into the rotor magnetic circuit which is not present in other types of PM machines [2].

As reported in some literature cited in [2], the relative magnitudes of the d- and q-axis inductance values depend on the details of the rotor geometry. And also the torque production in the IPM motor is altered as a result of the rotor saliency, providing design flexibility which can be exercised to shape the motor output characteristics beneficially since the q-axis inductance of the IPM synchronous motor (L_q) typically exceeds the d-axis inductance (L_d), a feature which distinguishes the IPM motor from conventional wound-rotor salient-pole synchronous motors for which $L_d > L_q$ [3, 4].

A samarium-cobalt IPM machine is described in [5, 6]. In [6], the author points out that, due to the inverse saliency of the IPM machine, the output voltage tends to rise as the load is increased, and that this tendency could be exploited in the design of an IPM generator so that no external voltage regulation schemes are needed.

The neodymium-iron-boron (NdFeB) rare earth permanent magnet, introduced in 1983, has the same advantages over the ceramic and Alnico magnets as does the samarium cobalt magnets; but the production cost of the NdFeB rare earth permanent magnet was (and is) much lower. It was with the introduction of the NdFeB rare earth permanent magnet that a tremendous amount of new and renewed interest in PM machines have risen.

The numerical analysis of PM machines utilizing finite element techniques has been greatly aided by the astronomical increase in computer hardware and software capabilities. An optimal design technique for a PM machine, presented in [7], provides a technique to obtain a quick “first cut” determination of the overall dimensions of a PM machine which is to be used as a generator. The work in [8] explains a method by which

the computation of the magnetic field of permanent magnets in iron cores may be determined. In [9], a detailed finite element examination of interior and surface magnet machines is presented. With the advances in computational power (and the renewed interest in PM machines) there have been numerous recent programs created to analyze the PM machine in greater detail. The works in [3, 10-12] offer various ways in which to analyze and design PM machines.

Although considerable amount of literature exists about modeling of permanent magnet motors at steady state and transient conditions [2, 5, 13], the influence of losses has not yet been included in performance analysis of the machine [14]. Due to the rotor configuration of the permanent magnet motors which is schematically shown in Figure 1.1, a significant level of iron loss is present because of the high values of current that flow in the stator circuits even at no-load as the terminal voltage is increased or reduced from its open circuit value [15]. Several circumstances concur to produce this effect, which can be viewed as a result of the combined action of the magnet excitation with the complicated rotor magnetic structure. The flux redistribution that occurs due to saturation of the leakage flux paths produces the distortion of the air gap flux, and time harmonics appear that induce additional losses [16]. Unlike conventional synchronous machines where the iron loss is essentially connected to the terminal voltage, the usual no-load test with fixed excitation and variable terminal voltage does not allow separation of the core loss since a significant component of such loss is due to the current [4].

The changing d-axis inductance and inclusion of constant core loss resistance in the model of the PM synchronous machines was set forth in [4-6, 15, 17-21], while

methods for determining changing axis inductances and demonstrating their impact on the torque capability of the machine were reported in [5, 6].

The torque production of the inverter is affected by either a fault on the interior permanent magnet machine or the inverter feeding it impresses unbalanced voltage sets. The first step in designing the re-configurable inverter control scheme is the determination of the models of the converters and machines under anticipated fault conditions. Past work on analyses of inverter fed wye-connected interior permanent magnet motors and surface permanent magnet (brushless) motors with such faults as an open phase have been reported in [22-26]. The simulation and analysis of utility fed synchronous machines with field and damper windings based on q-d-o models have also been earlier reported in [27-28]. Model of the IPM in the stationary reference frame is developed since the stationary reference frame is the best reference frame to study imbalances and faults on electric machines[29]. Similar work on fault analysis on either the machine or the inverter system have also been reported in [30-33], whereby one of the inverter phase legs broken/damaged was replaced with a split DC capacitor bank in order to avoid the loss of functionality of the drive and increasing its reliability [34].

The operating efficiency depends on the control strategies and losses can be minimized by the optimal control strategy [35-36]. So far, the $I_d = 0$ control method, in which the armature current vector is in phase with the back-EMF due to permanent magnets and d-axis component of armature current I_d does not exist, is applied in general in order to avoid irreversible demagnetization of permanent magnets. The recent development of the permanent magnets, however, has brought materials with high

coercivity and high residual magnetism. Therefore, several control methods have been proposed to improve the performance of the PM motor drives [2, 37-41]. In such control methods, the d-axis component of armature current is actively controlled according to the operating speed and load conditions.

Nevertheless, the PM synchronous machines are strongly nonlinear systems. Salient-pole motors, in particular, present an additional complexity. Specifically, their torque can be decomposed into two components. The first component is the so-called reluctance torque, which is due to the saliency effect in the machine and is expressed as a nonlinear product of the d- and q- components of the currents. The second component, referred to as the hybrid torque, is produced through the interaction between the stator rotating magnetic field and the rotor magnets. It represents the largest component of the two and is a linear function of the current I_q .

The progress accomplished recently in the area of nonlinear control [42] and microprocessor technology [43, 44] has allowed the implementation of sophisticated control schemes; and performing nonlinear control laws to sinusoidal synchronous motors [46-48] and to various other types of electrical motors [49, 50-52], in order to improve their dynamic performances. These control strategies are either based on a direct scheme, in which the park transformation or feedback linearization techniques are used in order to linearize directly the voltage-torque relationship [45, 48] (or voltage-speed or voltage-position in the case of speed or position control, respectively), or on an indirect and more classical current-control scheme, in which the appropriate current repartition is imposed in stator phases by the use of internal current loops [2, 52-54].

In order to simplify the control strategy of the machine, however, most of the direct and indirect scheme algorithms take only the hybrid part of the torque into account, even for salient-pole motors [45, 54]. The direct component of the stator current I_d is then forced to zero, which consequently orientates the stator magnetic field perpendicularly to the rotor field. Thus, the reluctance torque is canceled. As a result, the maximum torque obtainable for a given current is not maximized, and the copper losses are not minimized and, thus, nor is the power consumption of the motor.

The motor losses consist of mechanical loss, copper loss and iron loss. The mechanical loss is speed dependent and not controllable. The controllable losses are copper loss and iron loss. The copper loss can be minimized by the maximum torque-per-amp control, in which the armature current vector is controlled in order to produce the maximum torque per armature current ampere [2]. The iron loss can be reduced by flux-weakening control [38-41], in which the d-axis current is controlled in order to reduce the air gap flux by the demagnetizing effects due to the d-axis armature reaction, because the iron loss is roughly proportional to flux density squared.

On the other hand, some control strategies allowing I_d to have nonzero values are proposed in the literature [2, 52]. They are all indirect current-control schemes and, as such, present several drawbacks. First, they assume a high-performance internal current loop, since it is always difficult to impose arbitrary currents in inductive stator windings [53]. Second, the design of the internal current loop is based on the assumption of a time-scale separation between the mechanical and electrical time constants. For PM ac motors,

the mechanical and electrical time constants can be of the same order of magnitude, and the assumption of time-scale separation may, therefore, not be satisfied.

Another drawback of this type of scheme is that torque regulation is achieved through an open-loop feedforward torque controller, which converts the desired torque into the required stator phase currents. Aside from the robustness issues that feedforward controllers raise, the choice of the phase currents references is not an easy task, since there is an infinite number of candidates for a given desired torque.

In [2], the saliency effect is used, and the current references which insure a maximum torque/ampere are found graphically. This lookup table approach has to be reapplied, however, for every different motor. In [52], an internal current loop scheme is used for torque tracking. The motor used is a hybrid step motor, and the general model in which the inductance and back EMF functions are nonsinusoidal is considered. Exact feedback linearization is used to design the internal current controller, while feedforward compensation is used to decouple the electrical and mechanical subsystems. The arbitrariness in choosing the current references is formally expressed in terms of a free function, which can be selected in such a way as to minimize the power loss in the motor. The resulting scheme is interesting in terms of its generality. It is, however, computationally complex. The computation of the current references is performed in a feedforward manner and may involve time derivatives of the input torque command. This may be circumvented by augmenting the order of the controller.

Most vector controlled ac drives have been performed under the assumption that there is no iron loss in motors. As the employment of vector controlled ac motors,

especially induction motor, permanent magnet synchronous motor (PMSM), synchronous reluctance motor has become standard in industrial drives, the improvement of ac motor drives has been important issue. For this reason, several attempts have been made to consider the iron loss in vector controlled ac motor drives. Influences of the iron loss on the synchronous reluctance motors has experimentally been investigated [55] and various strategies which compensate the influence of the iron loss have been proposed in [56-60]. Influences of the iron loss on the flux linkage deviation, its orientation error, and torque deviation of a vector controlled induction motor have analytically been investigated [61] and various compensation strategies have been investigated in [62-64]. Although a number of work dealing with vector controlled ac motor drive taking the iron loss into account have been published, only a few paid attention to PMSM drives [17, 65]. In [17], the optimal control method of armature current vector, according to the operating speed and the load conditions, is proposed in order to minimize the controllable losses. The reluctance torque and d-axis armature reaction are utilized to minimize the losses in the control algorithm. This work is similar to the same idea presented in [63]. Maximum torque per ampere method has been introduced to enhance torque production and reduce input current assuming constant machine parameters [40, 33, 66]. A recent effort seeks to improve the efficiency of the machine by including the effects of changing q and d axis inductances which are measured on line [67, 68]. With a static mapping of the q and d-axis currents to the electromagnetic torque and using the classical IPM torque control scheme in [33], it is shown that including saturation dependence of the axis inductances, higher torque and higher efficiency result if the maximum torque per ampere trajectory of

the machine is implemented. On-line computation of the parameters has also been part of the work discuss in another type of permanent magnet synchronous machine [69] where the d-axis inductance is a function of the d-axis current.

1.3. Research Motivation

The PM synchronous motor offers several advantages for applications which require high acceleration and a good torque quality (i.e., no ripples), namely a high torque-to-inertia ratio and an excellent power factor close to unity, since the copper losses are essentially located only in the stator. In the applications of continuous long time operation such as electric vehicles and compressor drives, the efficiency is one of the most important performances. Therefore, the PM motor is suitable for such applications.

Literature survey yields some important information of this machine:

(a) Various efforts have been made to establish proper dynamic model and accurately analyze the performance of the interior permanent magnet synchronous motor in the past years but the influence of armature reaction, magnetic saturation and iron loss, has not yet been included in performance analysis of the machine. The impact of changing axis inductance on torque capability of the machine was reported in [5,6], the analysis has been done without iron loss resistance. Hence, a model whose equations consider the general case which includes the influence of armature reaction, magnetic saturation and iron loss was developed for the analysis of the performance of the interior permanent magnet synchronous machine. The determination of the parameters of the machine are

therefore necessary. Thus, the parameters (namely the mutual inductances in the d and q axes and the flux linkage created by the magnet) must be function of the operating conditions. Hence, finite element method and experimental measurement are used in determining these parameters and the validation of the two methods is done to compare their results.

(b) There have been work that has considered some analysis of some faults condition on IPM synchronous machine, there have been none that has considered faults on delta-connected stator machines. The analysis done on this topic has applied stationary reference frame of the model of the machines (IPM and induction machine) in the analysis of the machine in both star and delta connected stator winding. Instead of shutting down the system in the occurrence of a fault on one of the inverter legs, a modulation scheme of the PWM-VSI can be re-configure for the faulted/damaged inverter phase legs by replacing the phase with a split DC capacitor, this will improve the reliability of the whole system when a fault is sense.

(c) Most vector controlled ac drives have been performed under the assumption that there is no iron loss in motors. There have been work reported in on maximum torque per ampere method [40, 33, 66] to enhance torque production and reduce input current assuming constant machine parameters. A recent effort seeks to improve the efficiency of the machine by including the effects of changing q and d axis inductances which are measured on-line [67, 68] have been reported. With a static mapping of the q and d-axis currents to the electromagnetic torque and using the classical IPM torque control scheme in [33], it is shown that including saturation dependence of the axis inductances, higher

torque and higher efficiency result if the maximum torque per ampere trajectory of the machine is implemented. And with the advent of microprocessor technology and accomplishment in the area of nonlinear control law, the implementation of sophisticated control law has been made possible. Hence, it is necessary to combine the influence of parameters variation; iron loss and nonlinear control law to achieve the objective of optimal control of the machine, which gives minimum loss, and the ability to control the machine the speed (or torque) of the machine.

The motivation for this work was inspired from the above discussion. The objectives are to obtain proper understanding of the response and performance of electrical machines in the situation of fault; and their operating characteristics due to the geometric structure will be well laid out in determining their performance. With the use of PWM converter and digital signal processor (DSP), the proposed research will strive towards promoting effective and flexible control of the IPM synchronous machine in industrial applications.

1.4. Scope of Work

The research is carried out using a two horsepower IPM machine and the implementation of the total loss minimization control scheme is being implemented using an Analog DSP (ADMC 401).

Chapter 2 of this thesis discusses the fault tolerant of an interior permanent magnet synchronous motor with the stator winding in star and delta connection. Since the

torque production of the inverter is affected by either a fault on the interior permanent magnet machine or the inverter impresses unbalanced voltage sets on the machine, the first step in designing the re-configurable inverter control scheme is the determination of the models of the converters and machines under anticipated fault conditions. Simulation and experimental results are presented for these different fault conditions.

Chapter 3 presents similar fault tolerant analysis of an induction motor under different faults conditions and; simulation results for star- and delta- connected stator winding induction type motor is also analyzed.

Chapter 4 presents the mathematical modeling of a VSI-PWM with four switches and two capacitors in the dc link. The system has been derived using the generalized modulation theory to generate three-phase balanced voltages when a fault is detected in any of the legs of the inverter.

Chapter 5 presents the determination of the parameters of the IPM using an electrical equivalent circuit model without the iron loss included [70]. The modeling of the IPM includes the effects caused by the changing saturation and armature reaction dependent axes inductances and magnet flux linkage. The experimental tests used a two horsepower operating in generator mode in this literature.

Chapter 6 investigates the combined influence of magnetic flux saturation and the stator current armature reaction on the steady-state torque capability and efficiency of an interior permanent magnet machine (IPM). These effects are reflected in the classical qd0 equivalent circuit model of the machine in the following fashion: The core loss is represented with a stator flux linkage dependent core loss resistance, the armature

reaction effect is accounted for by the changing magnet flux linkage and magnetic saturation effect is reflected in the changing d and q-axis inductances of the machine. The steady-state modeling and analysis of the machine, the nature of the variations of the machine parameters and how they influence the machine torque and efficiency are clearly laid out and eventually confirmed by simulation and experimental results. Finite element analysis results for an experimental 2 hp(horsepower) IPM are also presented to further validate the conclusions drawn from calculation and experimental results.

The final chapter of this thesis is based on a nonlinear controller based on a direct scheme which directly controls the rotor speed (or torque). The nonlinear controller achieves both objectives used in [2] and [52], namely, torque regulation and minimization of power losses without recurring to an internal current loop nor to any feedforward compensation. It is also applied to rotor speed control with total loss minimization implemented during operation of the IPM. In both of these cases, the electrical model of the PM synchronous motor account for the iron losses and copper losses as in [17]. The control scheme is based on an input-output linearization method where the inputs are the stator voltages which is similar to [71]. By defining an output linked to the total loss (iron loss and copper loss) which when forced to zero, leads to maximum machine efficiency of better improvement compare to when only the copper loss is minimized. Simulation and experimental results are used to compare the results of the two schemes, minimization of total loss and minimization of copper loss also referred to as torque-per-ampere operation. To test some of the control strategies outline in Chapter 7, an

experimental system was developed. This system is based on an Analog (ADMC401) DSP and custom built power electronic hardware using IGBT's.

CHAPTER 2

INTERIOR PERMANENT MAGNET MACHINE UNDER VARIOUS FAULTS

2.1. Introduction

An interior permanent magnet synchronous machine (IPMSM) with damper winding is analyzed in this chapter under different fault conditions. Interior permanent magnet synchronous machines are attractive for a variety of applications because of their high power density, wide constant-power speed range, and excellent efficiency. However faults in either the machine or inverter create special challenges in any type of PM synchronous machine drive because of the presence of spinning rotor magnets that cannot be turned off at will. It is very important to understand the IPM drive's fault response in order to prevent fault-induced damage to either the machine, the inverter, or to the connected load.

This chapter investigates six important fault classes in all for an IPM machine in which the stator winding are either connected in star or delta form. These types of fault can be caused by mechanical failure of a machine terminal connector, an internal winding rupture, electrical failure of one of the three-phase supply line or by an electrical failure in one of the inverter phase legs.

The concepts of a fault tolerant machine is that it will continue to operate in a satisfactory manner after sustaining a fault. The term "satisfactorily" implies a minimum level of performance once faulted. The degree of fault that must be sustainable should be

related to the probability of its occurrence. For most safety critical applications it is accepted that the drive must be capable of rated output after the occurrence of any one fault.

The principal electromagnetic faults which may occur within the machine are:

- (1) Winding open-circuit;
- (2) Winding short-circuit (phase/phase);
- (3) Winding short circuit at terminals.

Within the power converter the faults under consideration are as follows:

- (1) Power device open-circuit;
- (2) Power device short circuit;
- (3) DC link capacitor failure.

Analytical techniques appropriate for the IPM machine fault conditions are presented in the next sections, followed by simulations of all the fault conditions (within the IPM machine for either star or delta connected stator winding) and some experimental verification test results.

2.2. Derivation of Machine Equations

These analyses are effectively carried out when the dq voltage equations are represented in stationary reference frame [29].

The qd model equations of the normal IPM machine in the rotor reference frame are given as [74]

$$V_{qs}^e = r_s I_{qs}^e + p\lambda_{qs}^e + \omega_r \lambda_{ds}^e \quad (2.1)$$

$$V_{ds}^e = r_s I_{ds}^e + p\lambda_{ds}^e - \omega_r \lambda_{qs}^e \quad (2.2)$$

$$V_{os}^e = r_s I_{os}^e + p\lambda_{os}^e \quad (2.3)$$

$$V_{qr}^e = r_r I_{qr}^e + p\lambda_{qr}^e \quad (2.4)$$

$$V_{dr}^e = r_r I_{dr}^e + p\lambda_{dr}^e \quad (2.5)$$

$$V_{or}^e = r_r I_{or}^e + p\lambda_{or}^e \quad (2.6)$$

where the angular rotor speed is ω_r , phase stator and referred rotor resistances are r_s and r_r , respectively, the stator and rotor qd flux linkages are λ_{qdos} and λ_{qdor} , respectively, the currents in the stator and rotor circuits are I_{qdos} and I_{qdor} , respectively, the input voltages to the stator and rotor windings are V_{qdos} and V_{qdor} , respectively, and the magnet flux is λ_m .

Using inter-reference frame transformation [75]

$$f_{qdos}^y = {}^x K^y f_{qdos}^x \quad (2.7)$$

where ${}^x K^y = \begin{bmatrix} \cos(\theta_y - \theta_x) & -\sin(\theta_y - \theta_x) & 0 \\ \sin(\theta_y - \theta_x) & \cos(\theta_y - \theta_x) & 0 \\ 0 & 0 & 1 \end{bmatrix}$ and the reference frame angles of y and

x reference frames are, respectively, given as θ_y and θ_x .

Variables f_q^x , f_d^x , and f_o^x can be mapped into f_q^y , f_d^y , and f_o^y , and vice-versa. Hence, the model equations expressed in rotor reference frame as given in Equations (2.1–2.6) can be transformed to stationary reference frame equations. Generally, transforming from rotor reference frame to stationary reference frame gives

$$\begin{aligned}
f^s_q &= f^e_q \cos(\theta_r) + f^e_d \sin(\theta_r) \\
f^s_d &= -f^e_q \sin(\theta_r) + f^e_d \cos(\theta_r) \\
f^s_o &= f^e_o .
\end{aligned} \tag{2.8}$$

Similarly, transforming from stationary reference frame to rotor reference frame gives

$$\begin{aligned}
f^e_q &= f^s_q \cos(\theta_r) - f^s_d \sin(\theta_r) \\
f^e_d &= f^s_q \sin(\theta_r) + f^s_d \cos(\theta_r) \\
f^e_o &= f^s_o .
\end{aligned} \tag{2.9}$$

where θ_r is reference angle in the rotor reference frame. In both transformation given in (2.8) and (2.9), the zero variables remain the same.

In rotor reference frame, the flux linkages can be expressed as

$$\lambda^e_{qs} = L_{qs} I^e_{qs} + L_{mq} I^e_{qr} \tag{2.10a}$$

$$\lambda^e_{qr} = L_{qr} I^e_{qr} + L_{mq} I^e_{qs} \Rightarrow I^e_{qr} = \lambda^e_{qr} / L_{qr} - (L_{mq} / L_{qr}) I^e_{qs} . \tag{2.10b}$$

Substitute (2.10b) in (2.10a) gives

$$\lambda^e_{qs} = L_{qq} I^e_{qs} + L_{mq} / L_{qr} \lambda^e_{qr} \tag{2.10c}$$

where

$$L_{qq} = L_{qs} - L^2_{mq} / L_{qr}$$

$$\lambda^e_{ds} = L_{ds} I^e_{ds} + L_{md} I^e_{dr} + \lambda_m \tag{2.11a}$$

$$\lambda^e_{dr} = L_{dr} I^e_{dr} + L_{md} I^e_{ds} + \lambda_m \Rightarrow I^e_{dr} = \lambda^e_{dr} / L_{dr} - (L_{md} / L_{dr}) I^e_{ds} - \lambda_m / L_{dr} . \tag{2.11b}$$

Substitute (2.11b) in (2.11a) gives

$$\lambda^e_{ds} = L_{dd} I^e_{ds} + (L_{md} / L_{dr}) \lambda^e_{dr} + \lambda_{mm} \tag{2.11c}$$

where

$$L_{dd} = L_{ds} - L^2_{md} / L_{dr} , \lambda_{mm} = \lambda_m [1 - L_{md} / L_{dr}] .$$

Transforming the stator flux linkages and the rotor currents from rotor reference frame to stationary reference frame as defined in Equation (2.8) gives

$$\lambda_{qs}^s = \lambda_{qs}^e \cos(\theta_r) + \lambda_{ds}^e \sin(\theta_r) \quad (2.12)$$

$$\lambda_{ds}^s = -\lambda_{qs}^e \sin(\theta_r) + \lambda_{ds}^e \cos(\theta_r) \quad (2.13)$$

$$I_{qr}^s = I_{qr}^e \cos(\theta_r) + I_{dr}^e \sin(\theta_r) \quad (2.14)$$

$$I_{dr}^s = -I_{qr}^e \sin(\theta_r) + I_{dr}^e \cos(\theta_r) . \quad (2.15)$$

The stator currents and rotor flux linkages are also transformed from the stationary reference frame to rotor reference frame by making use of Equation (2.9)

$$I_{qs}^e = I_{qs}^s \cos(\theta_r) - I_{ds}^s \sin(\theta_r) \quad (2.16)$$

$$I_{ds}^e = I_{qs}^s \sin(\theta_r) + I_{ds}^s \cos(\theta_r) \quad (2.17)$$

$$\lambda_{qr}^e = \lambda_{qr}^s \cos(\theta_r) - \lambda_{dr}^s \sin(\theta_r) \quad (2.18)$$

$$\lambda_{dr}^e = \lambda_{qr}^s \sin(\theta_r) + \lambda_{dr}^s \cos(\theta_r). \quad (2.19)$$

Substituting (2.10c), (2.11c), (2.16), (2.17), (2.18), and (2.19) into (2.12) and (2.13) gives

$$\begin{aligned} \lambda_{qs}^s = & I_{qs}^s [L_2 - L_1 \cos(2\theta_r)] + I_{ds}^s L_1 \sin(2\theta_r) + \lambda_{qr}^s [L_4 - L_3 \cos(2\theta_r)] \\ & + \lambda_{dr}^s L_3 \sin(2\theta_r) + \lambda_{mm} \sin(\theta_r) \end{aligned} \quad (2.20)$$

$$\begin{aligned} \lambda_{ds}^s = & I_{qs}^s L_1 \sin(2\theta_r) + I_{ds}^s [L_2 + L_1 \cos(2\theta_r)] + \lambda_{qr}^s L_3 \sin(2\theta_r) \\ & + \lambda_{dr}^s [L_4 + L_3 \cos(2\theta_r)] + \lambda_{mm} \cos(\theta_r). \end{aligned} \quad (2.21)$$

Differentiating Equations (2.20) and (2.21) with respect to time, t , whereby $d\theta_r/dt = \omega_r$ gives

$$\begin{aligned}
p\lambda_{qs}^s &= pI_{qs}^s [L_2 - L_1 \cos(2\theta_r)] + pI_{ds}^s L_1 \sin(2\theta_r) + p\lambda_{qr}^s [L_4 - L_3 \cos(2\theta_r)] \\
&+ p\lambda_{dr}^s L_3 \sin(2\theta_r) + \omega_r [I_{qs}^s 2L_1 \sin(2\theta_r) + I_{ds}^s 2L_1 \cos(2\theta_r) + \lambda_{qr}^s 2L_3 \sin(2\theta_r) \\
&+ \lambda_{dr}^s 2L_3 \cos(2\theta_r) + \lambda_{mm} \cos(\theta_r)] \quad (2.22)
\end{aligned}$$

$$\begin{aligned}
p\lambda_{ds}^s &= pI_{qs}^s L_1 \sin(2\theta_r) + pI_{ds}^s [L_2 + L_1 \cos(2\theta_r)] + p\lambda_{qr}^s L_3 \sin(2\theta_r) \\
&+ p\lambda_{dr}^s [L_4 + L_3 \cos(2\theta_r)] + \omega_r [I_{qs}^s 2L_1 \cos(2\theta_r) - I_{ds}^s 2L_1 \sin(2\theta_r) + \lambda_{qr}^s 2L_3 \cos(2\theta_r) \\
&- \lambda_{dr}^s 2L_3 \sin(2\theta_r) - \lambda_{mm} \sin(\theta_r)] . \quad (2.23)
\end{aligned}$$

Substituting Equations (2.10b), (2.11b), (2.16), (2.17), (2.18), and (2.19) in Equations (2.14) and (2.15), it can be shown that

$$\begin{aligned}
I_{qr}^s &= \lambda_{qr}^s [L_6 - L_5 \cos(2\theta_r)] + \lambda_{dr}^s L_5 \sin(2\theta_r) + I_{qs}^s [L_3 \cos(2\theta_r) - L_4] - I_{ds}^s L_3 \sin(2\theta_r) \\
&- (\lambda_m / L_{dr}) \sin(\theta_r) \quad (2.24)
\end{aligned}$$

$$\begin{aligned}
I_{dr}^s &= \lambda_{qr}^s L_5 \sin(2\theta_r) + \lambda_{dr}^s [L_6 + L_5 \cos(2\theta_r)] - I_{qs}^s L_3 \sin(2\theta_r) - I_{ds}^s [L_3 \cos(2\theta_r) + L_4] \\
&- (\lambda_m / L_{dr}) \cos(\theta_r) \quad (2.25)
\end{aligned}$$

where

$$L_1 = (L_{dd} - L_{qq})/2, L_2 = (L_{dd} + L_{qq})/2, L_3 = (L_{md}/L_{dr} - L_{mq}/L_{qr})/2,$$

$$L_4 = (L_{md}/L_{dr} + L_{mq}/L_{qr})/2, L_5 = (1/L_{dr} - 1/L_{qr})/2, L_6 = (1/L_{dr} + 1/L_{qr})/2.$$

The stationary reference frame stator voltage equations can be expressed as follows:

$$V_{qs}^s = r_s I_{qs}^s + p\lambda_{qs}^s \quad (2.26)$$

$$V_{ds}^s = r_s I_{ds}^s + p\lambda_{ds}^s . \quad (2.27)$$

Substitute $p\lambda_{qs}^s$ in Equation (2.22) in (2.26) and $p\lambda_{ds}^s$ in Equation (2.23) in (2.27), these give the qd voltage equations of the stator in stationary reference frame as a function of the stator currents, magnet flux, and rotor fluxes as expressed below.

$$\begin{aligned}
V_{qs}^s &= r_s I_{qs}^s + p I_{qs}^s [L_2 - L_1 \cos(2\theta_r)] + p I_{ds}^s L_1 \sin(2\theta_r) + p \lambda_{qr}^s [L_4 - L_3 \cos(2\theta_r)] \\
&+ p \lambda_{dr}^s L_3 \sin(2\theta_r) + \omega_r [I_{qs}^s 2L_1 \sin(2\theta_r) + I_{ds}^s 2L_1 \cos(2\theta_r) + \lambda_{qr}^s 2L_3 \sin(2\theta_r) \\
&+ \lambda_{dr}^s 2L_3 \cos(2\theta_r) + \lambda_{mm} \cos(\theta_r)] \\
&= p I_{qs}^s [L_2 - L_1 \cos(2\theta_r)] + p I_{ds}^s L_1 \sin(2\theta_r) + V_y^s
\end{aligned} \tag{2.28}$$

$$\begin{aligned}
V_{ds}^s &= r_s I_{ds}^s + p I_{qs}^s L_1 \sin(2\theta_r) + p I_{ds}^s [L_2 + L_1 \cos(2\theta_r)] + p \lambda_{qr}^s L_3 \sin(2\theta_r) \\
&+ p \lambda_{dr}^s [L_4 + L_3 \cos(2\theta_r)] + \omega_r [I_{qs}^s 2L_1 \cos(2\theta_r) - I_{ds}^s 2L_1 \sin(2\theta_r) + \lambda_{qr}^s 2L_3 \cos(2\theta_r) \\
&- \lambda_{dr}^s 2L_3 \sin(2\theta_r) - \lambda_{mm} \sin(\theta_r)] \\
&= p I_{qs}^s L_1 \sin(2\theta_r) + p I_{ds}^s [L_2 + L_1 \cos(2\theta_r)] + V_x^s
\end{aligned} \tag{2.29}$$

where V_y^s and V_x^s are variables which depends on the state variables $p I_{qs}^s$ and $p I_{ds}^s$.

$$\begin{aligned}
V_y^s &= r_s I_{qs}^s + p \lambda_{qr}^s [L_4 - L_3 \cos(2\theta_r)] + p \lambda_{dr}^s L_3 \sin(2\theta_r) \\
&+ \omega_r [I_{qs}^s 2L_1 \sin(2\theta_r) + I_{ds}^s 2L_1 \cos(2\theta_r) + \lambda_{qr}^s 2L_3 \sin(2\theta_r) + \lambda_{dr}^s 2L_3 \cos(2\theta_r) + \lambda_{mm} \cos(\theta_r)] \\
V_x^s &= r_s I_{ds}^s + p \lambda_{qr}^s L_3 \sin(2\theta_r) + p \lambda_{dr}^s [L_4 + L_3 \cos(2\theta_r)] + \omega_r [I_{qs}^s 2L_1 \cos(2\theta_r) \\
&- I_{ds}^s 2L_1 \sin(2\theta_r) + \lambda_{qr}^s 2L_3 \cos(2\theta_r) - \lambda_{dr}^s 2L_3 \sin(2\theta_r) - \lambda_{mm} \sin(\theta_r)]
\end{aligned}$$

The stationary reference frame rotor voltage equations can be expressed as follows:

$$V_{qr}^s = r_r I_{qr}^s + p \lambda_{qr}^s - \omega_r \lambda_{dr}^s \tag{2.30}$$

$$V_{dr}^s = r_r I_{dr}^s + p \lambda_{dr}^s + \omega_r \lambda_{qr}^s. \tag{2.31}$$

Solving Equations (2.28) and (2.29) for $p I_{qs}^s$ and $p I_{ds}^s$ while Equations (2.30) and (2.31) are solved for $p \lambda_{qr}^s$ and $p \lambda_{dr}^s$ gives the following results.

$$\begin{aligned}
L_{dd} L_{qq} p I_{qs}^s &= [(-L_2 L_4 + L_2 L_3 \cos(2\theta_r) - L_1 L_4 \cos(2\theta_r) + L_3 L_1) p \lambda_{qr}^s \\
&+ (L_4 L_1 - L_2 L_3) \sin(2\theta_r) p \lambda_{dr}^s - I_{qs}^s [r_s (L_1 \cos(2\theta_r) + L_2) + 2L_1 L_2 \omega_r \sin(2\theta_r)] + I_{ds}^s [r_s L_1 \sin(2\theta_r) \\
&- 2\omega_r L_1 (L_2 \cos(2\theta_r) + L_1)] - \lambda_{qr}^s \omega_r 2L_2 L_3 \sin(2\theta_r) - \lambda_{dr}^s 2\omega_r L_3 (L_2 \cos(2\theta_r) + L_1)
\end{aligned}$$

$$- \lambda_{mm}\omega_r \cos(\theta_r)L_{dd} + (L_1 \cos(2\theta_r) + L_2)V_{qs}^s - L_1 \sin(2\theta_r)V_{ds}^s] \quad (2.32a)$$

or,

$$L_{dd}L_{qq}pI_{qs}^s = [V_{qs}^s - V_y^s] [L_2 + L_1 \cos(2\theta_r)] - [V_{ds}^s - V_x^s]L_1 \sin(2\theta_r) \quad (2.32b)$$

$$\begin{aligned} L_{dd}L_{qq}pI_{ds}^s = & [(-L_2L_4 - L_2L_3 \cos(2\theta_r) + L_1L_4 \cos(2\theta_r) + L_3L_1)p\lambda_{dr}^s + (L_4L_1 - L_2L_3)\sin(2\theta_r)p\lambda_{qr}^s \\ & + I_{qs}^s (r_s L_1 \sin(2\theta_r) + 2\omega_r L_1 [L_1 - L_2 \cos(2\theta_r)]) + I_{ds}^s [r_s (L_1 \cos(2\theta_r) - L_2) + 2L_1 L_2 \omega_r \sin(2\theta_r)] \\ & + \lambda_{qr}^s 2\omega_r L_3 [L_1 - L_2 \cos(2\theta_r)] + \lambda_{dr}^s \omega_r 2L_2 L_3 \sin(2\theta_r) + \lambda_{mm}\omega_r \sin(\theta_r)L_{dd} + [L_2 - L_1 \cos(2\theta_r)]V_{ds}^s \\ & - L_1 \sin(2\theta_r)V_{qs}^s] \end{aligned} \quad (2.33a)$$

or,

$$L_{dd}L_{qq}pI_{ds}^s = [V_{ds}^s - V_x^s] [L_2 - L_1 \cos(2\theta_r)] - [V_{qs}^s - V_y^s] L_1 \sin(2\theta_r) \quad (2.33b)$$

$$\begin{aligned} p\lambda_{qr}^s = & V_{qr}^s - r_r [\lambda_{qr}^s (L_6 - L_5 \cos(2\theta_r)) + \lambda_{dr}^s L_5 \sin(2\theta_r) + I_{qs}^s (L_3 \cos(2\theta_r) - L_4) \\ & - I_{ds}^s L_3 \sin(2\theta_r) - (\lambda_m/L_{dr}) \sin(\theta_r)] + \omega_r \lambda_{dr}^s \end{aligned} \quad (2.34)$$

$$\begin{aligned} p\lambda_{dr}^s = & V_{dr}^s - r_r [\lambda_{dr}^s (L_6 + L_5 \cos(2\theta_r)) + \lambda_{qr}^s L_5 \sin(2\theta_r) - I_{ds}^s (L_3 \cos(2\theta_r) + L_4) \\ & - I_{qs}^s L_3 \sin(2\theta_r) - (\lambda_m/L_{dr}) \cos(\theta_r)] - \omega_r \lambda_{qr}^s \end{aligned} \quad (2.35)$$

The torque equation is expressed as

$$T_e = 3P(\lambda_{ds}^s I_{qs}^s - \lambda_{qs}^s I_{ds}^s)/4 \quad (2.36)$$

where P is the number of poles.

Substituting λ_{qs}^s and λ_{ds}^s in (2.36) gives the following expression for torque:

$$\begin{aligned} T_e = & 3P\{ [I_{qs}^s L_1 \sin(2\theta_r) + \lambda_{qr}^s L_3 \sin(2\theta_r) + \lambda_{dr}^s [L_4 + L_3 \cos(2\theta_r)] + \lambda_{mm} \cos(\theta_r)] I_{qs}^s \\ & - [I_{ds}^s L_1 \sin(2\theta_r) + \lambda_{qr}^s [L_4 - L_3 \cos(2\theta_r)] + \lambda_{dr}^s L_3 \sin(2\theta_r) + \lambda_{mm} \sin(\theta_r)] I_{ds}^s \\ & + 2I_{qs}^s I_{ds}^s L_1 \cos(2\theta_r)]/4 \end{aligned} \quad (2.37)$$

$$T_e = J(2/P)p\omega_r + T_L \quad . \quad (2.38)$$

The following sections investigate three important fault classes that can occur in an IPM synchronous machine for each different type of machine stator connection, star, and delta-connected stator as shown in Figure 2.1, some of which have been reported in earlier works [22-26]. The simulation and analysis of utility fed synchronous machines with field and damper windings based on q-d-o models have also been earlier reported in [27-28]. With the stator state variables in qd currents and the rotor state variables in qd flux linkages makes it possible and easier to simulate the different stator fault situations. Laboratory experiments were also carried out for some realistic/probable fault situations in IPMSM to confirm the computer simulation results. The IPMSM requires a high V_{dc} for starting to overcome the inertia of the magnet on the rotor, which can then be reduced when the machine has run up to speed. Table 2.1 shows the machine parameters of the 2-hp, 115/230 V, 60 Hz, 1800 rpm IPMSM used in the computer simulations.

2.3. Delta-Connected Stator

The delta-connected stator interior permanent magnet synchronous machine is shown in Figure 2.2 with the phase voltages expressed as follows:

$$V_{an} = V_{ab} = e_{ag} - e_{bg} \quad (2.39)$$

$$V_{bn} = V_{bc} = e_{bg} - e_{cg} \quad (2.40)$$

$$V_{cn} = V_{ca} = e_{cg} - e_{ag} \quad . \quad (2.41)$$

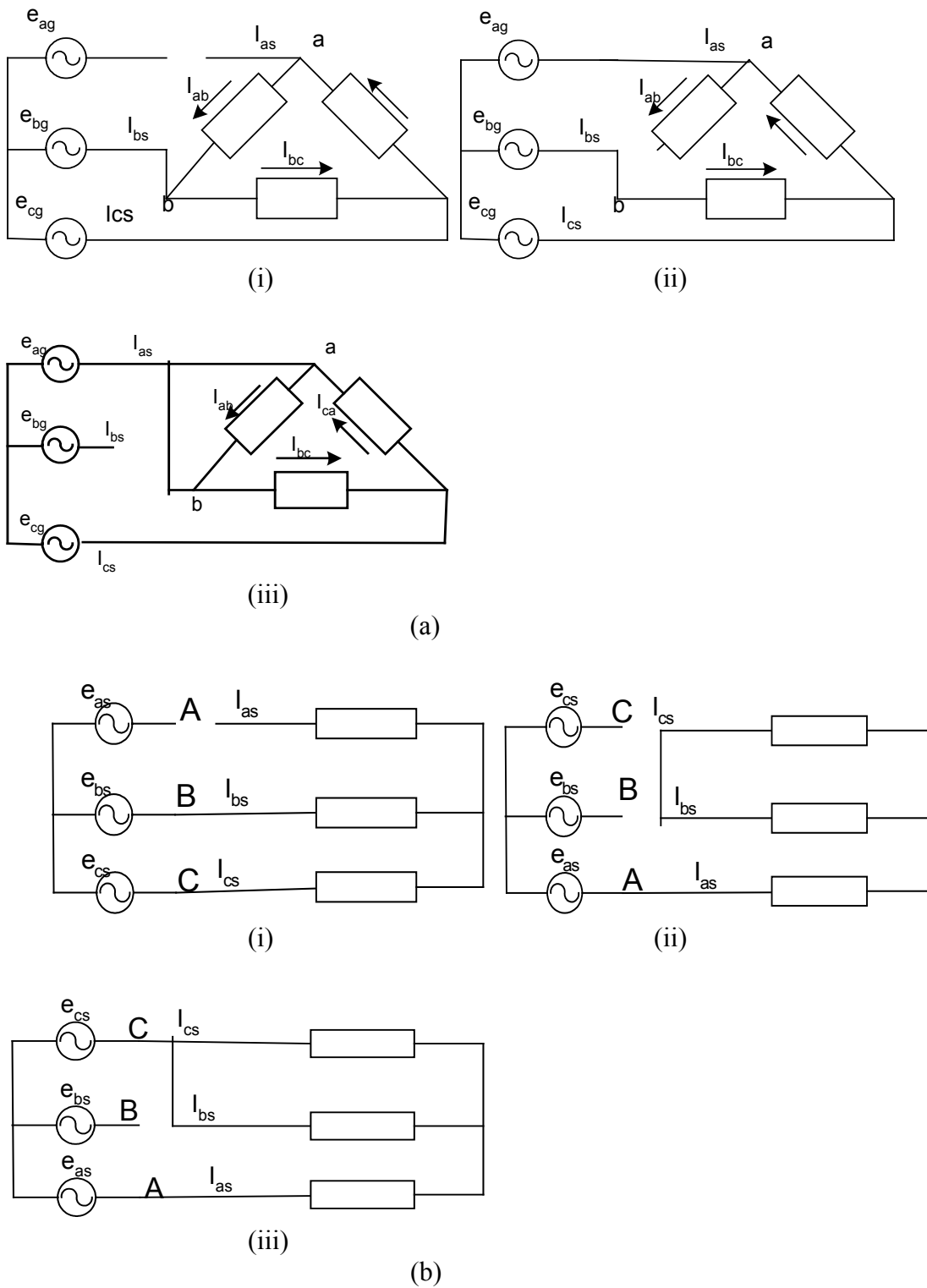


Figure 2. 1 Shows fault in (a) Delta-connected IPMSM (b) Star-connected IPMSM.

Table 2. 1 Interior Permanent Magnet Synchronous Machine Parameters

Rated Line Voltage	220 V
Stator Resistance, R_s	1.5 ohms
Stator Leakage Inductance, L_{ls}	1.6 mH
q-axis mutual Inductance, L_{mq}	0.1084H
d-axis mutual Inductance, L_{md}	0.0334H
Magnetic flux, λ_m	0.21Wb
Damper q-axis Inductance, L_{qr}	0.1195H
Damper d-axis Inductance, L_{dr}	0.0495H
Rotor Resistance, R_r	0.816 ohms
No. of Poles, P	4
Synchronous Speed, W_e	377 rad/sec
Inertia, J	0.089 kg/m2

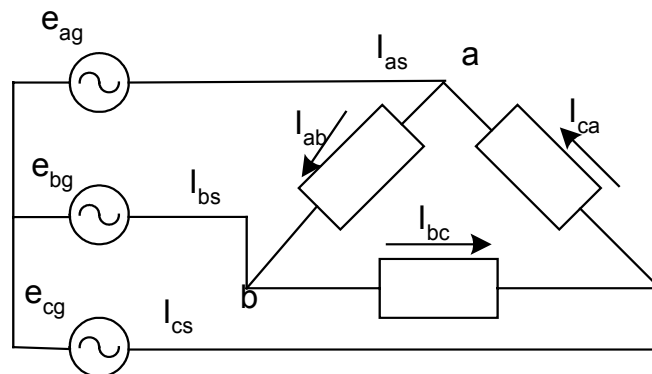


Figure 2. 2 Shows Delta-connected Stator Interior Permanent Magnet Machine

The IPMSM with delta-connected stator model is simulated with normal three-phase supply with supply line voltage of 73.5V(rms) at 60Hz and PWM-VSI supply ($V_{dc} = 200V$) at 50Hz. Figures 2.3-2.6 show the simulation results of the IPM synchronous machine under normal situation.

2.4 Fault Analysis using Stationary Reference Frame Unbalance in Delta-Connected IPMSM

2.4.1 Supply Line “A” Open-Circuit Response

Figure-2.1a (i) shows the schematic for an unbalance condition in which the supply line ‘a’ to a delta-connected stator of an IPMSM is open-circuited.

Note:

$$V_{bn} = V_{bc} = e_{bg} - e_{cg}$$

$$I_{ca} = I_{ab}$$

$$V_{ab} + V_{bc} + V_{ca} = 0 \Rightarrow V_{os}^s = 0 .$$

It can be shown for this unbalance condition that

$$V_{qs}^s = 2V_{ab}/3 - V_{bc}/3 - V_{ca}/3 = V_{ab} \quad (2.42)$$

$$V_{ds}^s = [V_{ca} - V_{bc}]/\sqrt{3} = [-V_{ab} - 2V_{bc}]/\sqrt{3} \quad (2.43)$$

$$-V_{qs}^s/\sqrt{3} = V_{ds}^s + 2V_{bc}/\sqrt{3} \quad (2.44)$$

$$I_{qs}^s = 2I_{ab}/3 - I_{bc}/3 - I_{ca}/3 = [I_{ab} - I_{bc}]/3 \quad (2.45)$$

$$I_{ds}^s = [I_{ca} - I_{bc}]/\sqrt{3} = [I_{ab} - I_{bc}]/\sqrt{3} \quad (2.46)$$

$$I_{ds}^s = \sqrt{3}I_{qs}^s \quad (2.47)$$

$$I_{os}^s = [I_{ab} + I_{bc} + I_{ca}]/3 = [2I_{ab} + I_{bc}]/3 . \quad (2.48)$$

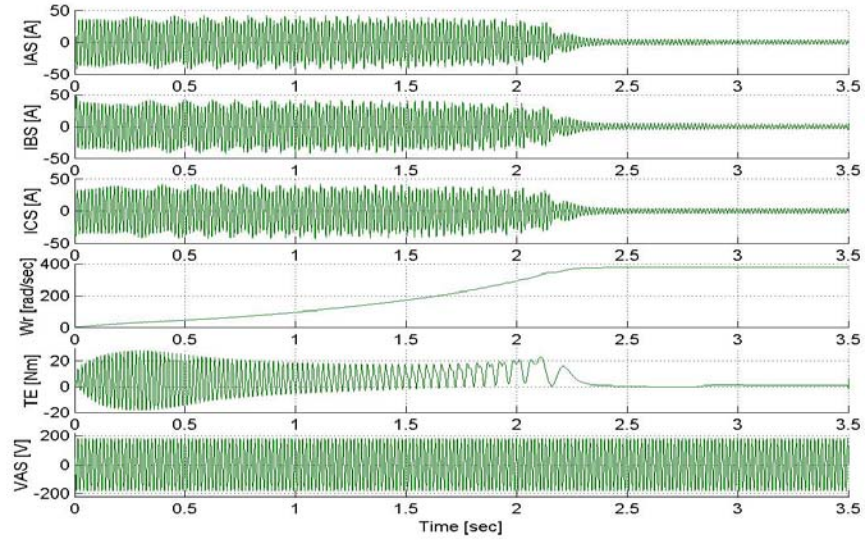


Figure 2. 3 Shows the starting transient of a delta-connected IPMSM with normal three-phase supply, from top: phase ‘a’ current, phase ‘b’ current, phase ‘c’ current, rotor speed, torque, phase ‘a’ voltage.

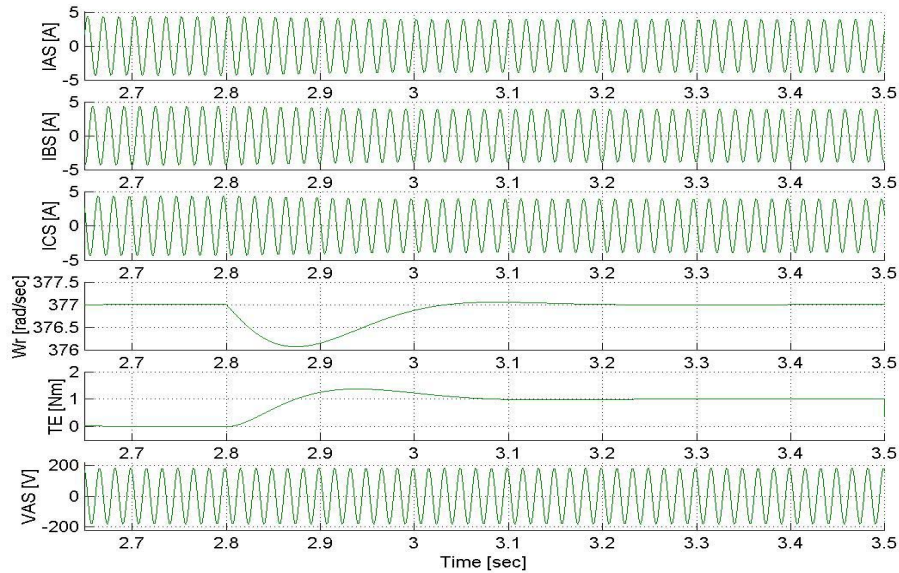


Figure 2. 4 Shows the steady state of a delta-connected IPMSM with normal three-phase supply, from top: phase ‘a’ current, phase ‘b’ current, phase ‘c’ current, rotor speed, torque, phase ‘a’ voltage.

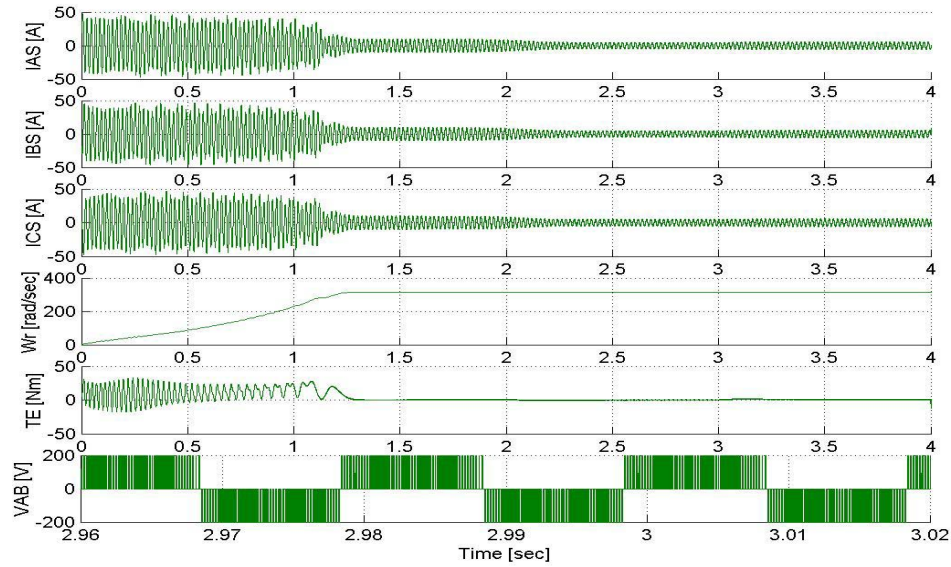


Figure 2. 5 Shows starting transient of a delta-connected IPMSM with PWM-VSI supply under Transient from top: phase ‘a’ current, phase ‘b’ current, phase ‘c’ current, rotor speed, torque, phase ‘a’ voltage.

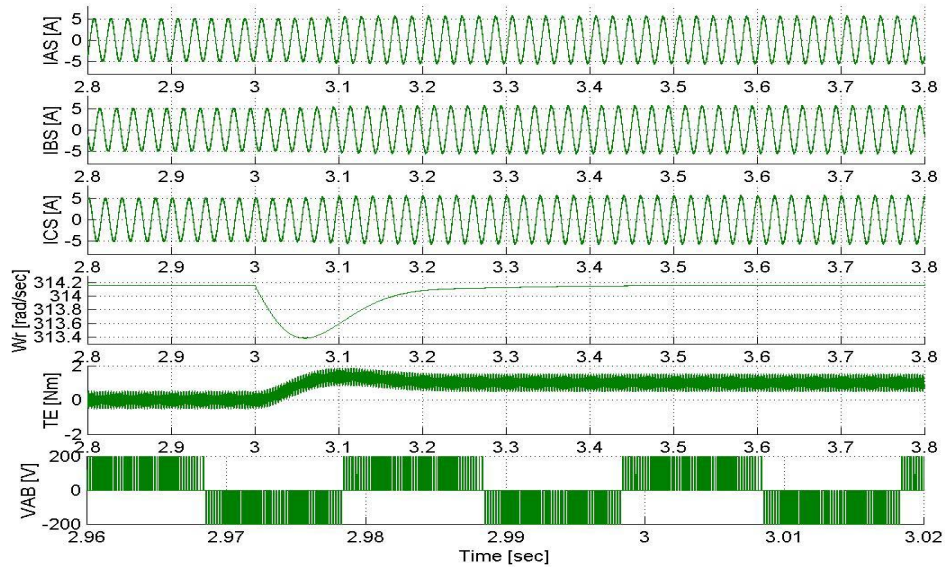


Figure 2. 6 Shows steady state of a delta-connected IPMSM with PWM-VSI supply, from top: phase ‘a’ current, phase ‘b’ current, phase ‘c’ current, rotor speed, torque, phase ‘a’ voltage.

With the supply line ‘a’ open, the knowledge of the fault conditions is established, which shows a coupling between the q-axis and d-axis.

Substitute Equations (2.28) and (2.29) in (2.44)

$$\begin{aligned} pI_{qs}^s L_1 \sin(2\theta_r) + pI_{ds}^s [L_2 + L_1 \cos(2\theta_r)] + V_x^s + 2V_{bc}/\sqrt{3} = -pI_{qs}^s [L_2 - L_1 \cos(2\theta_r)] \\ - pI_{ds}^s L_1 \sin(2\theta_r) - V_y^s/\sqrt{3} . \end{aligned} \quad (2.49)$$

Substitute Equation (2.47) in (2.49) whereby $pI_{ds}^s = \sqrt{3} pI_{qs}^s$ gives

$$pI_{qs}^s = [-V_y^s - V_x^s - 2V_{bc}]/[2\sqrt{3}L_1 \sin(2\theta_r) + 4L_2 + 2L_1 \cos(2\theta_r)] . \quad (2.50)$$

With pI_{qs}^s known, this is substituted back in Equations (2.28) and (2.29) to determine V_{qs}^s and V_{ds}^s during fault situations. Since V_{os}^s is known, then I_{os}^s can be determined.

$$V_{os}^s = I_{os}^s r_s + L_{ls} pI_{os}^s \quad (2.51)$$

The simulation results are as shown in Figures 2.7-2.8 while Figure 2.9 shows the experimental result of this fault condition.

Under this fault situation, Figures 2.7 and 2.8 the response of the IPM shows that the machine was able to maintain synchronous speed with a load of 1 Nm already applied on the machine but the machine experiences oscillation as seen on the torque and the speed. The tolerance of IPMSM was confirmed experimentally as shown in Figure 2.9. Similar changes were observed in the magnitude of the currents in all the phases.

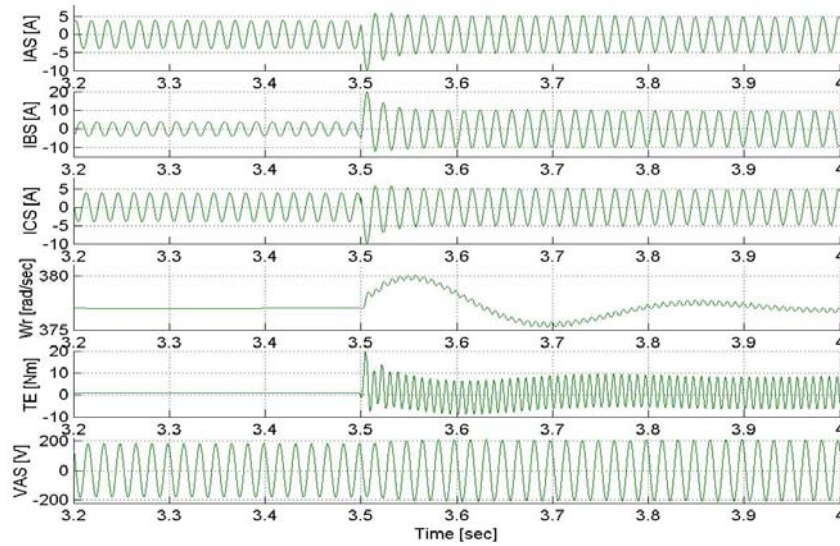


Figure 2. 7 Shows delta-connected IPMSM with a supply line open fed with a normal three-phase supply, from top: phase ‘a’ current, phase ‘b’ current, phase ‘c’ current, rotor speed, torque, phase ‘a’ voltage.

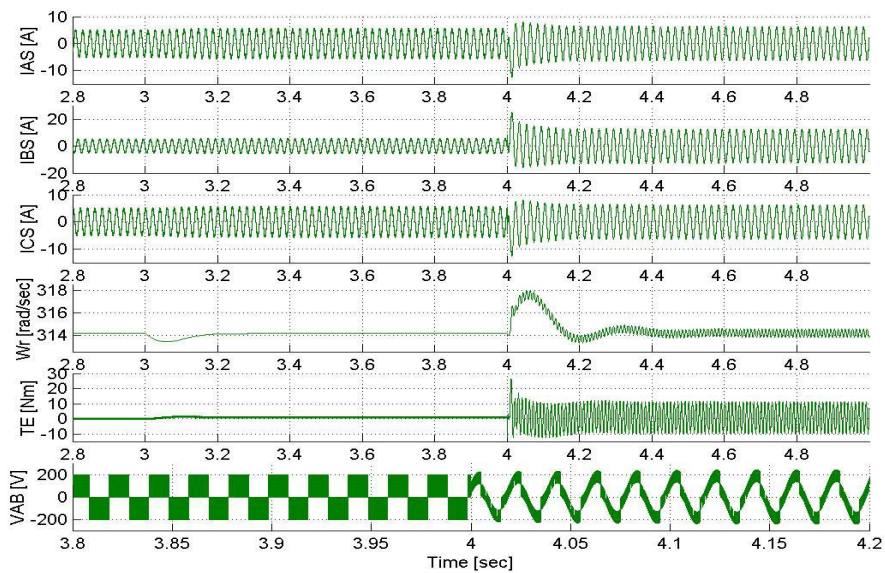


Figure 2. 8 Shows delta-connected IPMSM with a supply line open with PWM-VSI supply, from top: phase ‘a’ current, phase ‘b’ current, phase ‘c’ current, rotor speed, torque, phase ‘a’ voltage.

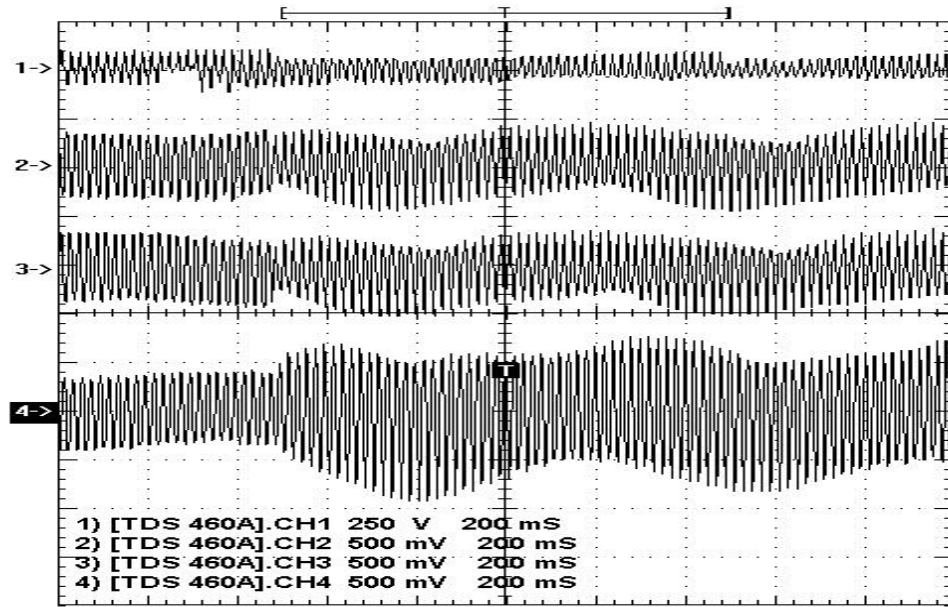


Figure 2. 9 Experimental results of phase ‘a’ line open for delta connection. (1) Inverter line-line voltage @ $V_{dc} = 90V$, (2) $I_{as} = 7A$ before and after fault, (3) $I_{cs} = 7A$ before and after fault, (4) $I_{bs} = 7A$ before and 13A after fault.

2.4.2 Stator Phase “A” Open-Circuit Response

Figure-2.1a (ii) shows the schematic of an unbalance in which the stator phase ‘a’ of the delta-connected IPMSM is opened.

The machine is analyze and it can be shown that the following equations apply.

Note:

$$I_{ab} = 0$$

$$V_{bn} = V_{bc} = e_{bg} - e_{cg}$$

$$V_{cn} = V_{ca} = e_{cg} - e_{ag}$$

$$e_{bg} - e_{ag} = V_{bc} + V_{ca} .$$

Hence, after simplifications, it can be shown that

$$\begin{aligned} V_{qs}^s &= 2V_{ab}/3 - V_{bc}/3 - V_{ca}/3 \\ &= 2V_{ab}/3 - [e_{bg} - e_{ag}]/3 \end{aligned} \quad (2.52)$$

$$V_{ds}^s = [V_{ca} - V_{bc}]/\sqrt{3} . \quad (2.53)$$

Simplifying further gives

$$I_{qs}^s = -I_{os}^s \quad (2.54)$$

$$V_{qs}^s = 2V_{os}^s + e_{ag} - e_{bg} \quad (2.55)$$

$$V_{os}^s = I_{os}^s r_s + L_{ls} p I_{os}^s \quad (2.56)$$

$$V_{qs}^s = e_{ag} - e_{bg} - 2I_{os}^s r_s - 2L_{ls} p I_{os}^s \quad (2.57)$$

$$I_{ab} = I_{qs}^s - I_{os}^s = 0 \quad (2.58)$$

$$I_{bc} = -I_{qs}^s/2 - \sqrt{3}I_{ds}^s/2 - I_{os}^s = -3I_{qs}^s/2 - \sqrt{3}I_{ds}^s/2 \quad (2.59)$$

$$I_{ca} = -I_{qs}^s/2 + \sqrt{3}I_{ds}^s/2 - I_{os}^s = -3I_{qs}^s/2 + \sqrt{3}I_{ds}^s/2 . \quad (2.60)$$

As already shown above, the phase 'a' of the machine is open-circuited which means $I_{ab} = 0$; it has been shown that $I_{qs}^s = -I_{os}^s$ and $V_{qs}^s = 2V_{os}^s + e_{ag} - e_{bg}$, these conditions are necessary and sufficient in the simulation of this fault situation.

From above, V_{ds}^s is known, therefore solving Equations (2.28) and (2.29) for V_{qs}^s , pI_{qs}^s , and pI_{ds}^s becomes

$$V_{ds}^s - V_x^s = pI_{qs}^s L_1 \sin(2\theta_r) + pI_{ds}^s [L_2 + L_1 \cos(2\theta_r)] \quad (2.61)$$

$$V_{qs}^s - V_y^s = pI_{qs}^s [L_2 - L_1 \cos(2\theta_r)] + pI_{ds}^s L_1 \sin(2\theta_r) . \quad (2.62)$$

From Equation (2.61),

$$pI_{ds}^s = [V_{ds}^s - V_x^s - pI_{qs}^s L_1 \sin(2\theta_r)] / [L_2 + L_1 \cos(2\theta_r)] . \quad (2.63)$$

Substitute (2.63) in (2.62),

$$L_{dd}L_{qq} pI_{qs}^s + V_{ds}^s L_1 \sin(2\theta_r) - V_x^s L_1 \sin(2\theta_r) = [L_2 + L_1 \cos(2\theta_r)] [V_{qs}^s - V_y^s] . \quad (2.64)$$

From (2.64), it can be shown that

$$pI_{qs}^s = [V_{qs}^s [L_2 + L_1 \cos(2\theta_r)] - V_y^s L_2 - [V_y^s L_1 \cos(2\theta_r) - V_x^s L_1 \sin(2\theta_r)] - V_{ds}^s L_1 \sin(2\theta_r)] / L_{dd}L_{qq} ; \quad (2.65)$$

therefore pI_{qs}^s and V_{qs}^s can be determined by solving Equations (2.65) and (2.57). Hence, substituting Equation (2.65) in Equation (2.57) gives

$$V_{qs}^s = e_a - e_b - 2r_s I_{qs}^s + 2L_{ls} [V_{qs}^s [L_2 + L_1 \cos(2\theta_r)] - V_y^s L_2 - [V_y^s L_1 \cos(2\theta_r) - V_x^s L_1 \sin(2\theta_r)] - V_{ds}^s L_1 \sin(2\theta_r)] / L_{dd}L_{qq} .$$

Simplifying gives

$$V_{qs}^s [1 - 2L_{ls} [L_2 + L_1 \cos(2\theta_r)] / L_{dd}L_{qq}] = e_a - e_b - 2r_s I_{qs}^s + 2L_{ls} [-V_y^s L_2 - [V_y^s L_1 \cos(2\theta_r) - V_x^s L_1 \sin(2\theta_r)] - V_{ds}^s L_1 \sin(2\theta_r)] / L_{dd}L_{qq} . \quad (2.66)$$

Note:

$$[V_y^s L_1 \cos(2\theta_r) - V_x^s L_1 \sin(2\theta_r)] = r_s L_1 [I_{qs}^s \cos(2\theta_r) - I_{ds}^s \sin(2\theta_r)] + p\lambda_{qr}^s [L_1 L_4 \cos(2\theta_r) - L_1 L_3] - p\lambda_{dr}^s L_1 L_4 \sin(2\theta_r) + \omega_r I_{ds}^s 2L_1^2 + \lambda_{dr}^s \omega_r 2L_1 L_3 + \lambda_m \omega_r L_1 \cos(\theta_r) .$$

V_{qs}^s is obtained from Equation (2.66) and substituted back in (2.65) which is now substituted in (2.63).

The simulation results are as shown in Figures 2.10 – 2.11 while the experimental result with PWM-VSI supply is as shown in Figure 2.12. Both simulation and experiment shows similar changes in current flowing in the stator phases. Figures 2.10, 2.11, and 2.12 show that the magnitude of the current in phase ‘b’ is highest during this fault situation and that zero current flows through phase ‘a’. The IPMSM was able to maintain synchronous speed during this fault situation after some initial transient when the fault

occurs. As would be expected, the motor oscillates during this unbalance as will be seen in the torque and the speed in Figures 2.10 and 2.11.

2.4.3 Shorted Stator Phase “A” Open-Circuit Response

Figure-2.1a (iii) shows the schematic of an unbalance in which the stator phase ‘a’ of the delta-connected IPMSM is shorted and supply line ‘b’ is open.

The machine is analyze and it can be shown that the following equations apply.

Note:

$$V_{ab} = 0$$

$$V_{bc} = e_{ag} - e_{cg}$$

$$V_{ca} = e_{cg} - e_{ag} .$$

Hence,

$$V_{qs}^s = -[V_{bc} + V_{ca}]/3 = 0 \quad (2.67)$$

$$V_{ds}^s = [V_{ca} - V_{bc}]/\sqrt{3} = 2[e_c - e_a]/\sqrt{3} \quad (2.68)$$

$$V_{os}^s = [V_{ab} + V_{bc} + V_{ca}]/3 = 0 .$$

With V_{qs}^s and V_{ds}^s known, then solving Equations (2.32) and (2.33) gives pI_{qs}^s and pI_{ds}^s , respectively. The simulation results are as shown in Figures 2.13-2.14. Though the IPMSM was able to maintain synchronous speed, the magnitudes of the stator currents are high.

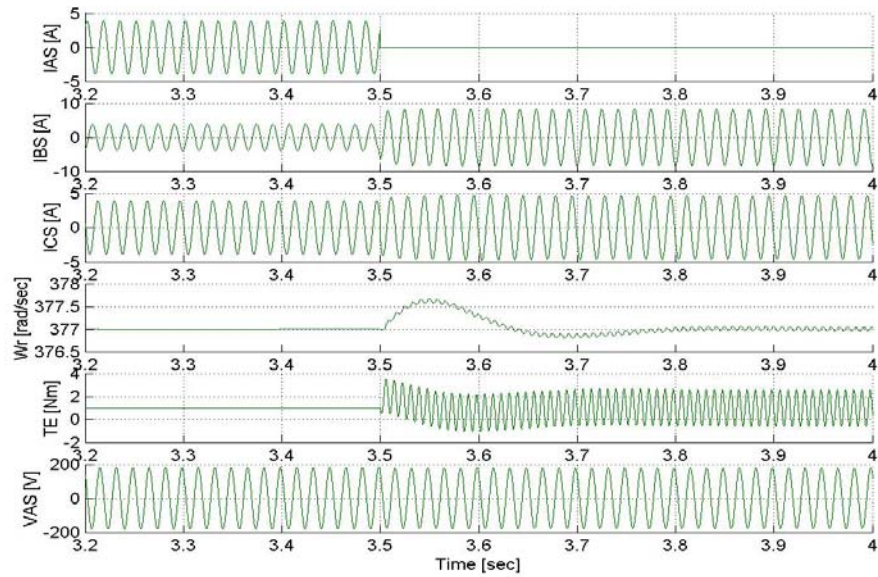


Figure 2. 10 Shows Delta-connected IPMSM for stator phase open with Normal three-phase supply from top: phase ‘a’ current, phase ‘b’ current, phase ‘c’ current, rotor speed, torque, phase ‘a’ voltage.

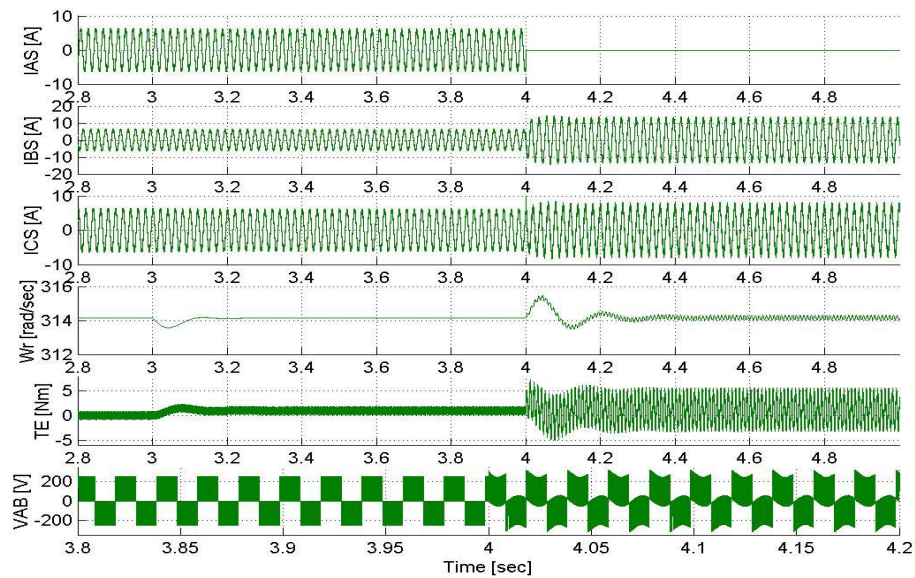


Figure 2. 11 Shows Delta-connected IPMSM for stator phase open with PWM-VSI from top: phase ‘a’ current, phase ‘b’ current, phase ‘c’ current, rotor speed, torque, phase ‘a’ voltage.

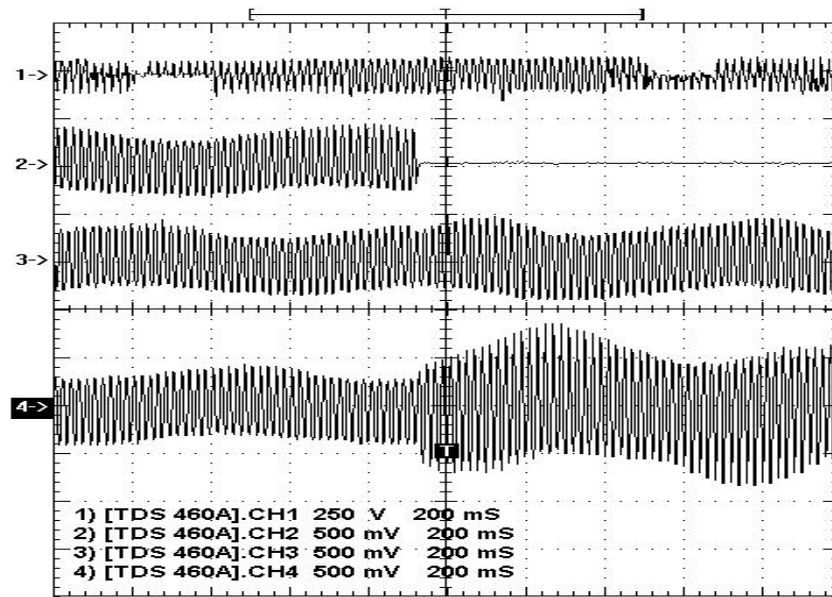


Figure 2. 12 Experimental results of phase ‘a’ winding open for delta connection. (1) Inverter line-line voltage @ $V_{dc} = 90V$, (2) $I_{as} = 5A$ before and $0A$ after fault, (3) $I_{cs} = 5A$ before and $6.5A$ after fault, (4) $I_{bs} = 5A$ before and $13A$ after fault.

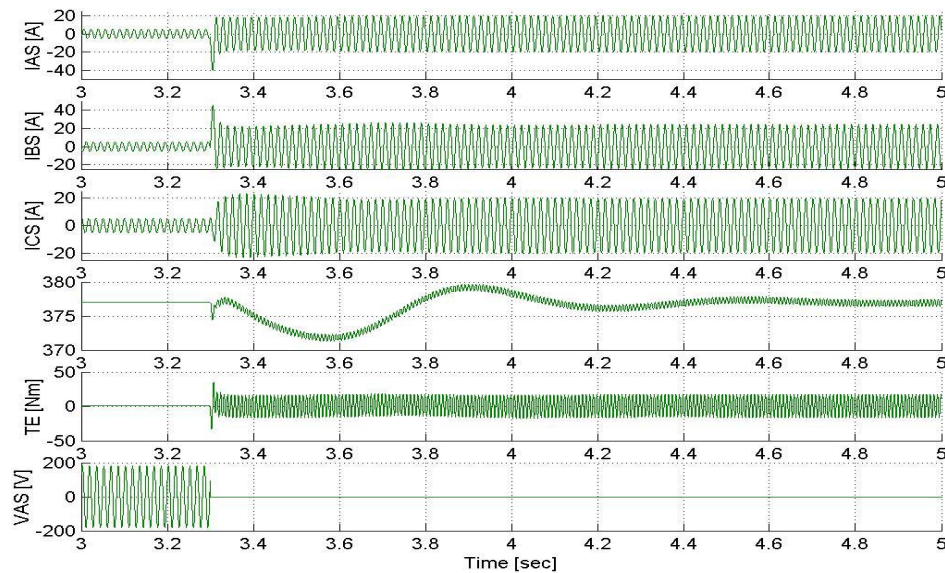


Figure 2. 13 Shows Delta-connected IPMSM for shorted stator phase with Normal three-phase supply from top: phase ‘a’ current, phase ‘b’ current, phase ‘c’ current, rotor speed, torque, phase ‘a’ voltage.

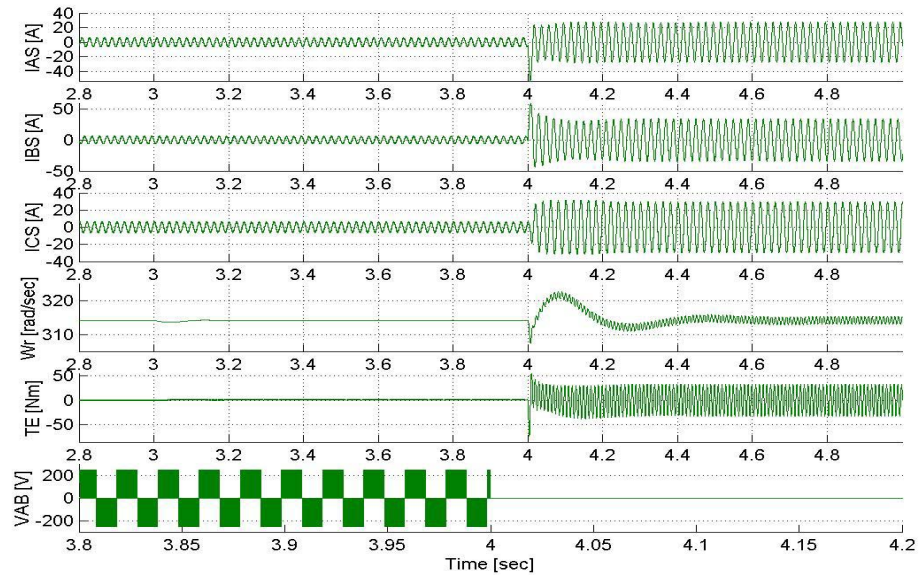


Figure 2. 14 Shows Delta-connected IPMSM for shorted stator phase with PWM-VSI from top: phase ‘a’ current, phase ‘b’ current, phase ‘c’ current, rotor speed, torque, phase ‘a’ voltage.

2.5 Star-Connected Stator

The star-connected stator interior permanent magnet synchronous machine is as shown in Figure 2.15 and the phase voltages can be expressed as follows:

$$e_{ag} = V_{as} + V_{sn} \quad (2.69)$$

$$e_{bg} = V_{bs} + V_{sn} \quad (2.70)$$

$$e_{cg} = V_{cs} + V_{sn} . \quad (2.71)$$

The IPMSM with star-connected stator model is simulated with normal three-phase supply with supply line voltage of 220-V (rms) at 60Hz and PWM-VSI supply with V_{dc}

of 250V at 50Hz with a load of 1Nm. Figures 2.16-2.19 show the simulation results under no fault situations.

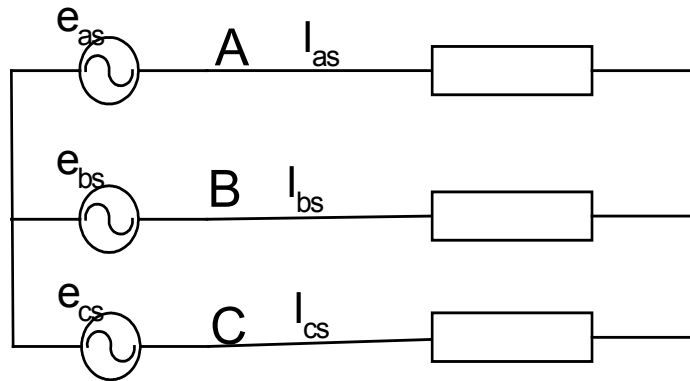


Figure 2. 15 Shows Star-connected stator Interior Permanent Magnet Machine

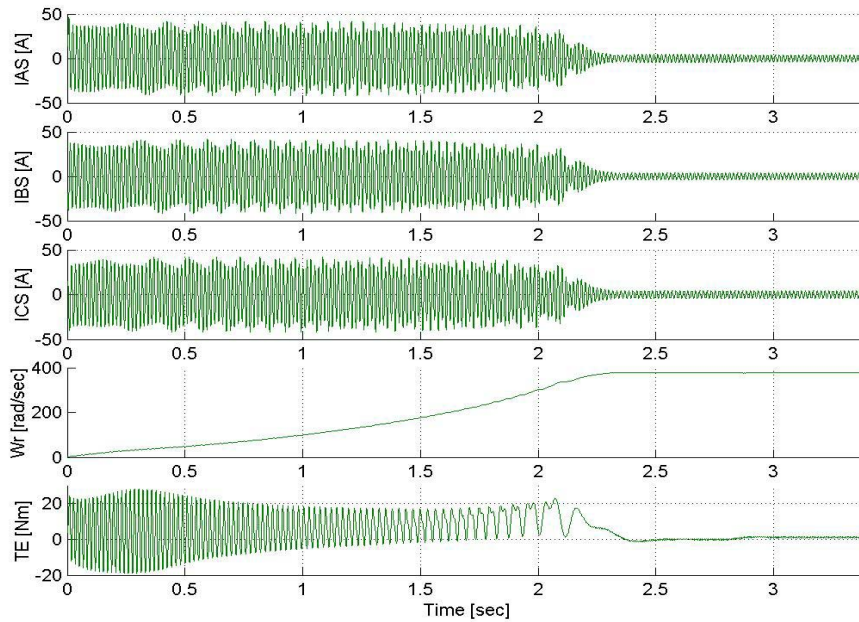


Figure 2. 16 Shows starting transient of a star-connected IPMSM with normal three-phase supply, from top: phase ‘a’ current, phase ‘b’ current, phase ‘c’ current, rotor speed, torque.

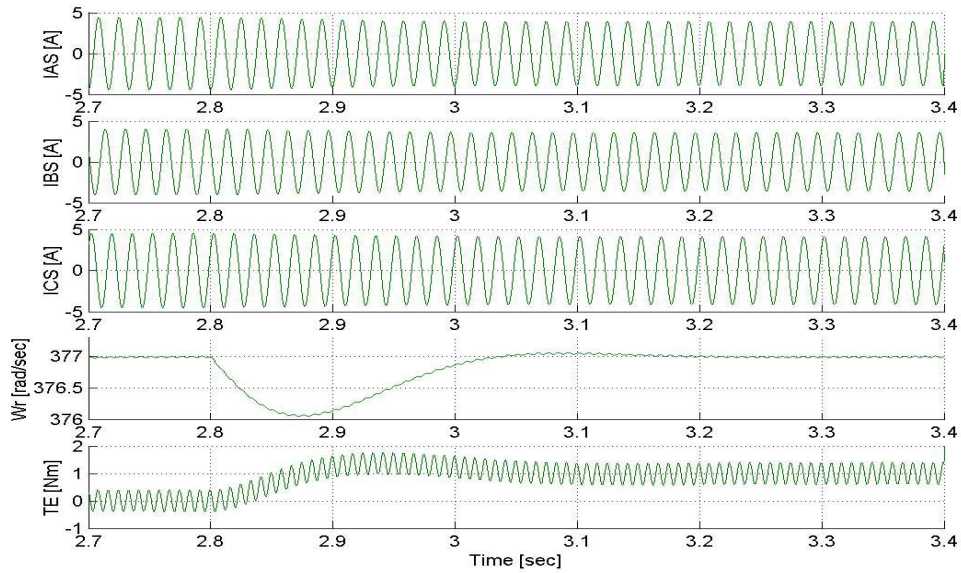


Figure 2. 17 Shows steady state of a star-connected IPMSM with normal three-phase supply under Steady-state from top: phase ‘a’ current, phase ‘b’ current, phase ‘c’ current, rotor speed, torque.

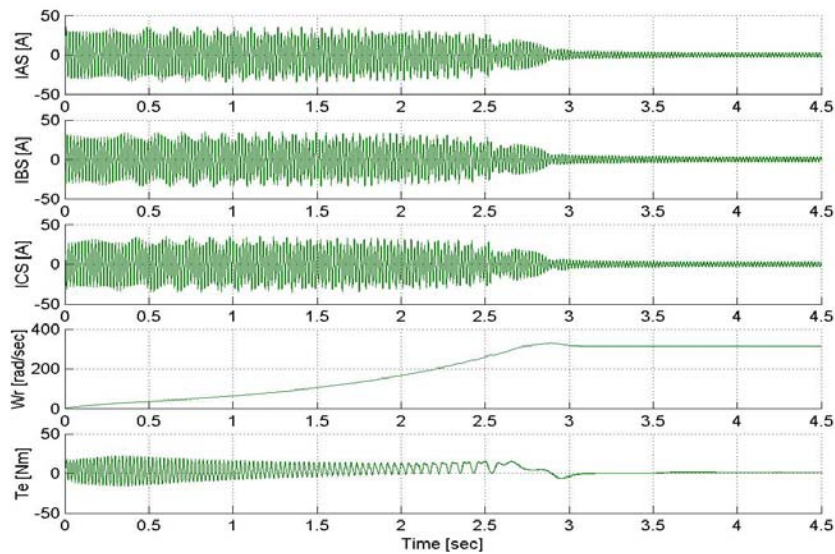


Figure 2. 18 Shows starting transient of a star-connected IPMSM with PWM-VSI supply, from top: phase ‘a’ current, phase ‘b’ current, phase ‘c’ current, rotor speed, torque.

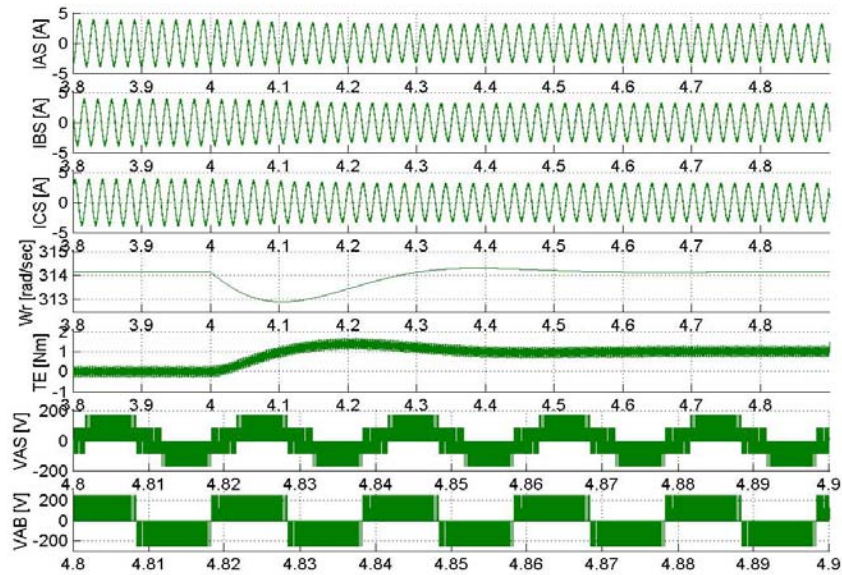


Figure 2. 19 Shows steady state of a star-connected IPMSM with PWM-VSI supply, from top: phase ‘a’ current, phase ‘b’ current, phase ‘c’ current, rotor speed, torque, phase ‘a’ voltage, line voltage.

2.6 Fault Analysis using Stationary Reference Frame Unbalance in Star-Connected IPMSM

2.6.1 Supply Line “A” Open-Circuit Response

Figure-2.1b (i) shows the schematic for an unbalance condition in which the supply line ‘a’ to a star-connected stator of an IPMSM is open-circuited.

With the supply line ‘a’ open,

$$I_{as} = 0$$

$$I_{as} + I_{bs} + I_{cs} = 0 \Rightarrow I_{bs} = -I_{cs} .$$

Hence,

$$I_{qs}^s = 2I_{as}/3 - I_{bs}/3 - I_{cs}/3 = 0 \quad (2.72)$$

$$I_{as} + I_{bs} + I_{cs} = 0 \Rightarrow I_{os} = 0 \quad (2.73)$$

$$I_{ds}^s = [I_{cs} - I_{bs}]/\sqrt{3} = 2I_{cs}/\sqrt{3} \quad (2.74)$$

$$V_{os} = [V_{as} + V_{bs} + V_{cs}]/3 \quad (2.75)$$

$$V_{qs}^s = 2V_{as}/3 - V_{bs}/3 - V_{cs}/3 . \quad (2.76)$$

From (2.70),

$$2V_{os} = [2V_{as} + 2V_{bs} + 2V_{cs}]/3 . \quad (2.77)$$

Hence,

$$V_{qs}^s = 2V_{os} - V_{bs} - V_{cs} \Rightarrow V_{os} + V_{qs}^s = V_{as} \quad (2.78)$$

$$V_{ds}^s = [V_{cs} - V_{bs}]/\sqrt{3} = [e_{cg} - e_{bg}]/\sqrt{3} . \quad (2.79)$$

Two fault conditions has been established from above ($I_{qs}^s = 0$ and $V_{ds}^s = [e_{cg} - e_{bg}]/\sqrt{3}$)

which is sufficient in simulating this fault situation.

Hence from Equation (2.72),

$$pI_{qs}^s = 0 . \quad (2.80)$$

Substituting Equations (2.80) and (2.72) in (2.28) and (2.29) reduces to

$$\begin{aligned} V_{qs}^s = & pI_{ds}^s L_1 \sin(2\theta_r) + p\lambda_{qr}^s [L_4 - L_3 \cos(2\theta_r)] + p\lambda_{dr}^s L_3 \sin(2\theta_r) + \omega_r [I_{ds}^s 2L_1 \cos(2\theta_r) \\ & + \lambda_{qr}^s 2L_3 \sin(2\theta_r) + \lambda_{dr}^s 2L_3 \cos(2\theta_r) + \lambda_{mm} \cos(\theta_r)] \end{aligned} \quad (2.81)$$

$$\begin{aligned} V_{ds}^s = & r_s I_{ds}^s + pI_{ds}^s [L_2 + L_1 \cos(2\theta_r)] + p\lambda_{qr}^s L_3 \sin(2\theta_r) + p\lambda_{dr}^s [L_4 + L_3 \cos(2\theta_r)] \\ & + \omega_r [-I_{ds}^s 2L_1 \sin(2\theta_r) + \lambda_{qr}^s 2L_3 \cos(2\theta_r) - \lambda_{dr}^s 2L_3 \sin(2\theta_r) - \lambda_{mm} \sin(\theta_r)] . \end{aligned} \quad (2.82)$$

Since V_{ds}^s is known from the conditions above, then pI_{ds}^s can be determined from (2.82)

as follows:

$$pI_{ds}^s [L_2 + L_1 \cos(2\theta_r)] = V_{ds}^s - r_s I_{ds}^s - p\lambda_{qr}^s L_3 \sin(2\theta_r) - p\lambda_{dr}^s [L_4 + L_3 \cos(2\theta_r)] \\ - \omega_r [-I_{ds}^s 2L_1 \sin(2\theta_r) + \lambda_{qr}^s 2L_3 \cos(2\theta_r) - \lambda_{dr}^s 2L_3 \sin(2\theta_r) - \lambda_{mm} \sin(\theta_r)] \quad .$$

Simplifying for pI_{ds}^s from above reduces to

$$pI_{ds}^s = (V_{ds}^s - r_s I_{ds}^s - p\lambda_{qr}^s L_3 \sin(2\theta_r) - p\lambda_{dr}^s [L_4 + L_3 \cos(2\theta_r)] - \omega_r [-I_{ds}^s 2L_1 \sin(2\theta_r) \\ + \lambda_{qr}^s 2L_3 \cos(2\theta_r) - \lambda_{dr}^s 2L_3 \sin(2\theta_r) - \lambda_{mm} \sin(\theta_r)]) / [L_2 + L_1 \cos(2\theta_r)] \quad . \quad (2.83)$$

Substituting (2.83) in (2.81) gives V_{qs}^s as

$$V_{qs}^s [L_2 + L_1 \cos(2\theta_r)] = p\lambda_{qr}^s [L_2 L_4 - L_2 L_3 \cos(2\theta_r) + L_1 L_4 \cos(2\theta_r) - L_1 L_3] \\ + p\lambda_{dr}^s \sin(2\theta_r) [L_2 L_3 - L_1 L_4] + \omega_r \lambda_{qr}^s 2L_2 L_3 \sin(2\theta_r) + \omega_r \lambda_{dr}^s 2L_3 [L_2 \cos(2\theta_r) + L_1] \\ + I_{ds}^s \omega_r [2L_1 L_2 \cos(2\theta_r) + 2L_1^2 - r_s L_1 \sin(2\theta_r) / \omega_r] + \omega_r \lambda_{mm} \cos(\theta_r) L_{dd} \\ + V_{ds}^s L_1 \sin(2\theta_r). \quad (2.84)$$

The following simulation results for this fault are shown in Figures 2.20 – 2.21, and the experimental result is as shown in Figure 2.22.

The simulation results show that the machine was able to exhibit some tolerance during fault situation; this is shown from the synchronous speed, which remains constant after an initial transient.

Experimental and simulation results shows that the current in phase ‘a’ is zero while in other phases, the currents changed to approximately an equal value, the machine also oscillates while the fault persist.

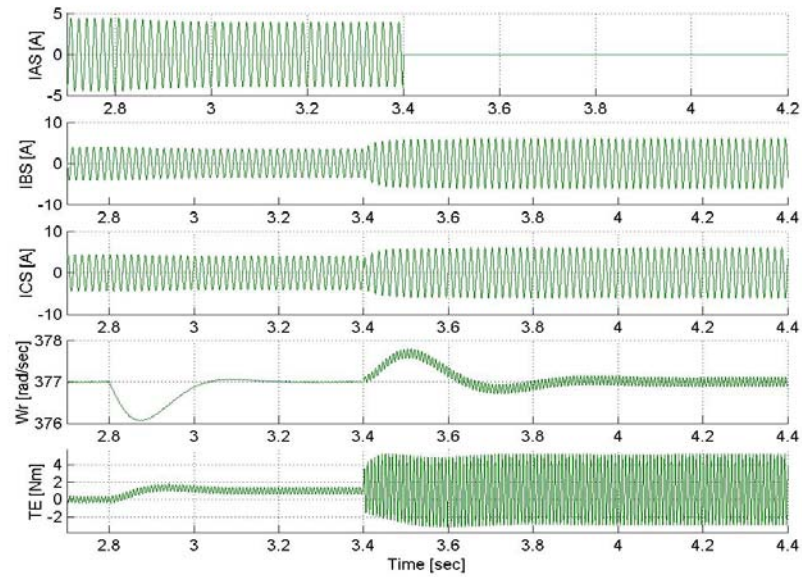


Figure 2. 20 Shows star-connected IPMSM for supply line open with normal three-phase supply from top: phase ‘a’ current, phase ‘b’ current, phase ‘c’ current, rotor speed, torque.

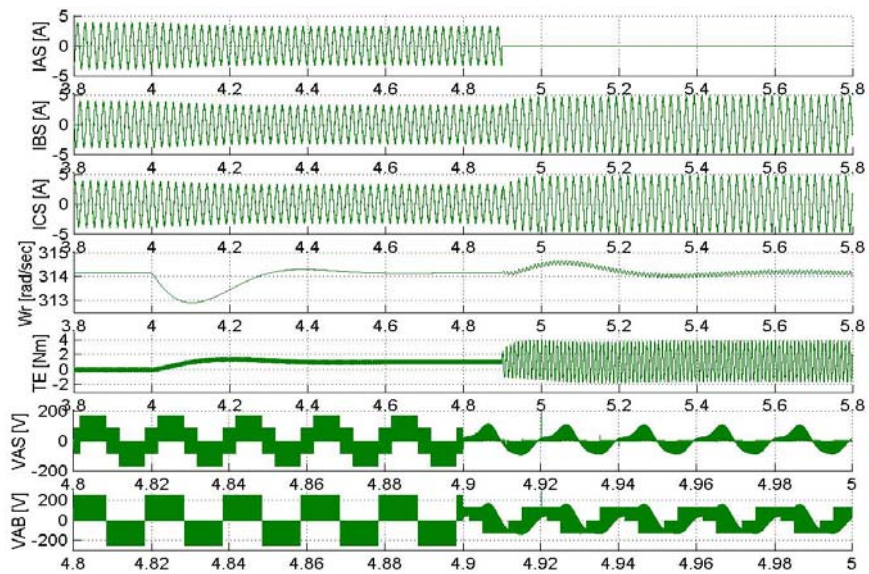


Figure 2. 21 Shows star-connected IPMSM for supply line open with PWM-VSI from top: phase ‘a’ current, phase ‘b’ current, phase ‘c’ current, rotor speed, torque, phase ‘a’ voltage, line voltage.

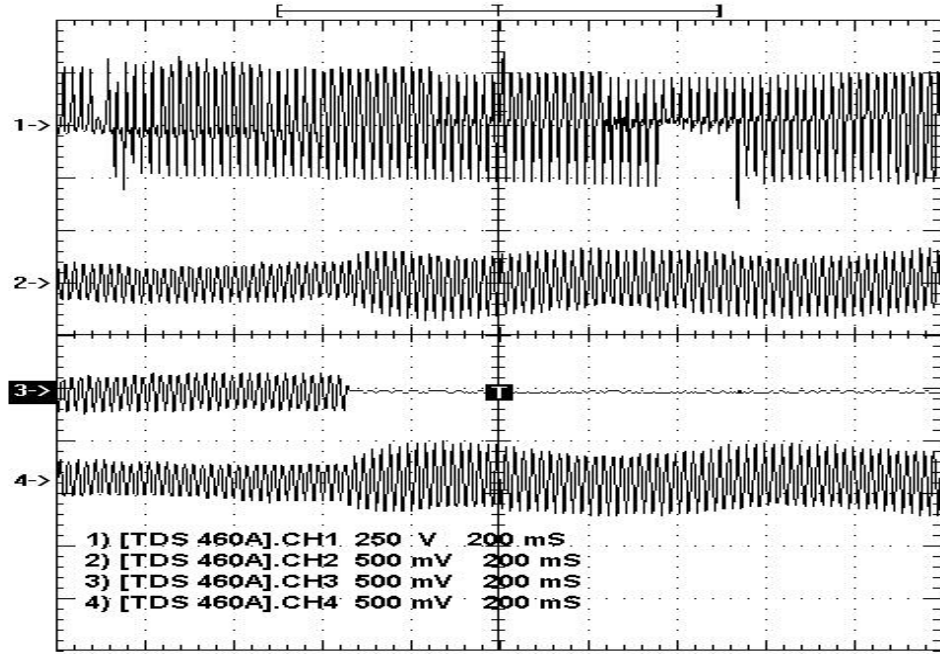


Figure 2. 22 Experimental results of three-leg IPM motor with phase ‘a’ open. (1) Inverter line-line voltage @ $V_{dc} = 250V$, (2) $I_{as} = 3A$ before and $5A$ after fault, (3) $I_{ca} = 3A$ before and $0A$ after fault, (4) $I_{bc} = 3A$ before and $5A$ after fault.

2.6.2 Supply Line-to-Line Fault Response

Figure-2.1b (ii) shows the schematic for an unbalance condition in which the supply line ‘b’ and ‘c’ of a star-connected stator of an IPMSM are short-circuited and the corresponding supply line is open-circuited. From Figure 2.1b(ii),

$$e_{ag} = V_{as} + V_{sn}$$

$$V_{bs} = V_{cs} .$$

Hence,

$$V_{ds}^s = [V_{cs} - V_{bs}]/\sqrt{3} = 0 \quad (2.85)$$

$$V_{qs}^s = 2V_{as}/3 - V_{bs}/3 - V_{cs}/3 = 2V_{as}/3 - 2V_{bs}/3 . \quad (2.86)$$

Also,

$$I_{cs} = -I_{bs}$$

$$I_{as} + I_{bs} + I_{cs} = 0 \Rightarrow I_{as} = 0$$

$$I_{qs}^s = 2I_{as}/3 - I_{bs}/3 - I_{cs}/3 = 0 \quad (2.87)$$

$$I_{ds}^s = [I_{cs} - I_{bs}]/\sqrt{3} = 2I_{cs}/\sqrt{3} . \quad (2.88)$$

With $V_{ds}^s = 0$ and $I_{qs}^s = 0 \Rightarrow pI_{qs}^s = 0$, solving Equations (2.29) and (2.28),

$$\begin{aligned} 0 &= r_s I_{ds}^s + pI_{ds}^s [L_2 + L_1 \cos(2\theta_r)] + p\lambda_{qr}^s L_3 \sin(2\theta_r) + p\lambda_{dr}^s [L_4 + L_3 \cos(2\theta_r)] \\ &+ \omega_r [-I_{ds}^s 2L_1 \sin(2\theta_r) + \lambda_{qr}^s 2L_3 \cos(2\theta_r) - \lambda_{dr}^s 2L_3 \sin(2\theta_r) - \lambda_{mm} \sin(\theta_r)] \\ pI_{ds}^s [L_2 + L_1 \cos(2\theta_r)] &= -r_s I_{ds}^s - p\lambda_{qr}^s L_3 \sin(2\theta_r) - p\lambda_{dr}^s [L_4 + L_3 \cos(2\theta_r)] \\ &- \omega_r [-I_{ds}^s 2L_1 \sin(2\theta_r) + \lambda_{qr}^s 2L_3 \cos(2\theta_r) - \lambda_{dr}^s 2L_3 \sin(2\theta_r) - \lambda_{mm} \sin(\theta_r)] \end{aligned} \quad (2.89)$$

$$\begin{aligned} V_{qs}^s &= pI_{ds}^s L_1 \sin(2\theta_r) + p\lambda_{qr}^s [L_4 - L_3 \cos(2\theta_r)] + p\lambda_{dr}^s L_3 \sin(2\theta_r) \\ &+ \omega_r [I_{ds}^s 2L_1 \cos(2\theta_r) + \lambda_{qr}^s 2L_3 \sin(2\theta_r) + \lambda_{dr}^s 2L_3 \cos(2\theta_r) + \lambda_{mm} \cos(\theta_r)] . \end{aligned} \quad (2.90)$$

Since pI_{ds}^s is known, then V_{qs}^s can be determined. The simulation results in Figures 2.23-2.24 show that a circulating current is flowing in phase 'b' and 'c' while phase 'a' current is zero. The speed drops and the IPMSM went into generating mode showing the severity of this fault situation.

2.6.3 Shorted Stator Phases

Figure-2.1b (iii) shows the schematic for an unbalance condition in which the supply line 'b' and 'c' of a star-connected stator of an IPMSM are short-circuited and

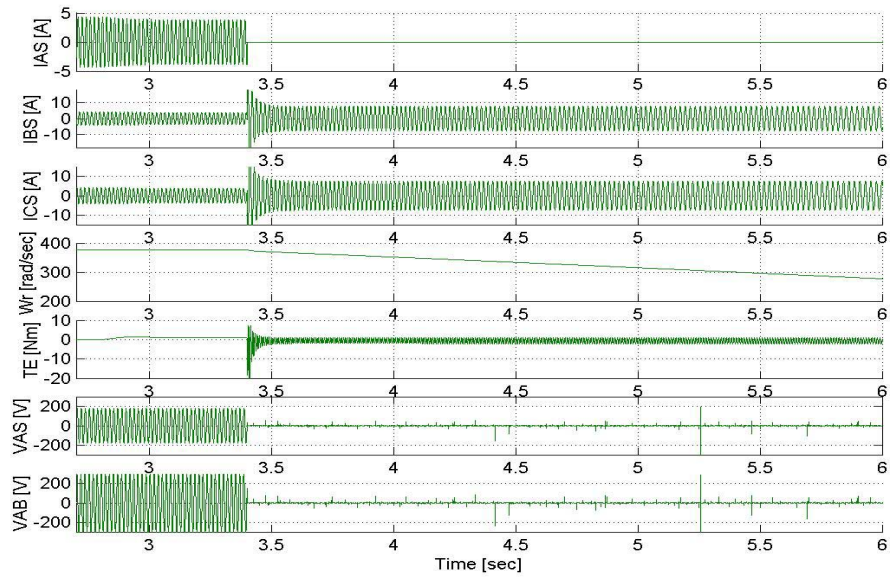


Figure 2. 23 Shows star-connected IPMSM for line-line fault with normal three-phase supply from top: phase 'a' current, phase 'b' current, phase 'c' current, rotor speed, torque, phase 'a' voltage, line voltage.

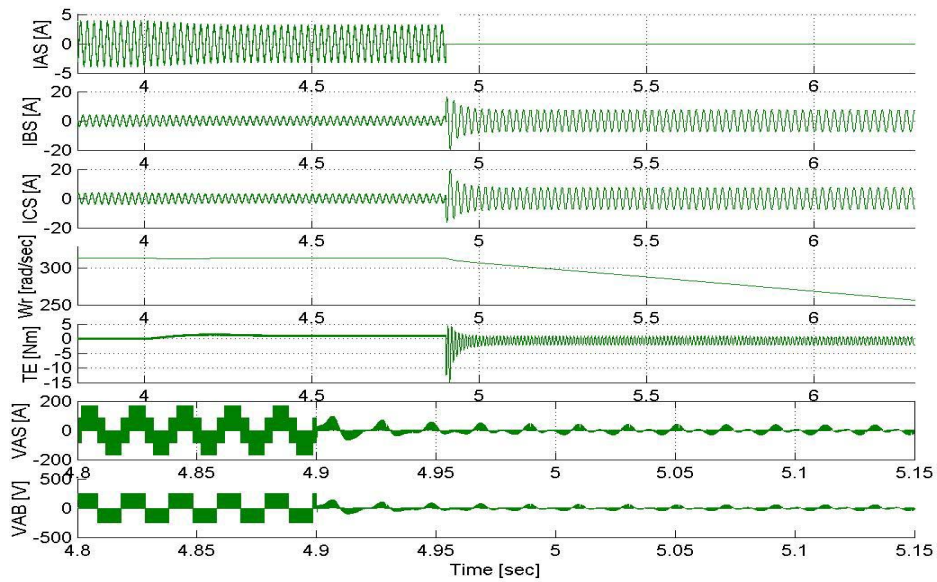


Figure 2. 24 Shows star-connected IPMSM for line-line fault with PWM-VSI from top: phase 'a' current, phase 'b' current, phase 'c' current, rotor speed, torque, phase 'a' voltage, line voltage.

supply line 'b' is open-circuited. From Figure 2.1b(iii):

$$e_{ag} = V_{as} + V_{sn}$$

$$e_{bg} = V_{cs} + V_{sn}$$

$$e_{cg} = V_{cs} + V_{sn} .$$

Hence,

$$V_{bs} = V_{cs} .$$

Therefore,

$$\begin{aligned} V_{qs}^s &= 2V_{as}/3 - V_{bs}/3 - V_{cs}/3 = 2V_{as}/3 - 2V_{bs}/3 \\ &= 2[e_{ag} - e_{cg}]/3 \end{aligned} \quad (2.91)$$

$$V_{ds}^s = [V_{cs} - V_{bs}]/\sqrt{3} = 0 \quad (2.92)$$

$$I_{as} + I_{bs} + I_{cs} = 0 \Rightarrow I_{os} = 0 . \quad (2.93)$$

Substitute Equations (2.91) and (2.92) in Equations (2.32) and (2.33), this give the value of pI_{qs}^s and pI_{ds}^s necessary for the simulation for this fault situation. Figures 2.25-2.26 show a large increase in current flowing through the stator phase of the IPMSM even though the machine was able to run at synchronous speed.

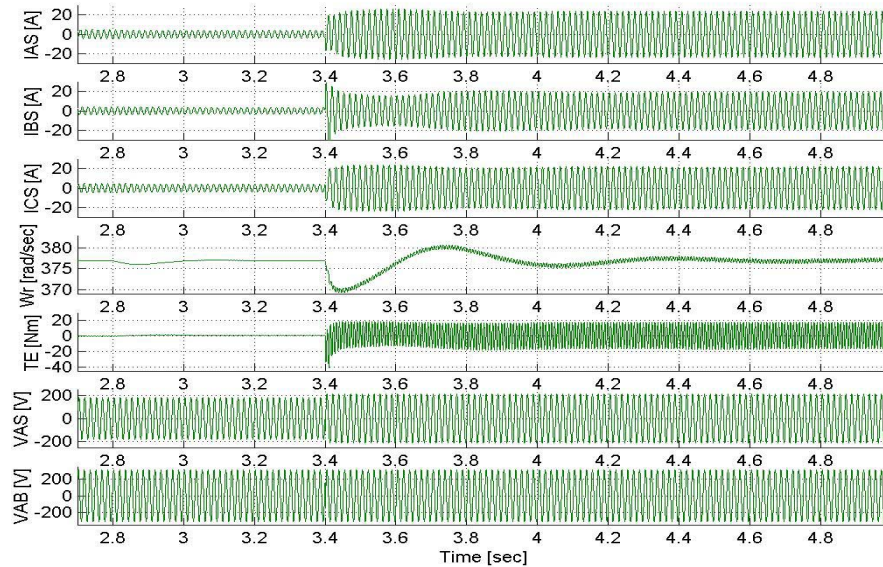


Figure 2. 25 Shows star-connected IPMSM for shorted stator phase with normal three-phase supply from top: phase 'a' current, phase 'b' current, phase 'c' current, rotor speed, torque, phase 'a' voltage, line voltage.

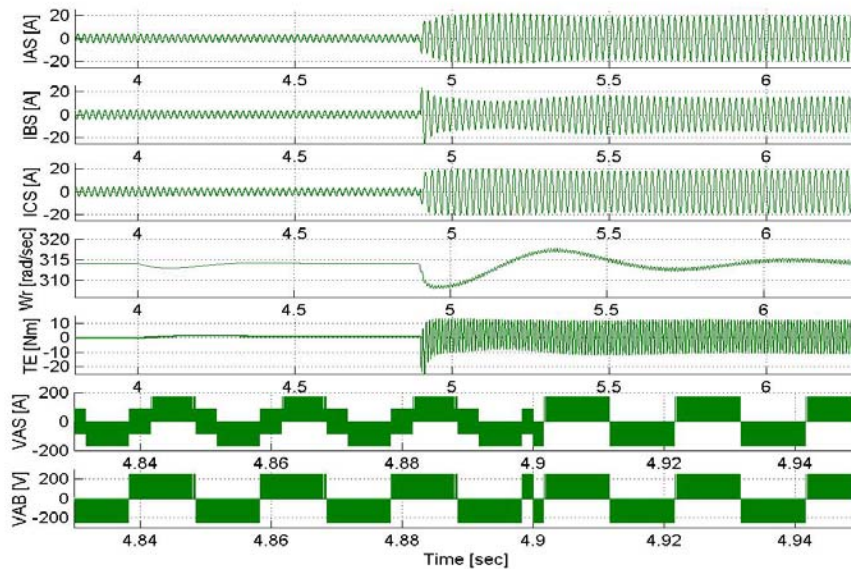


Figure 2. 26 Shows Star-connected IPMSM for shorted stator phase with PWM-VSI from top: phase 'a' current, phase 'b' current, phase 'c' current, rotor speed, torque, phase 'a' voltage, line voltage.

CHAPTER 3

INDUCTION MACHINE UNDER VARIOUS FAULTS

3.1 Introduction

This chapter presents the analysis of an Induction machine and the different unbalance situations that are involved. Similar analytical techniques used in Chapter 2 are also applied here. The star-connected stator and delta-connected stator induction machine's model equations are derived in stationary reference frame, since this is the best reference frame to imbalances and faults on electric machines [29]. For faults on the stator, the stator state variables are the qd currents and the states of the rotor circuit are the rotor flux linkages.

3.2 Voltage Equations

The voltage equations in machine variables may be expressed having referred all rotor variables to the stator windings by appropriate turns ratio [73].

$$V_{abcs} = r_s i_{abcs} + p \lambda_{abcs} \quad (3.1)$$

$$V'_{abcr} = r'_r i'_{abcr} + p \lambda'_{abcr} \quad (3.2)$$

where

$$\begin{bmatrix} \lambda_{abcs} \\ \lambda'_{abcr} \end{bmatrix} = \begin{bmatrix} L_s & L'_{sr} \\ (L'_{sr})^T & L'_r \end{bmatrix} \begin{bmatrix} i_{abcs} \\ i'_{abcr} \end{bmatrix} \quad (3.3)$$

$$p = d/dt \cdot \quad (3.4)$$

Transforming the variables associated with the symmetrical stator and rotor windings to the arbitrary reference frame using the following transformation for the stator and rotor, respectively:

$$f_{qdos} = K_s f_{abcs} \quad (3.5)$$

$$f'_{qdor} = K_r f'_{abcr} \quad (3.6)$$

$$\theta = \int \omega dt + \theta(0) \quad (3.7)$$

$$\theta_r = \int \omega_r dt + \theta_r(0) \quad (3.8)$$

$$\beta = \theta - \theta_r \quad (3.9)$$

where

$$K_s = \frac{2}{3} \begin{bmatrix} \cos \theta & \cos(\theta - 2\pi/3) & \cos(\theta + 2\pi/3) \\ \sin \theta & \sin(\theta - 2\pi/3) & \sin(\theta + 2\pi/3) \\ 1/2 & 1/2 & 1/2 \end{bmatrix}$$

$$K_r = \frac{2}{3} \begin{bmatrix} \cos \beta & \cos(\beta - 2\pi/3) & \cos(\beta + 2\pi/3) \\ \sin \beta & \sin(\beta - 2\pi/3) & \sin(\beta + 2\pi/3) \\ 1/2 & 1/2 & 1/2 \end{bmatrix}$$

f_{qdos}, f_{abcs} Stator circuit qdo and abc reference frame variables

f'_{qdor}, f'_{abcr} Referred rotor circuit qdo and abc reference frame variables

K_s Stator reference frame transformation

K_r Rotor reference frame transformation

θ Stator reference frame angular displacement (rad)

θ_r Rotor angular displacement (rad)

β	Rotor reference frame angular displacement (rad)
ω	Stator reference frame angular velocity (rad/sec)
ω_r	Rotor angular velocity (rad/sec)
i_{qs}, i_{ds}	Stator quadrature and direct axis currents (A)
i_{qr}, i_{dr}	Rotor quadrature and direct axis currents (A)
$\lambda_{qs}, \lambda_{ds}$	Stator quadrature and direct axis flux linkages (Wb)
$\lambda_{qr}, \lambda_{dr}$	Rotor quadrature and direct axis flux linkages (Wb)
L_{qs}, L_{ds}	Stator quadrature and direct axis inductances (H)
L_{qr}, L_{dr}	Rotor quadrature and direct axis inductances (H)
T_e	Electromagnetic Torque (Nm)
P	Number of poles
J	Inertia of the rotor
T_L	Torque (load).

The voltage equations in arbitrary reference frame are thus expressed below [74]:

$$V_{qdos} = r_s i_{qdos} + p \lambda_{qdos} + \omega \lambda_{dqs} \quad (3.10)$$

$$V'_{qdor} = r'_r i'_{qdor} + p \lambda'_{qdor} + (\omega - \omega_r) \lambda'_{dqr} \quad (3.11)$$

where

$$(\lambda_{dqs})^T = [\lambda_{ds} \quad -\lambda_{qs} \quad 0] \quad (3.12)$$

$$(\lambda'_{dqr})^T = [\lambda'_{dr} \quad -\lambda'_{qr} \quad 0] \quad (3.13)$$

$$\lambda_{qs} = L_{qs} i_{qs} + L_{mq} i'_{qr} = L_{ls} i_{qs} + L_{mq} (i_{qs} + i'_{qr}) \quad (3.14)$$

$$\lambda_{ds} = L_{ds} i_{ds} + L_{md} i'_{dr} = L_{ls} i_{ds} + L_{md} (i_{ds} + i'_{dr}) \quad (3.15)$$

$$\lambda'_{qr} = L'_{qr} i'_{qr} + L_{mq} i'_{qs} = L'_{lr} i'_{qr} + L_{mq} (i'_{qs} + i'_{qr}) \quad (3.16)$$

$$\lambda'_{dr} = L'_{dr} i'_{dr} + L_{md} i'_{ds} = L'_{lr} i'_{dr} + L_{mq} (i'_{ds} + i'_{dr}) \quad (3.17)$$

$$\lambda_{os} = L_s i_{os} \quad (3.18)$$

$$\lambda'_{or} = L'_{lr} i'_{or} \quad (3.19)$$

In stationary reference frame, the machine equations can be expressed as follows:

$$V'_{qdos} = r_s i'_{qdos} + p \lambda'_{qdos} = r_s I_{qds} + p [L_s I_{qds} + L_m I_{qdr}] \quad (3.20)$$

$$V'_{qdor} = r'_r i'_{qdor} + p \lambda'_{qdor} + (-\omega_r) \lambda'_{dqr} = r_r I_{qdr} - \omega_r \lambda'_{dqr} + p [L_r I_{qdr} + L_m I_{qds}] = 0 \quad (3.21)$$

From Equations (3.16) and (3.17), it can be shown that

$$I_{qdr} = \frac{\lambda_{qdr} - L_m I_{qds}}{L_r}, \quad p I_{qdr} = \frac{p \lambda_{qdr}}{L_r} - \frac{L_m}{L_r} p I_{qds} \quad (3.22)$$

Hence, simplifying Equation (3.20) with $p I_{qdr}$ replaced with the above expressions, the state equations can be expressed in terms of the stator current:

$$p I_{qs} = \frac{1}{\Delta} \left[L'_r V_{qs} - r_s I_{qs} L_r + \frac{L_m}{L_r} r_r \lambda_{qr} - \frac{L_m^2}{L_r} r_r I_{qs} - L_m \omega_r \lambda_{dr} \right] \quad (3.23)$$

$$p I_{ds} = \frac{1}{\Delta} \left[L'_r V_{ds} - r_s I_{ds} L_r + \frac{L_m}{L_r} r_r \lambda_{dr} - \frac{L_m^2}{L_r} r_r I_{ds} + L_m \omega_r \lambda_{qr} \right] \quad (3.24)$$

where

$$\Delta = L_r L_s - L_m^2 \quad (3.25)$$

Note: $L_{mq} = L_{md} = L_m$

while the rotor state equations can be expressed in terms of flux as given below:

$$p\lambda_{qr} = -r_r \left[\frac{\lambda'_{qr} - L_m I_{qs}}{L_r} \right] + \omega_r \lambda_{dr} \quad (3.26)$$

$$p\lambda_r = -r_r \left[\frac{\lambda_{dr} - L_m I_{ds}}{L_r} \right] - \omega_r \lambda_{qr} \quad (3.27)$$

The torque equation is given as

$$T_e = \frac{3P}{4} (\lambda_{ds} i_{qs} - \lambda_{qs} i_{ds}) \quad (3.28)$$

The torque and the rotor speed are related by

$$T_e = J \left(\frac{2}{P} \right) p\omega_r + T_L \quad (3.29)$$

The waveforms from computer simulations using Matlab/SIMULINK from the qd voltage equations and the torque equations derived are shown in Figures 3.1-3.2 for a three-phase induction motor with star-connected stator winding with 220V (rms) at 60Hz; and Figures 3.3- 3.4 for PWM-VSI supply with 280V- V_{dc} at 60Hz, with a load of 10Nm applied at steady state. The analysis of the steady state, transient and dynamic characteristics of these drive systems has been evaluated in the past [73-76]. Table 3.1 shows the parameters of the Induction machine used in these simulations.

As will be expected in an induction motor, the speed drops when a load is applied at steady state.

Computer simulations using the derived model equations for both star-connected stator and delta-connected stator type are used to show the induction machine performance/response under different fault situations. Generally, during fault situations the machine oscillates as will be seen in the torque of the motor and the rotor speed.

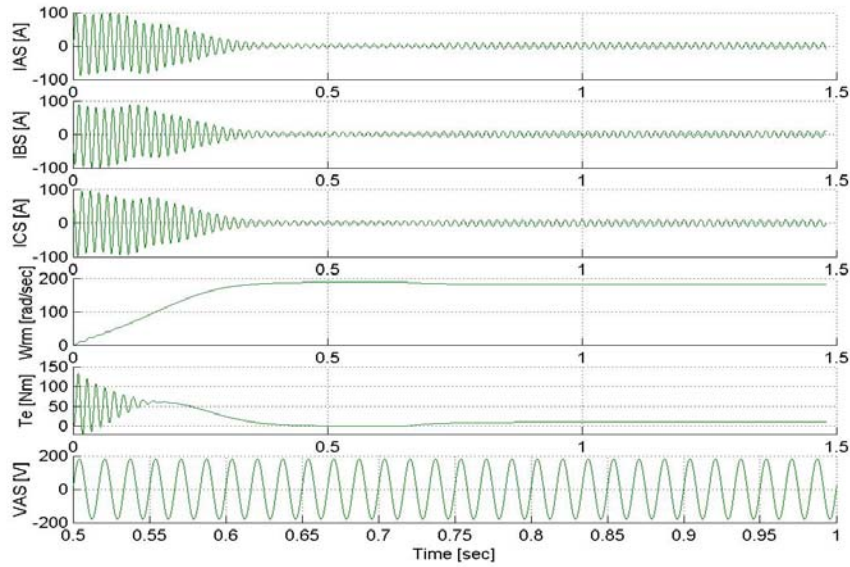


Figure 3.1 Shows starting transient of a star connected Induction machine with 220V(rms) three-phase supply with load from top: phase currents ‘a’, ‘b’, ‘c’, mechanical speed, torque, phase voltage.

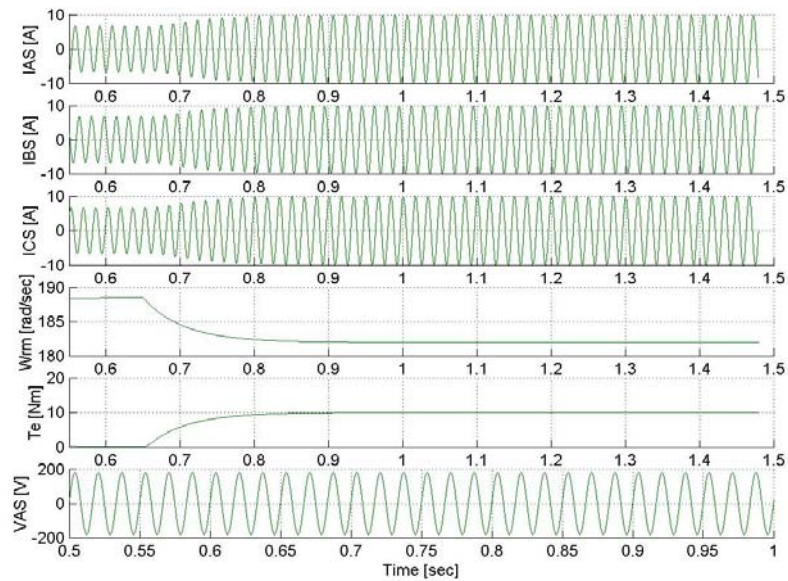


Figure 3.2 Shows the steady state characteristics of a star connected Induction machine with 220V(rms) three-phase supply with load from top: phase currents ‘a’, ‘b’, ‘c’, mechanical speed, torque, phase voltage.

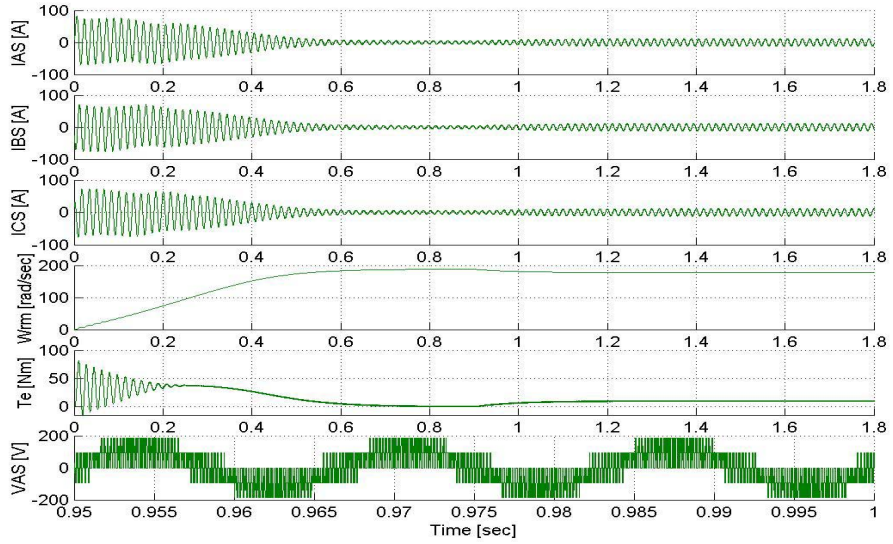


Figure 3.3 Shows a star-connected Induction machine with PWM-VSI supply with 280V V_{dc} with load from top: phase currents 'a', 'b', 'c', mechanical speed, torque, phase voltage.

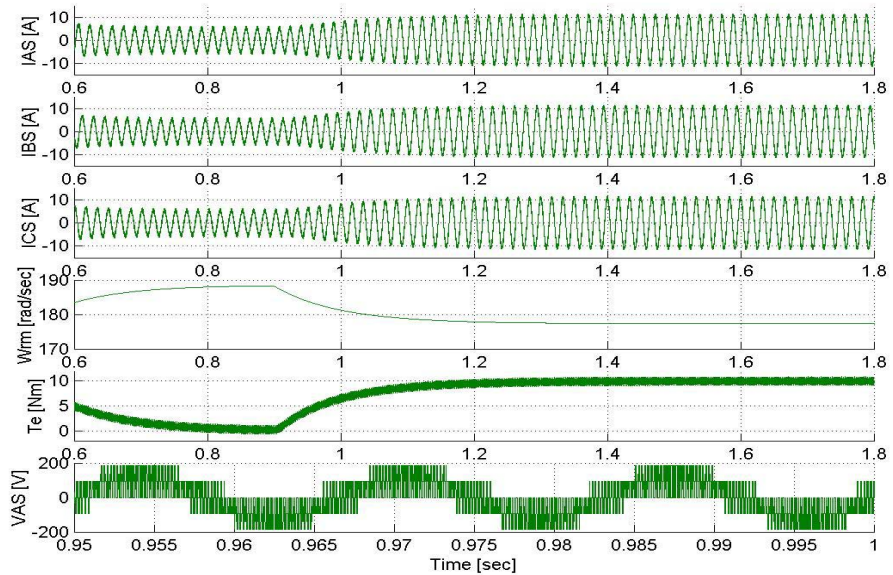


Figure 3.4 Shows the steady state characteristics of a star-connected Induction machine with PWM-VSI supply with 280V V_{dc} with load from top: phase currents 'a', 'b', 'c', mechanical speed, torque, phase voltage.

Table 3. 1 Induction Machine Parameters

Rated Line Voltage	220 V
Stator Resistance, R_s	0.435 ohms
Stator Leakage Inductance, L_{ls}	2 mH
Rotor Resistance, R_r	0.816 ohms
Rotor Leakage Inductance, L_{lr}	2 mH
Mutual Inductance, L_{ms}	0.0693 H
No. of Poles, P	4
Synchronous Speed, W_e	377 rad/sec
Inertia, J	0.04 kg/m ²

3.3 Unbalances in Star-Connected Induction Machine

3.3.1 Supply Line “A” Open-Circuit Response

Figure 3.5 shows a star-connected induction machine with the supply line ‘a’ opened.

The fault analysis is done in stationary reference frame.

With supply line ‘a’ open,

$$I_{as} = 0 \quad (3.30)$$

Note: The Kirchhoff current law applies hence,

$$I_{as} + I_{bs} + I_{cs} = 0 \quad (3.31)$$

$$I_{bs} = -I_{cs} \quad (3.32)$$

Hence, in stationary reference frame:

$$I_{qs} = -1/3[I_{bs} + I_{cs}] \quad (3.33)$$

$$I_{os} = 1/3[I_b + I_c] \Rightarrow I_o = -I_{qs} \quad (3.34)$$

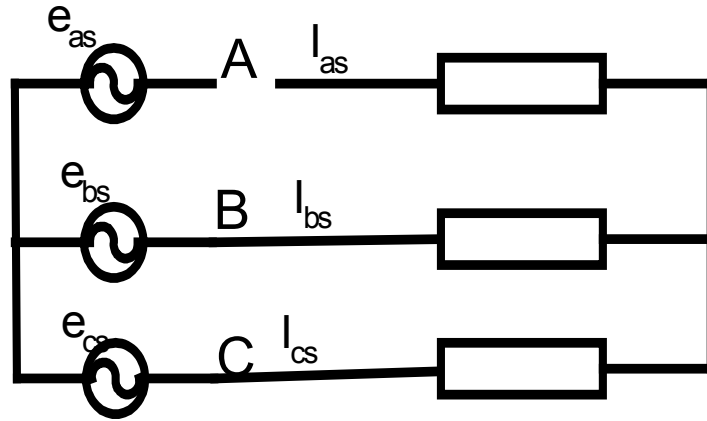


Figure 3. 5 Shows star-connected stator Induction machine with supply line ‘a’ open.

$$I_{os} = \frac{1}{3}[I_a + I_b + I_c] = 0 \Rightarrow I_{qs} = 0 \quad (3.35)$$

$$I_{ds} = \frac{1}{\sqrt{3}}[I_{cs} - I_{bs}] \quad (3.36)$$

while the ds -voltage in stationary reference frame can be expressed as

$$V_{ds} = \frac{1}{\sqrt{3}}[V_{cn} - V_{bn}] = \frac{1}{\sqrt{3}}[e_{cg} - e_{bg}]. \quad (3.37)$$

From the above, it has been shown that $I_{qs} = 0$ and V_{ds} is known from (3.37). These are sufficient conditions to simulate the fault. Substituting Equation (3.35) in Equation (3.20) which is rewritten below,

$$\begin{aligned} V_{qs} &= r_s I_{qs} + p \lambda_{qs} \\ &= r_s I_{qs} + p[L_{qs} I_{qs} + L_{mq} I_{qr}] \\ &= L_{mq} p I_{qr} . \end{aligned} \quad (3.38)$$

Therefore, from Equation (3.22)

$$pI_{qr} = \frac{p\lambda_{qr}}{L_r} . \quad (3.39)$$

Substitute (3.39) in (3.38),

$$V_{qs} = \frac{L_m}{L_{qr}} p\lambda_{qr} . \quad (3.40)$$

With V_{qs} , V_{ds} , and pI_{qs} (I_{qs}) known, pI_{ds} can be solved from (3.24).

The torque equation thus reduces to

$$\begin{aligned} T_e &= \frac{3P}{4} [\lambda_{ds} I_{qs} - \lambda_{qs} I_{ds}] \\ &= \frac{3P}{4} [-\lambda_{qs} I_{ds}] \\ &= \frac{3P}{4} \frac{L_{mq}}{L_{qr}} [-\lambda_{qr} I_{ds}] . \end{aligned} \quad (3.41)$$

Computer simulation results of the motor are shown in the Figures 3.6 and 3.7 with a load applied in steady state before the supply line is opened.

The machine was able to tolerate the fault during this unbalance as shown by the simulation result, the machine speed drops to some low value. The current in phase ‘a’ becomes zero as earlier derived.

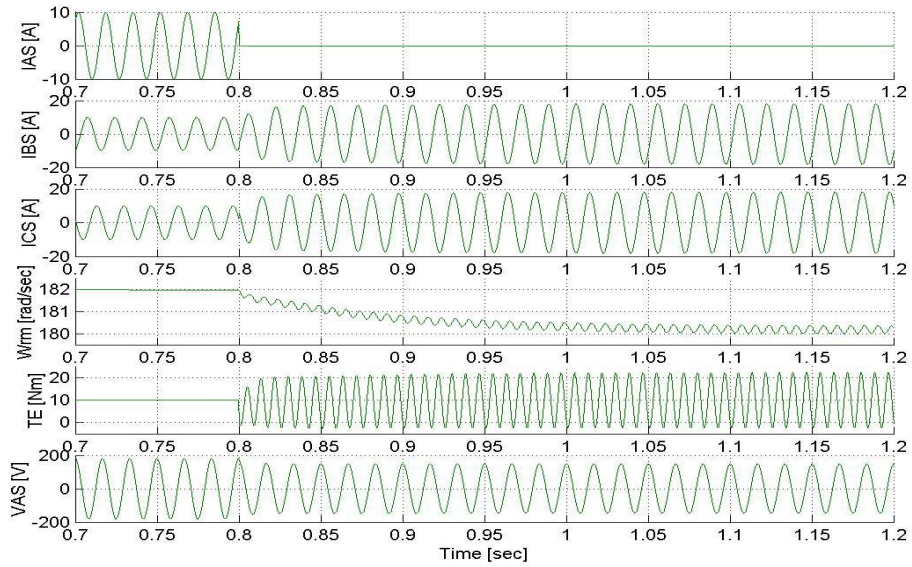


Figure 3.6 Shows a star-connected Induction machine with supply line ‘a’ open-circuited with 220V(rms) three-phase supply with load, from top: phase currents ‘a’, ‘b’, ‘c’, mechanical speed, torque, phase voltage.

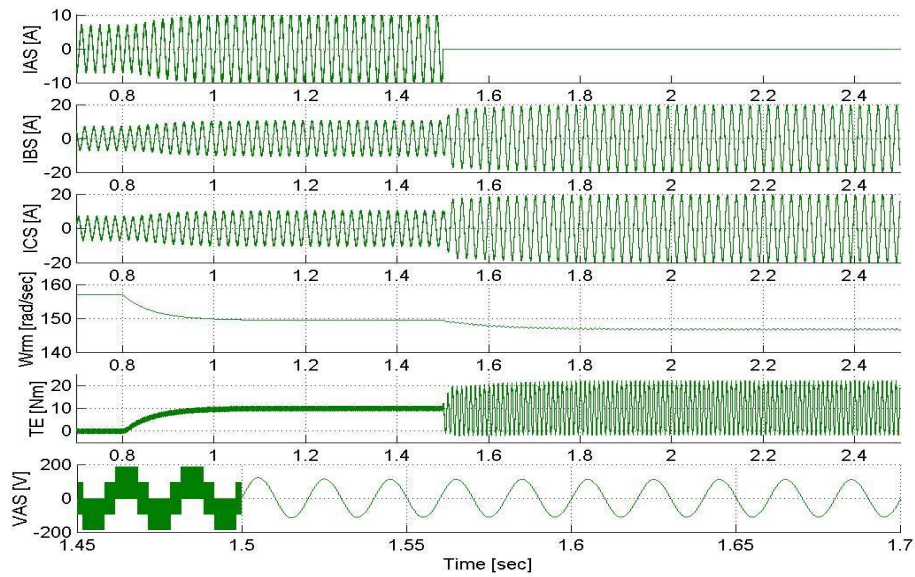


Figure 3.7 Shows a star-connected Induction machine with supply line ‘a’ open-circuited with PWM-VSI supply with load, from top: phase currents ‘a’, ‘b’, ‘c’, mechanical speed, torque, phase voltage.

3.3.2 Stator Line to Line Fault

An unbalance in a star-connected induction machine with the stator phase ‘b’ and ‘c’ shorted is shown in Figure 3.8, this can also be referred to as line-to-line fault.

The following analysis are valid for this unbalance condition:

$$e_{ag} = V_{as} + V_{sn} \quad (3.42)$$

$$V_{bs} = V_{cs} \quad (3.43)$$

$$I_a + I_b + I_c = 0 \quad (3.44)$$

$$I_c = -I_b = I_x \quad (3.45)$$

$$I_a = 0 \quad (3.46)$$

Hence, the currents in *qs-ds* stationary reference frame are given as

$$I_{qs} = \frac{2}{3} I_{as} - \frac{1}{3} I_{bs} - \frac{1}{3} I_{cs} = 0 \quad (3.47)$$

$$I_{ds} = \frac{1}{\sqrt{3}} [I_{cs} - I_{bs}] = \frac{2I_{cs}}{\sqrt{3}} \quad (3.48)$$

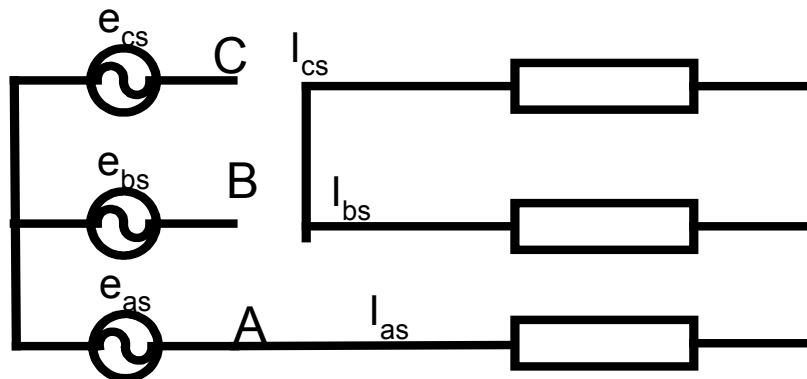


Figure 3. 8 Shows star-connected stator Induction machine with 2 stator phases shorted.

And the voltages as

$$V_{ds} = \frac{1}{\sqrt{3}} [V_{cs} - V_{bs}] = 0 \quad (3.49)$$

$$V_{qs} = \frac{2}{3}V_{as} - \frac{1}{3}V_{bs} - \frac{1}{3}V_{cs} = \frac{2}{3}V_{as} - \frac{2}{3}V_{bs} \quad (3.50)$$

Substituting Equation (3.47) in Equation (3.20), it can be shown that

$$V_{qs} = L_m p I_{qr} \quad (3.51)$$

With V_{qs} , V_{ds} , and pI_{qs} (I_{qs}) known, pI_{ds} can be solved from (3.24).

Computer simulation results are shown in Figures 3.9-3.10 with and without load, respectively, for 220V (rms) supply, Figure 3.11 shows the performance of the machine when a PWM-VSI is used as the supply voltage. The performance of this machine is dependent on the load applied on it when the fault occurs.

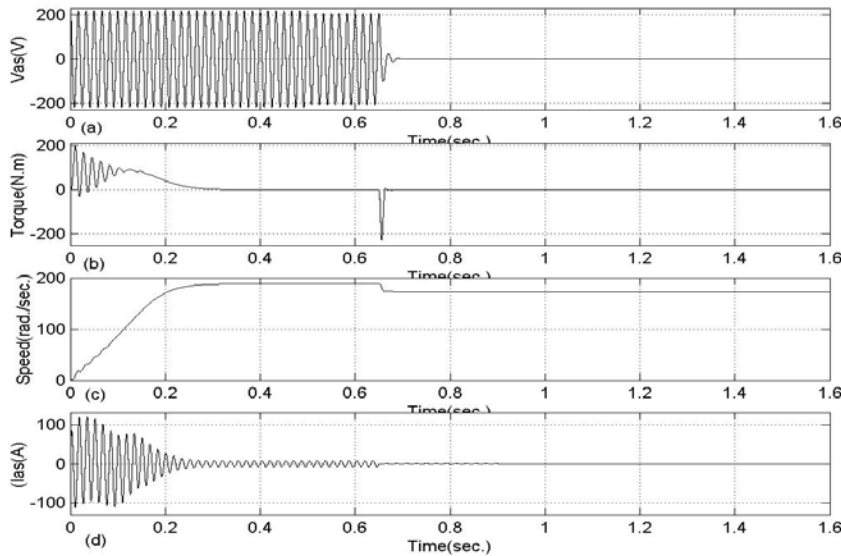


Figure 3.9 Shows from top: Phase voltage Torque Speed Phase current without Load applied

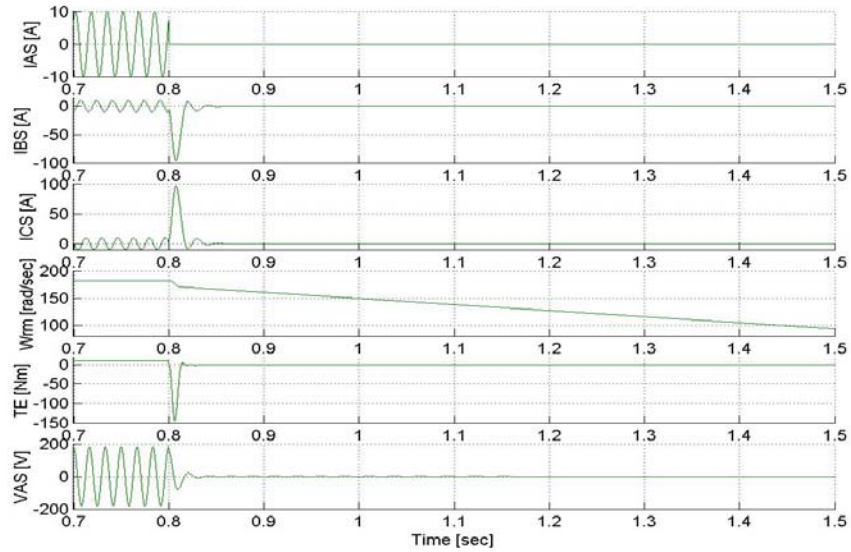


Figure 3.10 Shows a star-connected Induction machine with 2 stators winding shorted with 220V(rms) three-phase supply with load, from top: phase currents ‘a’, ‘b’, ‘c’, mechanical speed, torque, phase voltage.

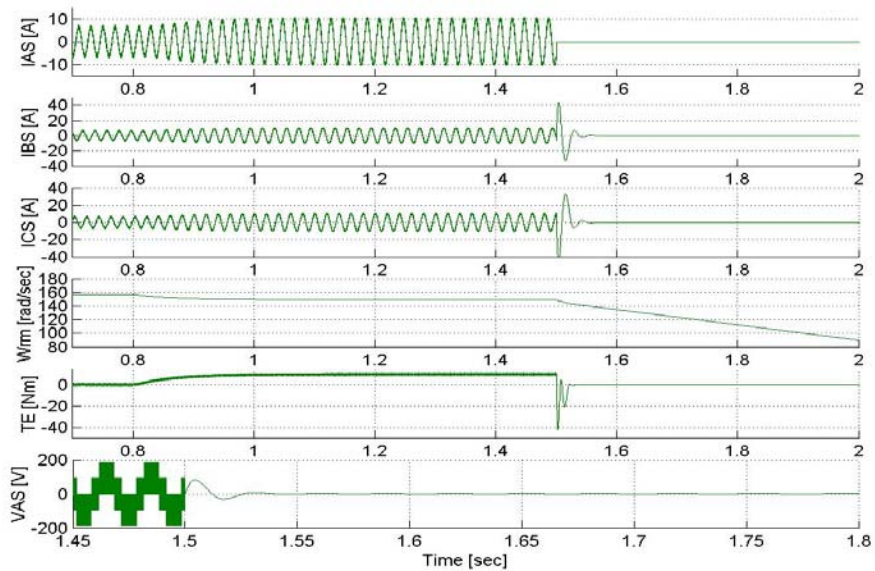


Figure 3. 11 Shows a star-connected Induction machine with 2 stators winding shorted with PWM-VSI supply with load, from top: phase currents ‘a’, ‘b’, ‘c’, mechanical speed, torque, phase voltage.

3.3.3 Stator Line “B” and “C” Shorted to Supply Line Voltage “C”

The schematic for an unbalance with the stator phase ‘b’ and ‘c’ shorted is described in Figure 3.12. The performance of this motor under this fault situation is analyzed and the results from computer simulation are shown in Figures 3.13 and 3.14.

From this fault situation, it can be shown that

$$e_{ag} = V_{as} + V_{sn} \quad (3.52)$$

$$e_{cg} = V_{bs} + V_{sn} \quad (3.53)$$

$$V_{bs} = V_{cs} \quad (3.54)$$

$$e_{cg} = V_{cs} + V_{sn} \quad (3.55)$$

Hence, in stationary reference frame, the voltage are given as

$$V_{qs} = \frac{2}{3}V_{as} - \frac{1}{3}V_{bs} - \frac{1}{3}V_{cs}$$

$$V_{qs} = \frac{2}{3}V_{as} - \frac{2}{3}V_{cs} = \frac{2}{3}[e_{ag} - e_{cg}] \quad (3.56)$$

$$V_{ds} = \frac{1}{\sqrt{3}}[V_{cs} - V_{bs}] = 0 \quad (3.57)$$

With the voltages known, these are substituted in Equations (3.23) and (3.24); this is sufficient to simulate this fault.

Figure 3.13 shows the simulation result of the fault with three-phase supply of 220V (rms) supply while Figure 3.14 shows the simulation result when a PWM-VSI is used as the supply source, the fault occur after a load of 10Nm was applied to the motor.

The simulation shows that the currents magnitude increases and the speed drops making the machine goes into a generating mode.

3.4 Delta Connected Stator

The delta-connected stator induction machine is as shown in Figure 3.15 and the phase voltages can be expressed as follows:

$$V_{an} = V_{ab} = V_{ag} - V_{bg} \quad (3.58)$$

$$V_{bn} = V_{bc} = V_{bg} - V_{cg} \quad (3.59)$$

$$V_{cn} = V_{ca} = V_{cg} - V_{ag} \quad (3.60)$$

The q-axis and d-axis voltage equations at stationary reference frame and the electromagnetic torque expression given by Equations (3.20)-(3.29) still applies in the analysis of this motor. Figures 3.16-3.19 shows the characteristics of the induction machine under normal situation using a 73.4V (rms) three-phase supply and PWM-VSI supply of 208V V_{dc} with a load of 10Nm applied in steady state.

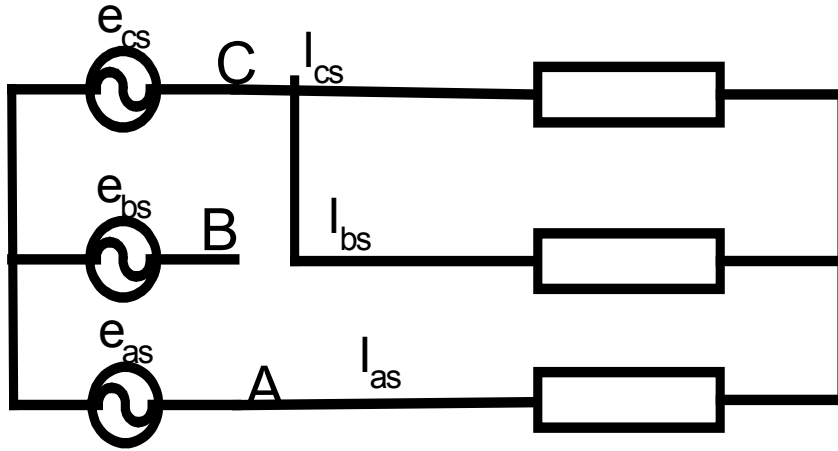


Figure 3. 12 Shows star-connected stator Induction machine with a phase open-circuited and 2 shorted stator phases.

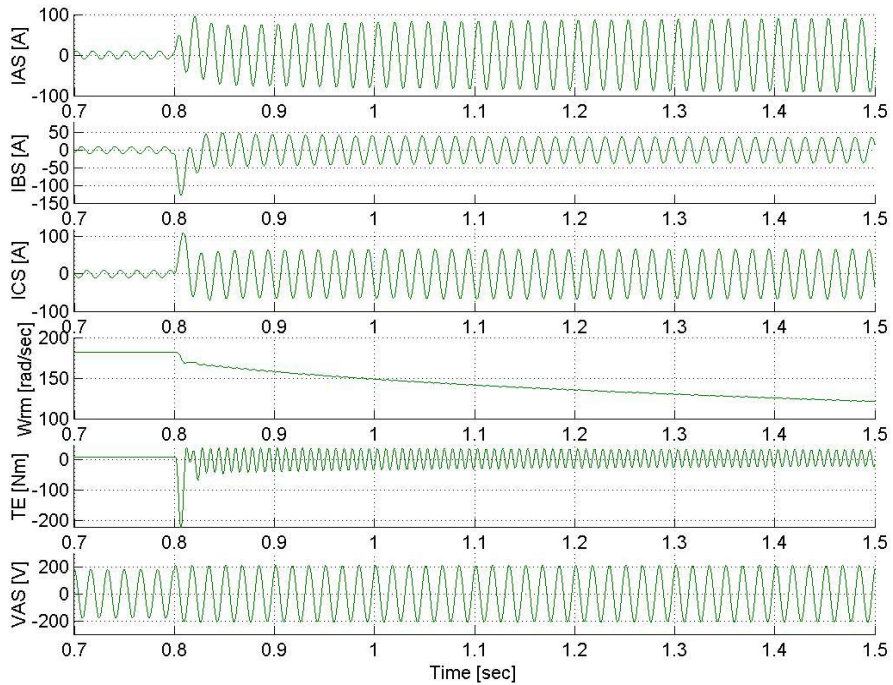


Figure 3. 13 Shows a star-connected Induction machine with 2 stators winding shorted while a phase is open-circuited, with 220V(rms) three-phase supply with load, from top: phase currents 'a', 'b', 'c', mechanical speed, torque, phase voltage.

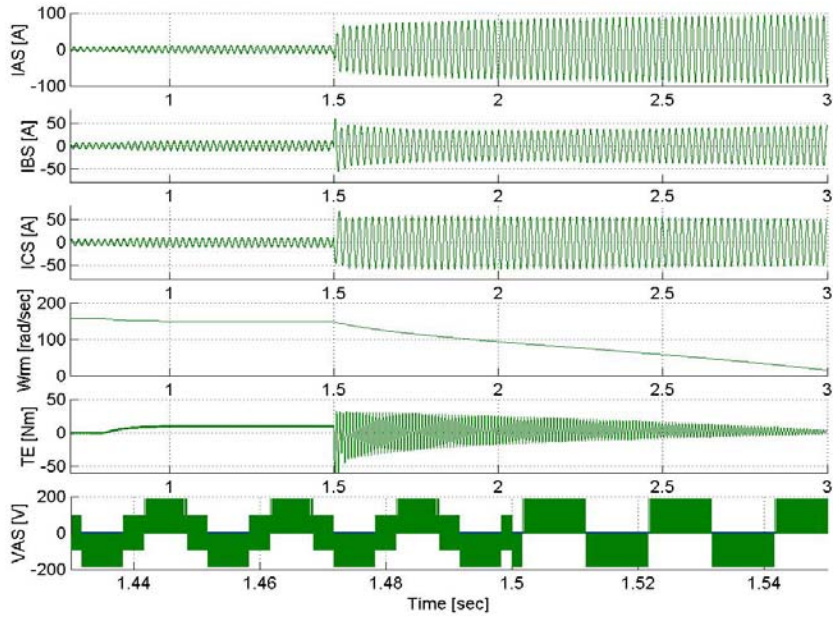


Figure 3. 14 Shows a star-connected Induction machine with 2 stators winding shorted while a phase is open-circuited, with PWM-VSI supply with load, from top: phase currents ‘a’, ‘b’, ‘c’, mechanical speed, torque, phase voltage.

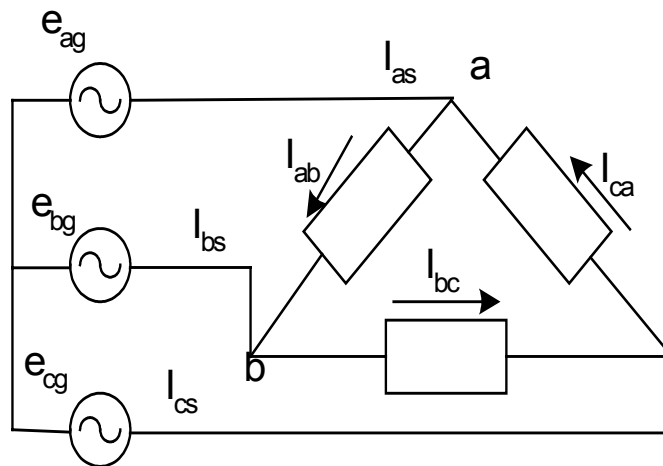


Figure 3. 15 Shows an Induction machine with delta-connected stator.

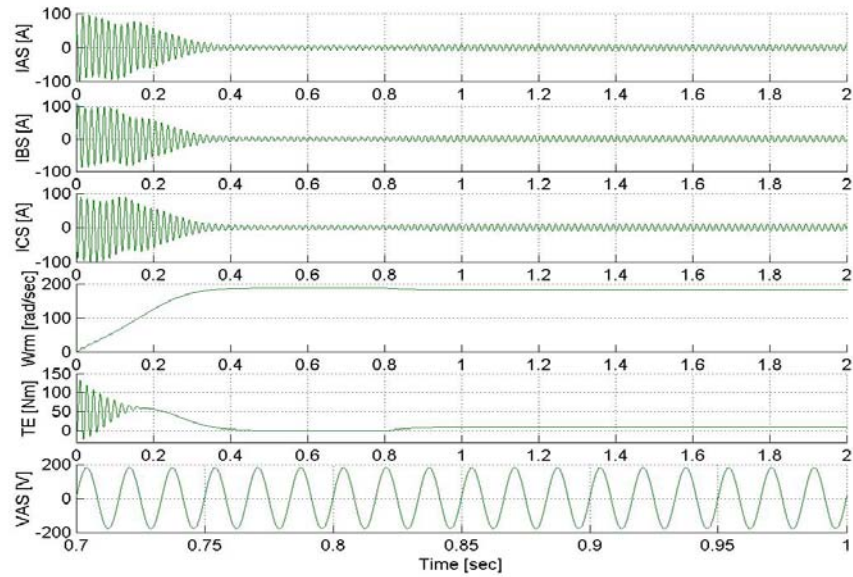


Figure 3. 16 Shows delta-connected Induction machine with 104V three-phase supply with load from top: phase currents ‘a’, ‘b’, ‘c’, mechanical speed, torque, phase voltage.

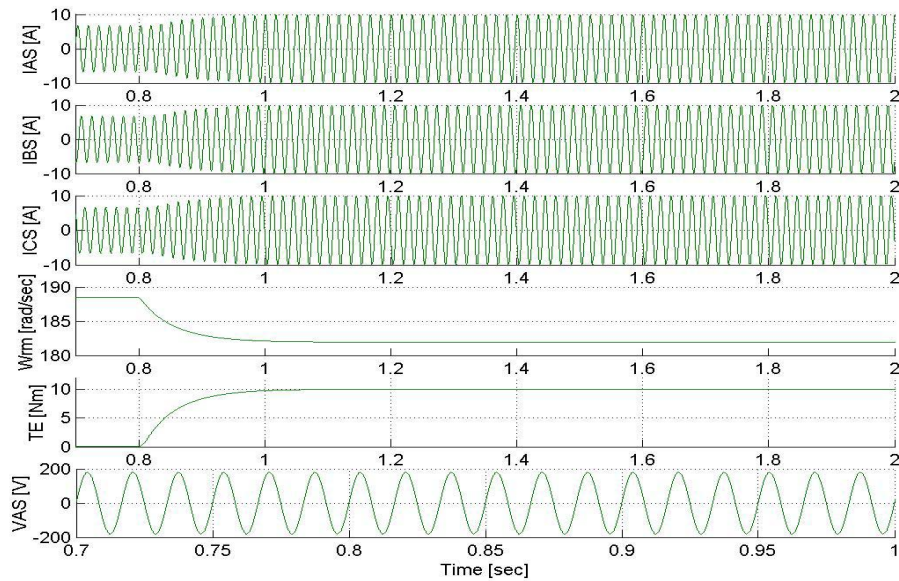


Figure 3. 17 Shows the steady state characteristics of an Induction machine with 104V three-phase supply with load from top: phase currents ‘a’, ‘b’, ‘c’, mechanical speed, torque, phase voltage.

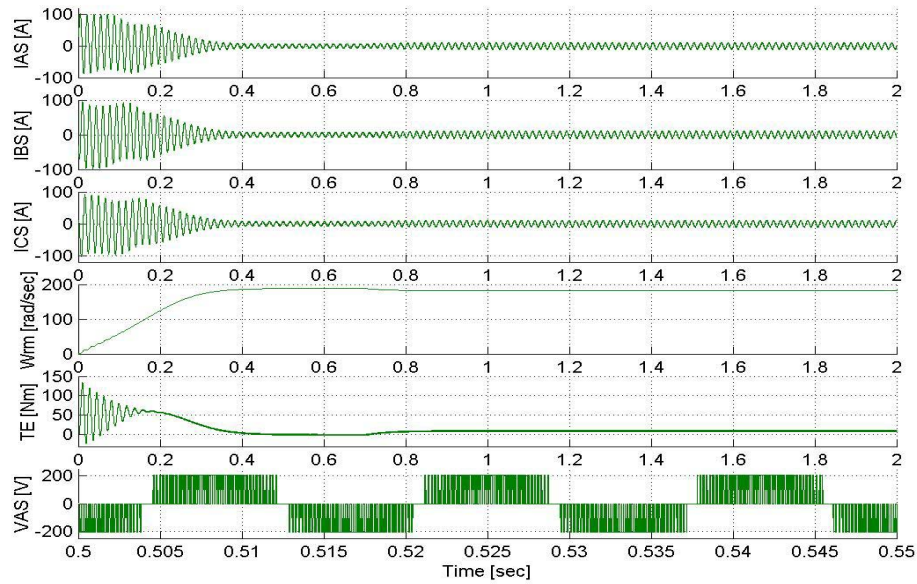


Figure 3. 18 Shows Induction machine with PWM-VSI supply with 208V V_{dc} with load from top: phase currents ‘a’, ‘b’, ‘c’, mechanical speed, torque, phase voltage.

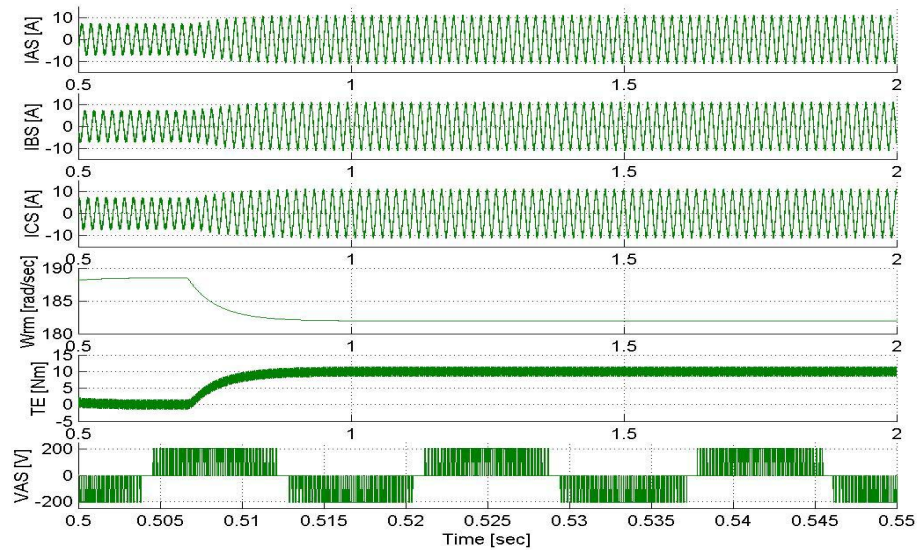


Figure 3. 19 Shows the steady state characteristics of an Induction machine with PWM-VSI supply with 208V V_{dc} with load from top: phase currents ‘a’, ‘b’, ‘c’, mechanical speed, torque, phase voltage.

3.5 Unbalances in Delta-Connected Induction Machine

3.5.1 Supply Line ‘A’ Open-Circuit Response

Figure 3.20 shows the schematic for an unbalance condition in which the supply line ‘A’ is open. Therefore, it can be shown for this unbalance condition that

$$V_{bc} = V_b = e_{bg} - e_{cg} \quad (3.61)$$

$$I_c = I_a \quad (3.62)$$

Note:

$$V_a + V_b + V_c = 0 \Rightarrow V_{os} = 0 \quad (3.63)$$

The voltages can be shown below in qs - ds stationary reference frame as

$$V_{qs} = \frac{2}{3}V_a - \frac{1}{3}V_b - \frac{1}{3}V_c = V_a \quad (3.64)$$

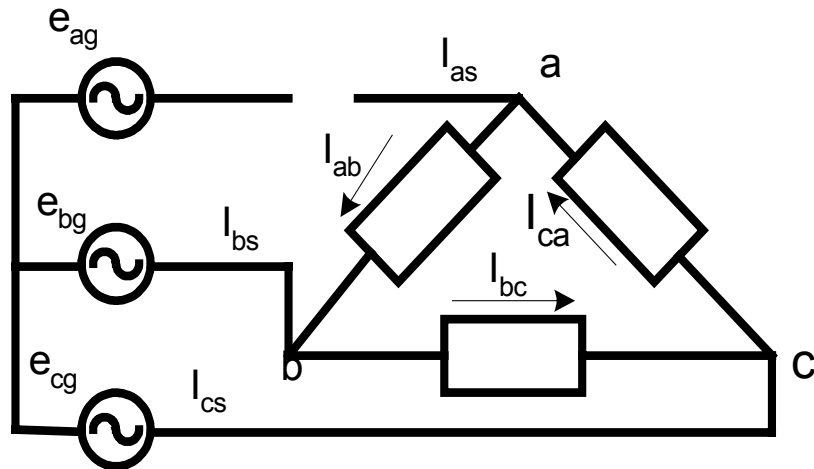


Figure 3. 20 Shows a delta-connected Induction machine with supply line ‘a’ open-circuited.

$$V_{ds} = \frac{1}{\sqrt{3}}[V_c - V_b] = \frac{1}{\sqrt{3}}[-V_a - 2V_b] = \frac{1}{\sqrt{3}}[-V_{qs} - 2V_b] \quad (3.65)$$

and the current can be expressed as

$$I_{qs} = \frac{2}{3}I_a - \frac{1}{3}I_b - \frac{1}{3}I_c = \frac{I_a - I_b}{3} \quad (3.66)$$

$$I_{ds} = \frac{1}{\sqrt{3}}[I_c - I_b] = \frac{1}{\sqrt{3}}[I_a - I_b] \quad (3.67)$$

$$I_{ds} = \sqrt{3}I_{qs} \quad (3.68)$$

$$I_o = \frac{1}{3}[I_a + I_b + I_c] = \frac{1}{3}[2I_a + I_b] . \quad (3.69)$$

From Equation (3.22) (which is repeated below),

$$I_{qdr} = \frac{\lambda_{qdr} - L_m I_{qds}}{L_r}$$

$$L_m pI_{qdr} = \frac{L_m}{L_r} [p\lambda_{qdr}] - \frac{L_m^2}{L_r} pI_{qds} . \quad (3.70)$$

From (3.70),

$$L_m pI_{qr} = \frac{L_m}{L_r} p\lambda_{qr} - \frac{L_m^2}{L_r} pI_{qs} \quad (3.71)$$

$$\sqrt{3}L_m pI_{dr} = \sqrt{3} \frac{L_m}{L_r} p\lambda_{dr} - \sqrt{3} \frac{L_m^2}{L_r} pI_{ds} . \quad (3.72)$$

Substituting (3.68) in (3.72) gives

$$\sqrt{3}L_m pI_{dr} = \sqrt{3} \frac{L_m}{L_r} p\lambda_{dr} - 3 \frac{L_m^2}{L_r} pI_{qs} . \quad (3.73)$$

By substituting Equation (3.20) in (3.65), and replacing pI_{qr} and pI_{dr} as given in (3.71)

and (3.73), respectively, it can be shown that

$$4r_s I_{qs} + 4L_s p I_{qs} + \sqrt{3} \frac{L_m}{L_r} p \lambda_{dr} - 4 \frac{L_m^2}{L_r} p I_{qs} + 2V_b + \frac{L_m}{L_r} p \lambda_{qr} = 0 . \quad (3.74)$$

From Equation (3.74), the currents are known and hence the subsequent voltages during fault can be calculated. Also, $V_{os} = 0 \Rightarrow I_{os} = 0$.

Figures 3.21 and 3.22 show the waveforms from the computer simulation for this fault situation. The machine shows little decrease in the speed during while the faults persists indicating an high fault tolerance. Phase ‘b’ stator current shows an increase in magnitude.

3.5.2 Stator Phase “A” Open-Circuit Response

Figure 3.23 shows the schematic of an unbalance in which the stator phase of the delta-connected induction machine is opened.

The machine is analyzed and it can be shown that the following equations apply:

$$I_a = 0 \quad (3.75)$$

$$V_b = e_b - e_c \quad (3.76)$$

$$V_c = e_c - e_a \quad (3.77)$$

$$e_b - e_a = V_b + V_c . \quad (3.78)$$

The qs and ds voltages are given as

$$\begin{aligned} V_{qs} &= \frac{2}{3} V_a - \frac{1}{3} V_b - \frac{1}{3} V_c = \frac{2}{3} V_a - \frac{(V_b + V_c)}{3} \\ &= \frac{2}{3} V_a - \frac{1}{3} [e_b - e_a] \end{aligned} \quad (3.79)$$

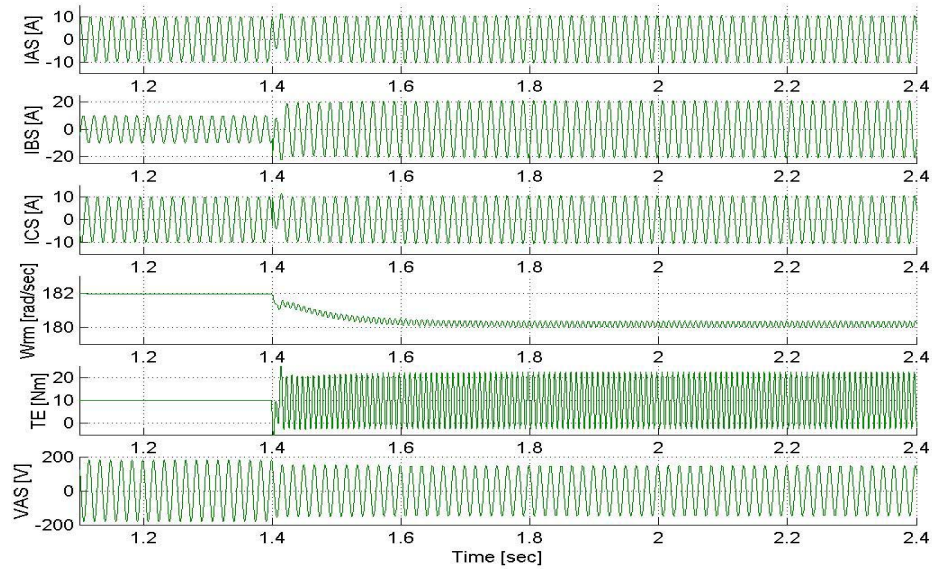


Figure 3.21 Shows a delta-connected Induction machine with supply line ‘a’ open-circuited with 104V three-phase supply with load, from top: phase currents ‘a’, ‘b’, ‘c’, mechanical speed, torque, phase voltage.

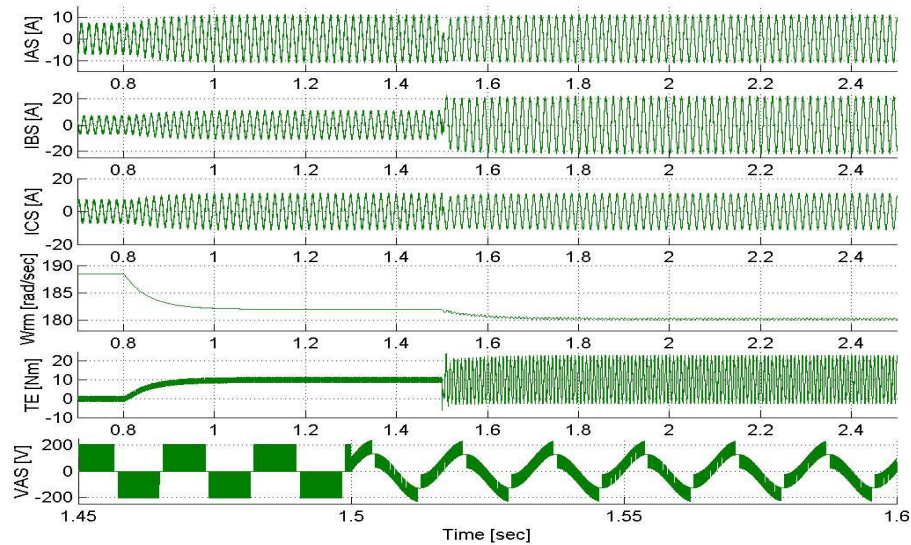


Figure 3. 22 Shows a delta-connected Induction machine with supply line ‘a’ open-circuited with PWM-VSI supply with load, from top: phase currents ‘a’, ‘b’, ‘c’, mechanical speed, torque, phase voltage.

$$V_{ds} = \frac{1}{\sqrt{3}}[V_c - V_b] . \quad (3.80)$$

Also, the currents are given as

$$I_o = -I_{qs} \quad (3.81)$$

$$I_a = I_{qs} - I_{qs} = 0 \quad (3.82)$$

$$I_b = -\frac{1}{2}I_{qs} - \frac{\sqrt{3}}{2}I_{ds} - I_{qs} = -\frac{3}{2}I_{qs} - \frac{\sqrt{3}}{2}I_{ds} \quad (3.83)$$

$$I_c = -\frac{1}{2}I_{qs} + \frac{\sqrt{3}}{2}I_{ds} - I_{qs} = -\frac{3}{2}I_{qs} + \frac{\sqrt{3}}{2}I_{ds} . \quad (3.84)$$

It can be shown that

$$V_{qs} = 2V_{os} + e_a - e_b \quad (3.85)$$

$$V_{qs} = e_a - e_b - 2r_s I_{qs} - 2L_{ls} pI_{qs} . \quad (3.86)$$

By substituting Equation (3.23) in Equation (3.86), V_{qs} can be determined, while V_{ds} is known from (3.80), then this fault can be simulated.

Figures 3.24-3.25 shows a little or no change in the speed of machine during fault except for the oscillations. The current in phase 'a' is zero as derived while the current in the other phases increased.

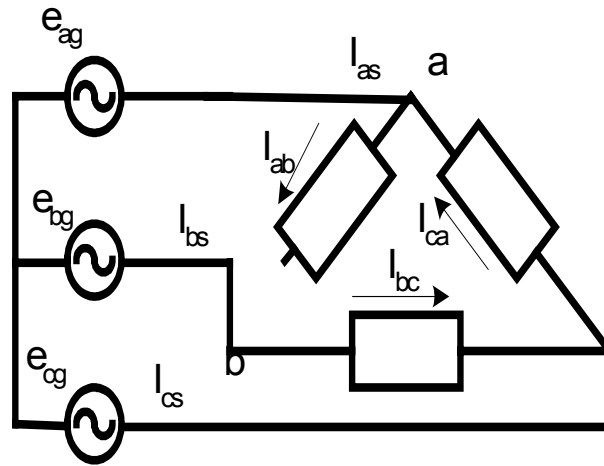


Figure 3. 23 Shows a delta-connected Induction machine with phase ‘a’ open-circuited.

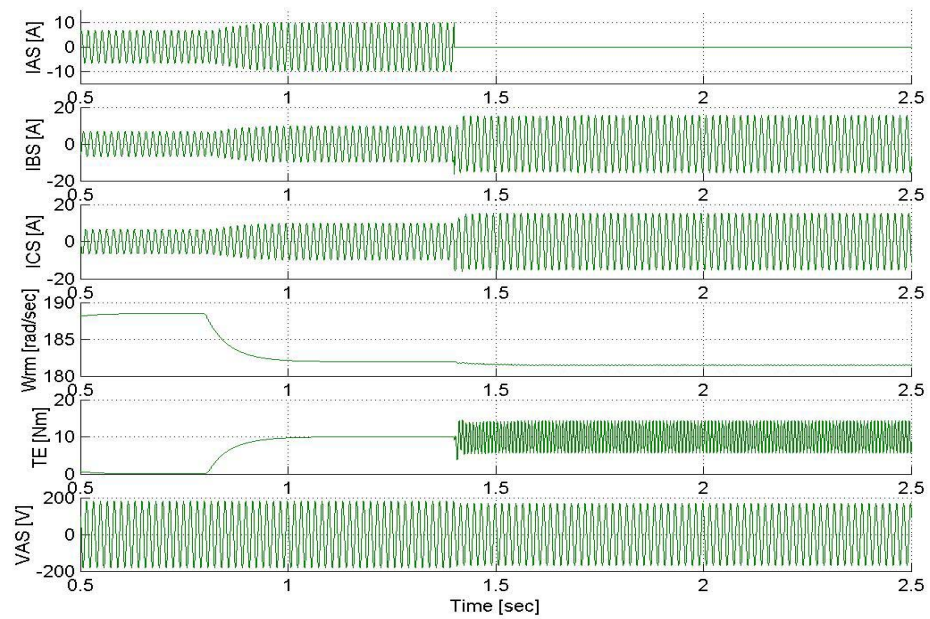


Figure 3.24 Shows a delta-connected Induction machine with phase ‘a’ open-circuited with 104V three-phase supply with load applied, from top: phase currents ‘a’, ‘b’, ‘c’, mechanical speed, torque, phase voltage.

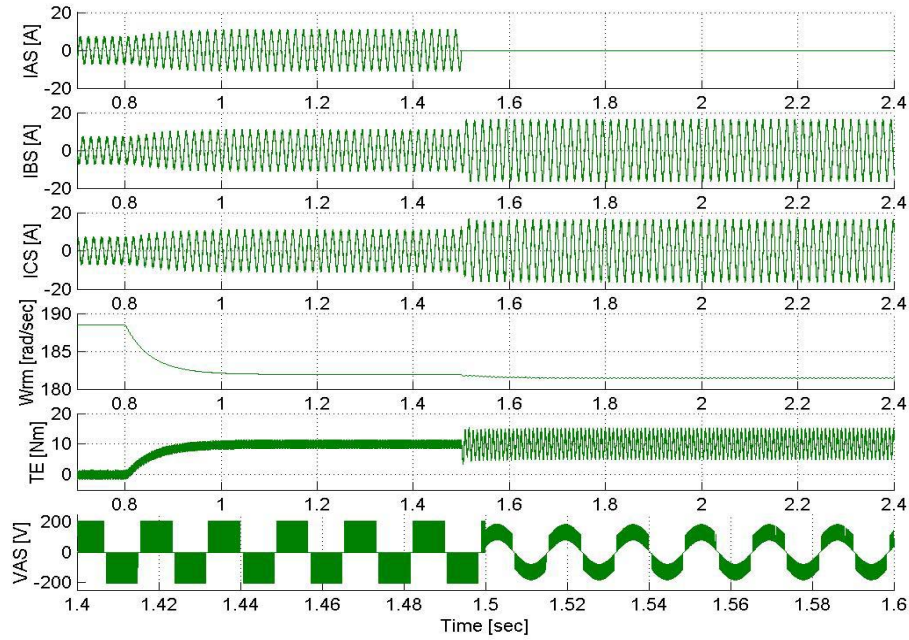


Figure 3.25 Shows a delta-connected Induction machine with phase ‘a’ open-circuited with PWM-VSI supply with load applied, from top: phase currents ‘a’, ‘b’, ‘c’, mechanical speed, torque, phase voltage.

3.5.3 Supply Line “B” Open and Stator Phase “A” Shorted

Figure 3.26 shows the schematic for the unbalance in which the stator phase ‘a’ of a delta-connected induction motor is shorted.

From this fault, it can be shown from Figure 3.26 that

$$V_{ab} = 0 \quad (3.87)$$

$$V_{bc} = e_{ag} - e_{cg} \quad (3.88)$$

$$V_{ca} = e_{cg} - e_{ag} \quad (3.89)$$

Hence, the qs and ds voltages in stationary reference frame are given as

$$V_{qs} = 0 \quad (3.90)$$

$$V_{ds} = \frac{2}{\sqrt{3}} [e_c - e_a] \quad (3.91)$$

$$V_{os} = 0 \Rightarrow I_{os} = 0. \quad (3.92)$$

With V_{qs} and V_{ds} known from Equations (3.90) and (3.91), respectively, the fault can be simulated. The simulation results of this fault are shown in Figures 3.27-3.28 with a load (10N.m) already applied in steady state. The rotor speed continues to drop, and shown also is the phase 'a' voltage which is zero due to the short circuit.

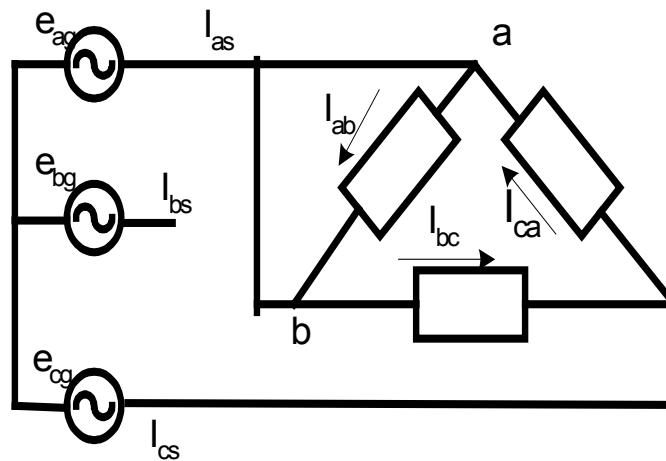


Figure 3. 26 Shows a delta-connected Induction machine with phase 'a' short-circuited.

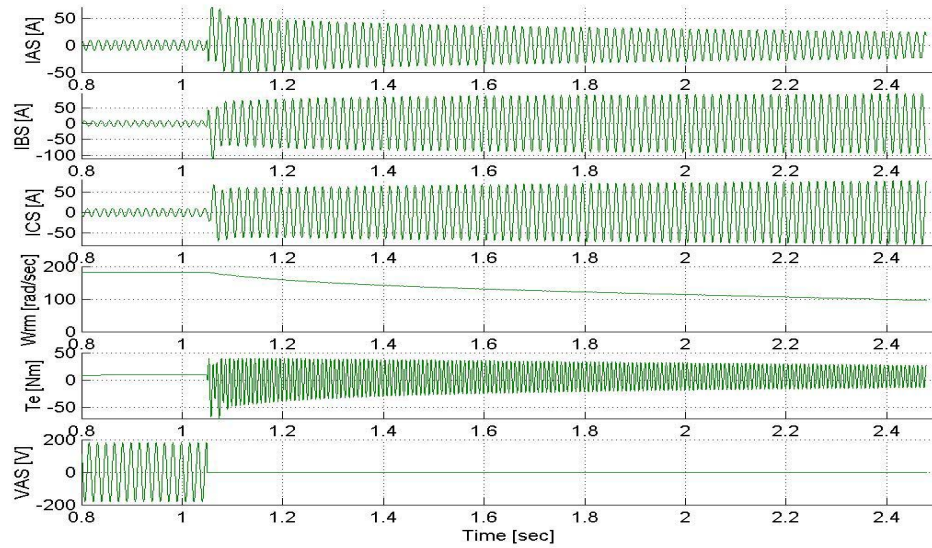


Figure 3. 27 Shows a delta-connected Induction machine with phase ‘a’ short-circuited with 104V three-phase supply with load applied, from top: phase currents ‘a’, ‘b’, ‘c’, mechanical speed, torque, phase voltage.

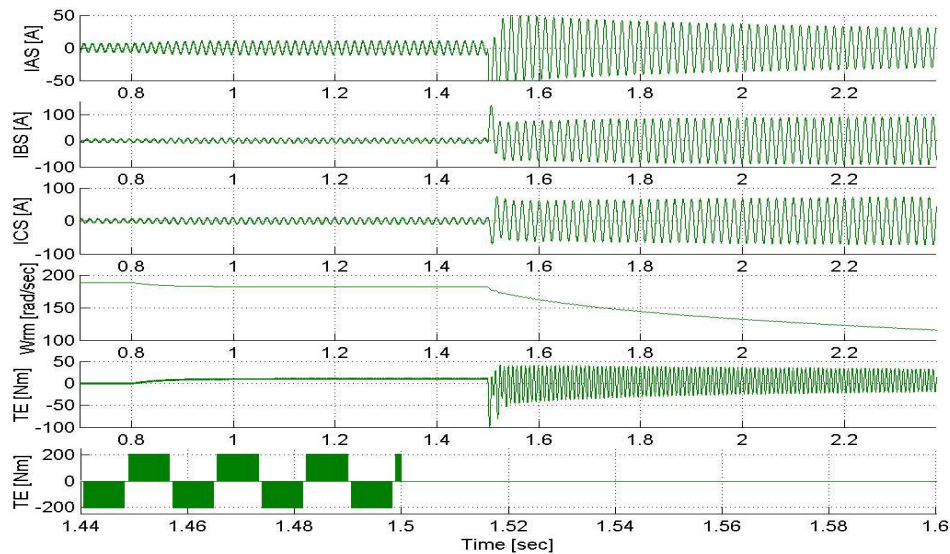


Figure 3. 28 Shows a delta-connected Induction machine with phase ‘a’ short-circuited with PWM-VSI supply with load applied, from top: phase currents ‘a’, ‘b’, ‘c’, mechanical speed, torque, phase voltage.

CHAPTER 4

A THREE-PHASE VOLTAGE SOURCE INVERTER WITH A FAULTED LEG

4.1 Introduction

One approach suggested to ensure motor drive operation when one of the inverter phase legs (power converter faults) is broken/damaged is the use of a split DC capacitor arrangement shown also in Figure 4.2. When it is sensed that an inverter leg has been lost, the motor phase winding connected to the broken leg is transferred to midpoint of the split capacitors. The modulation signals in the two other phase legs are re-configure to generate three phase balanced voltages. The scheme allows continuous operation of the machine instead of being shut down, hence, increasing the reliability of the drive system.

4.2 System Model

Figure 4.1 shows the structure of a three-phase VSI-PWM inverter with six switches connected to a Y-connected three-phase ac induction motor at adjustable voltage and frequency. With a fault on one of the inverter legs, the VSI-PWM inverter can be modeled with four power switches and a two-split capacitor dc high voltage link as shown in Figure 4.2.

From Figure 4.2, it is assumed that the fault is on phase A leg of the inverter in which the two switches S_{ap} and S_{an} are replaced by capacitors C_1 and C_2 . This inverter-

switching requirement can be stated as follows. Given a desired set of three-phase voltages and a set of three-phase currents for the output of the inverter:

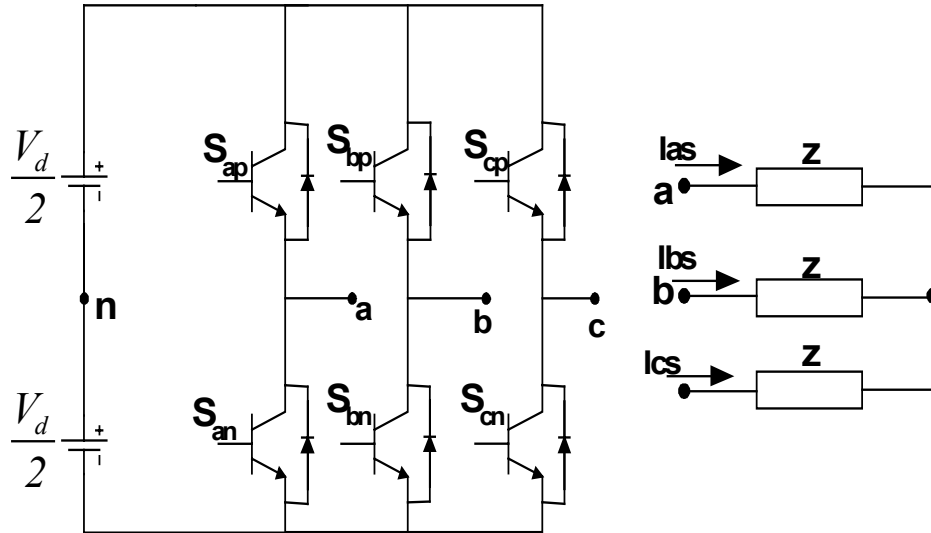


Figure 4. 1 Conventional PWM-VSI inverter system.

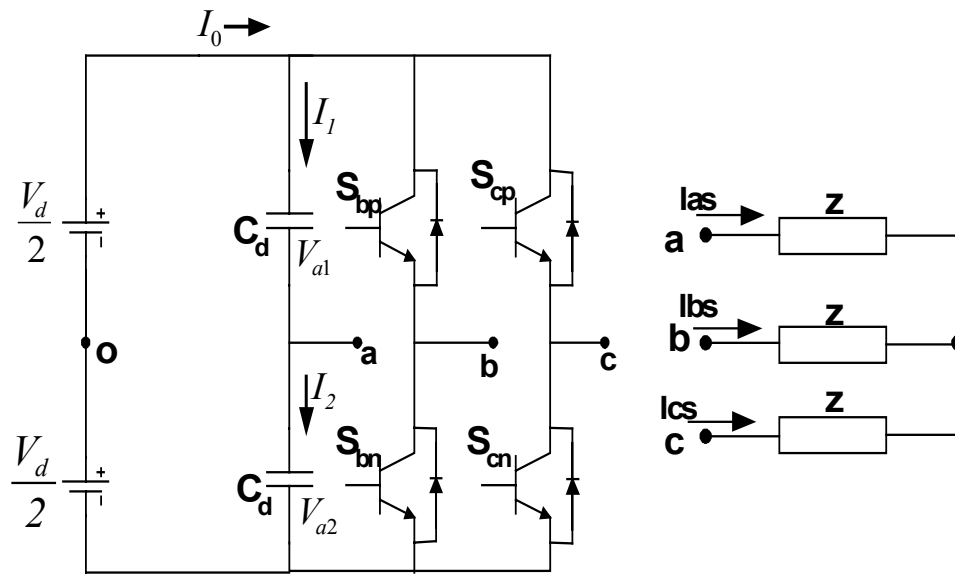


Figure 4. 2 PWM-VSI topology with a split DC capacitor replacing the faulted phase of the PWM-VSI inverter system

$$\begin{aligned}
V_{as} &= V_0 \cos(\omega_0 t) \\
V_{bs} &= V_0 \cos\left(\omega_0 t - \frac{2\pi}{3}\right) \\
V_{cs} &= V_0 \cos\left(\omega_0 t + \frac{2\pi}{3}\right)
\end{aligned} \tag{4.1}$$

where V_0 is the magnitude of the output voltages.

Determining the modulation function, S , that will produce a desired set of line-to-ground voltages:

$$\begin{bmatrix} V_{bs} + V_{s0} \\ V_{cs} + V_{so} \end{bmatrix} = \begin{bmatrix} S_{bp} & S_{bn} \\ S_{cp} & S_{cn} \end{bmatrix} \begin{bmatrix} \frac{V_d}{2} \\ -\frac{V_d}{2} \end{bmatrix}, \tag{4.2}$$

$$S_{bp} + S_{bn} = 1; S_{cp} + S_{cn} = 1; \tag{4.3}$$

$$V_{as} + V_{so} = V_{a2} - \frac{V_d}{2} \tag{4.4}$$

and the dc capacitor voltages V_{a1} and V_{a2} are given by

$$V_{a1} + V_{a2} = V_d . \tag{4.5}$$

It can be shown by substituting Equation (4.3) into (4.2) that

$$\frac{V_d}{2} [2S_{bp} - 1] = V_{bs} + V_{so} \tag{4.6}$$

$$\frac{V_d}{2} [2S_{cp} - 1] = V_{cs} + V_{so} . \tag{4.7}$$

Since $V_{as} + V_{bs} + V_{cs} = 0$ for a balance load voltage then,

$$V_{so} = \frac{V_{a2}}{3} - \frac{V_d}{2} + S_{bp} \frac{V_d}{3} + S_{cp} \frac{V_d}{3} . \quad (4.8)$$

Substituting V_{so} into the expressions in Equations (4.6) and (4.7), the resulting equations can be solved as follows:

$$\begin{bmatrix} 2V_d & -V_d \\ -V_d & 2V_d \end{bmatrix} \begin{bmatrix} S_{bp} \\ S_{cp} \end{bmatrix} = \begin{bmatrix} 3V_{bs} + V_{a2} \\ 3V_{cs} + V_{a2} \end{bmatrix}$$

$$V_{as} = \frac{2}{3}V_{a2} - \frac{V_d}{3}S_{bp} - \frac{V_d}{3}S_{cp} . \quad (4.9)$$

Defining the modulation function for the devices as

$$S_{bp} = \frac{1}{2}(1 + M_b)$$

$$S_{cp} = \frac{1}{2}(1 + M_c) \quad (4.10)$$

where from Equation (4.9):

$$S_{bp} = \frac{1}{V_d}(2V_{bs} + V_{cs} + V_{a2})$$

$$S_{cp} = \frac{1}{V_d}(2V_{cs} + V_{bs} + V_{a2}) . \quad (4.11)$$

Combining Equations (4.10) and (4.11), the modulating signals M_b and M_c needed to synthesis the desired three-phase voltage can be defined as

$$M_b = \frac{2(2V_{bs} + V_{cs})}{V_d} + \frac{2V_{a2}}{V_d} - 1$$

$$M_c = \frac{2(2V_{cs} + V_{bs})}{V_d} + \frac{2V_{a2}}{V_d} - 1 \quad (4.12)$$

for operation in the linear region, the modulation index M is defined in Volt/Hertz as follows:

$$M = \frac{2\sqrt{3}V_0}{V_d}, \quad |M| \leq 1. \quad (4.13)$$

The input current I_o will be

$$\begin{aligned} I_o &= I_{bs}S_{bp} + I_{cs}S_{cp} + C_d pV_{a1} \\ -I_o &= I_{bs}S_{bn} + I_{cs}S_{cn} - C_d pV_{a2} \end{aligned} \quad (4.14)$$

where capacitor $C_1 = C_2 = C_d$, it can be shown that

$$V_{a2} - V_{a1} = \frac{1}{C_d} \int (I_{bs} + I_{cs}) = -\frac{1}{C_d} \int I_{as} dt = \sigma \quad (4.15)$$

from Equation (4.5), V_{a2} and V_{a1} can be expressed as follows:

$$\begin{aligned} V_{a2} &= \frac{V_d}{2} + \frac{\sigma}{2} \\ V_{a1} &= \frac{V_d}{2} - \frac{\sigma}{2}. \end{aligned} \quad (4.16)$$

4.3 Simulation Results

This sections investigates the characteristic response of this model when connected to a star-connected Induction machine (IM). The computer simulation under free acceleration at rated frequency is carried out and the result is as shown in Figure 4.3. The Induction machine is also connected to a load of 10N.m at the rated frequency of 60Hz at steady state and also removed after sometime and the simulation result is as

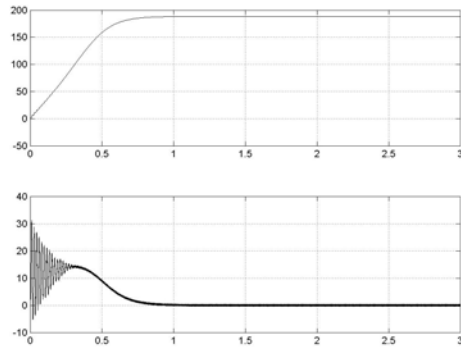
Table 4. 1 Induction Machine Parameters

Rated Line Voltage	220 V
Stator Resistance, R_s	0.435 ohms
Stator Leakage Inductance, L_{ls}	2 mH
Rotor Resistance, R_r	0.816 ohms
Rotor Leakage Inductance, L_{lr}	2 mH
Mutual Inductance, L_{ms}	0.0693 H
No. of Poles, P	4
Synchronous Speed, W_e	377 rad/sec
Inertia, J	0.04 kg/m ²

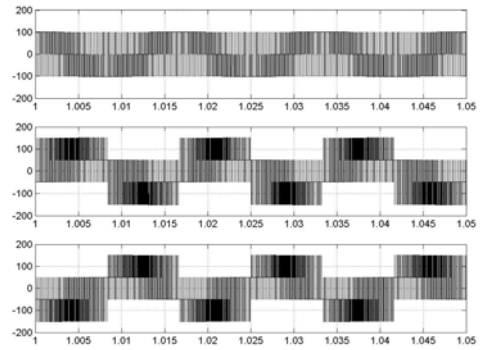
shown in Figure 4.4.

The simulation results for three other different frequencies 5Hz, 30Hz, and 70Hz with load connected are as shown in the Figures 4.5,4.6, and 4.7, respectively. The machine parameters used are as shown in Table 4.1 and the two capacitors ($C_1=C_2=C_d$) are 2000 μ F.

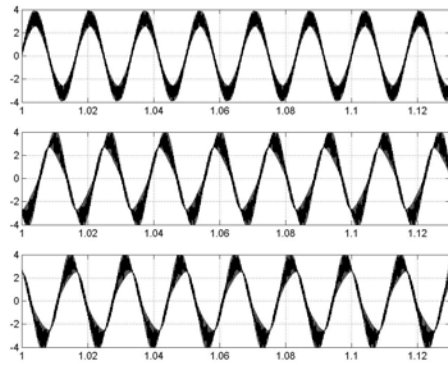
The simulation was carried out with the machine operating with the three VSI-PWM intact and then a fault occur in one of the leg, the fault was sensed and the modulation scheme is switched to the scheme describe above almost immediately to keep the machine in operation. Figure 4.8 shows the simulation result for this case. With the capacitor replaced with a larger value of 50000 μ F (the capacitors voltage charged to $V_{a1} = V_{a2} = V_d/2$ during the period of no failure in any of the switches) to be able to retain the DC voltage when fault occurs. The fault occurs at 1.3sec. and as shown in Figure 4.8, the induction motor experiences a little drop in speed but most of all there is no stoppage in operation, hence, increasing the availability of the machine despite loss of an inverter leg.



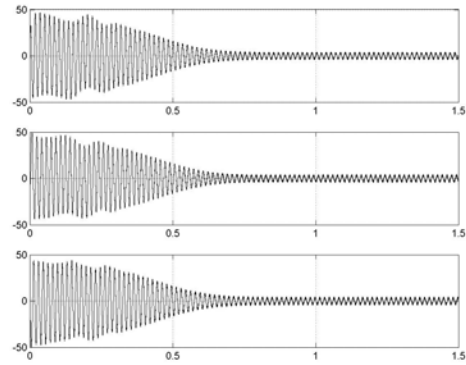
(a)



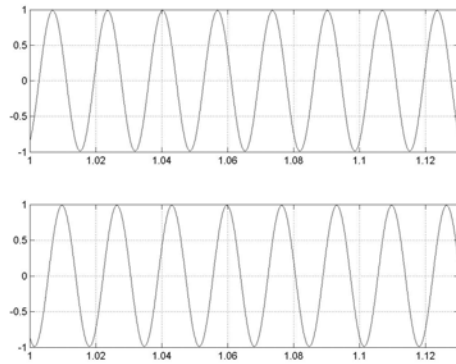
(b)



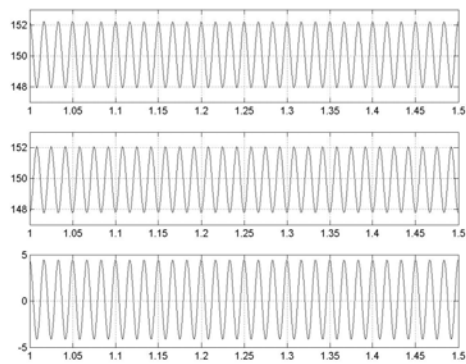
(c)



(d)

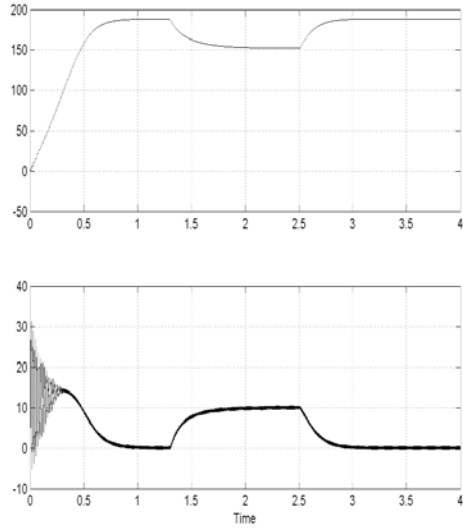


(e)

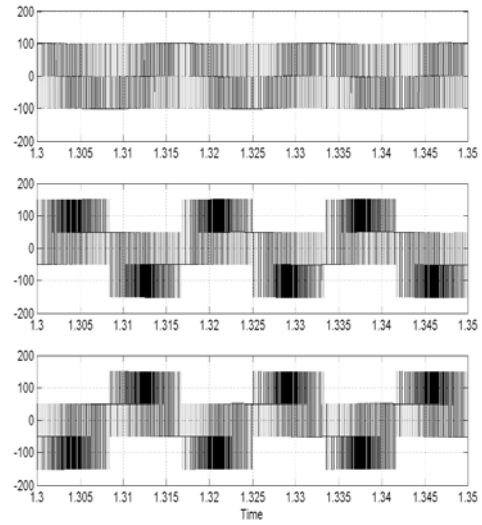


(f)

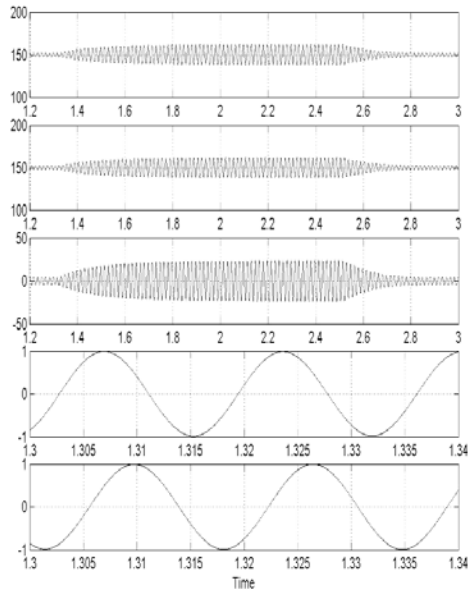
Figure 4. 3 Shows free acceleration characteristic of the Induction Machine (a) top: Speed, bottom: Torque (b) Stator phase Voltages from top: a,b,c (c) Steady state Stator current (d) Transient response of the stator current (e) Modulating signal top: M_b , bottom: M_c (f) Top: upper capacitor v_{a2} , middle: lower capacitor v_{a1} , bottom: difference of the two-capacitor $v_{a2}-v_{a1}$



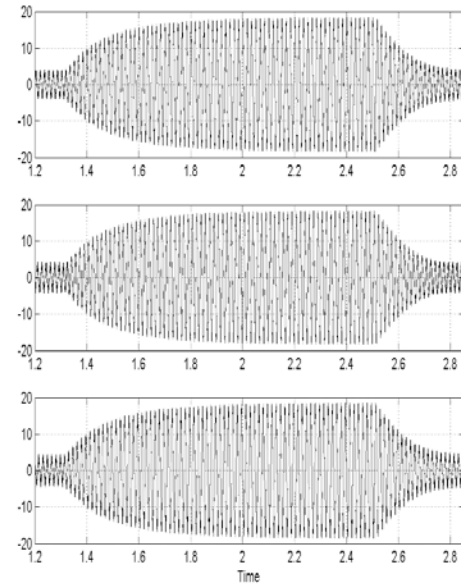
(a)



(b)

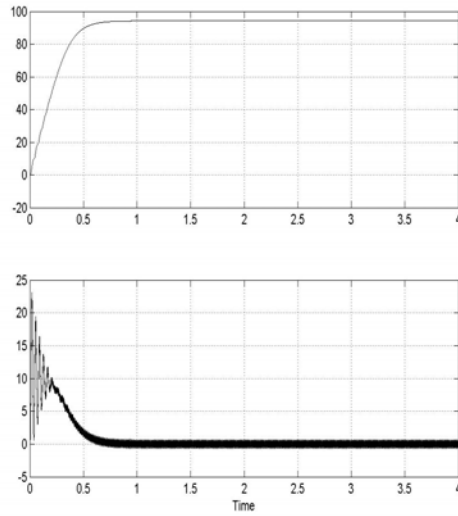


(c)

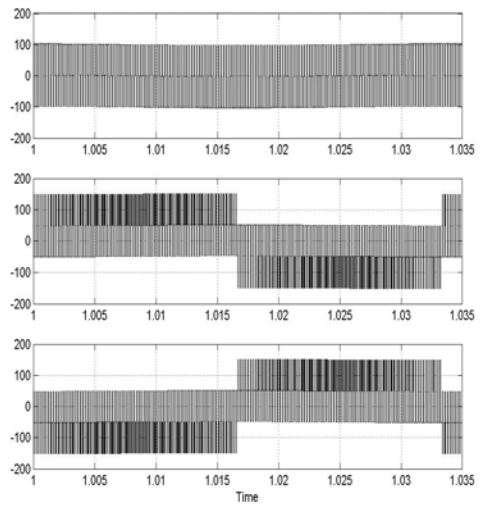


(d)

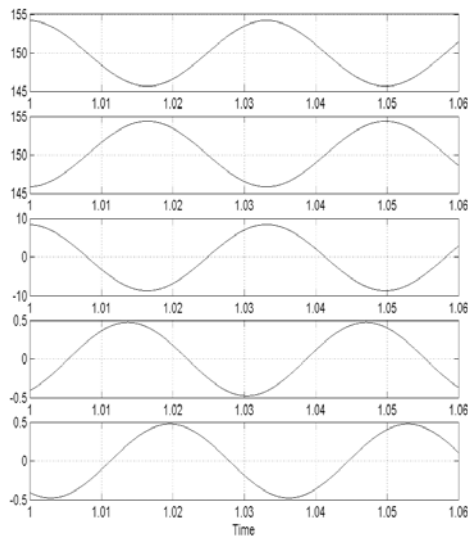
Figure 4. 4 Shows Induction Machine with load 10N.m at steady state and remove afterwards (a) top: Speed, bottom: Torque (b) Stator phase Voltages from top: a,b,c (c) From Top: lower capacitor v_{a1} , upper capacitor v_{a2} , difference of the two-capacitor $v_{a2}-v_{a1}$, Modulating signal M_b , Modulating signal M_c (d) Steady state Stator current.



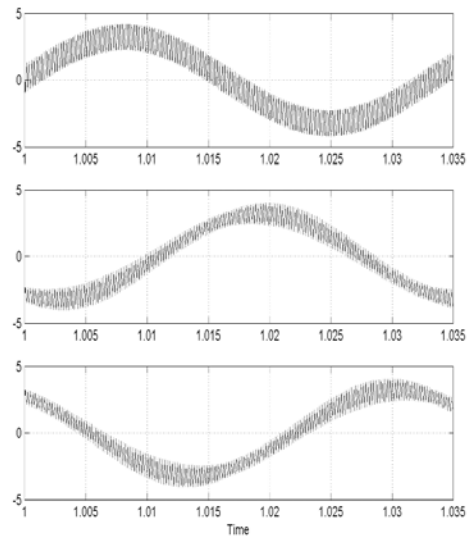
(a)



(b)

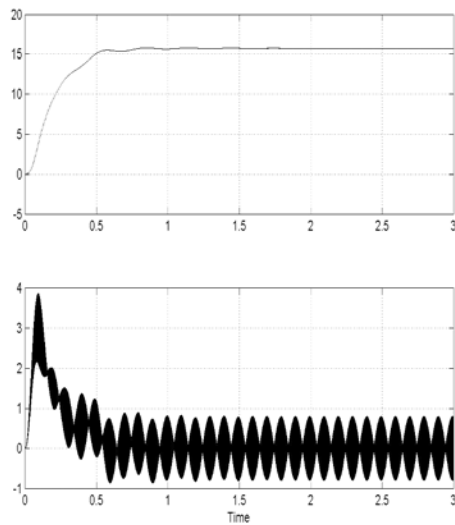


(c)

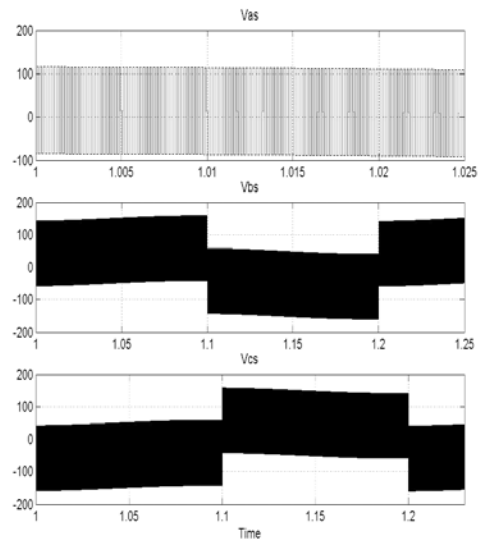


(d)

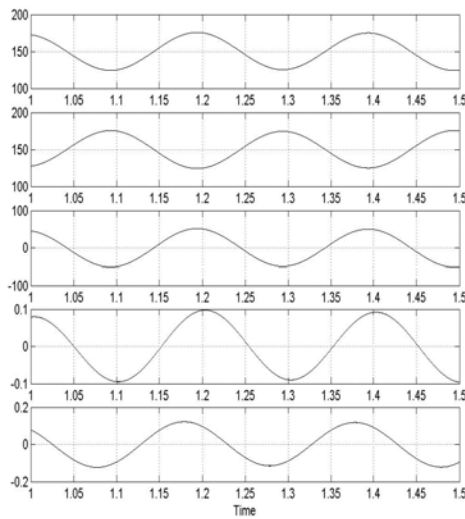
Figure 4. 5 Shows free acceleration characteristic of the Induction Machine at 30Hz (a) top: Speed, bottom: Torque (b) Stator phase Voltages from top: a,b,c (c) From Top: lower capacitor v_{a1} , upper capacitor v_{a2} , difference of the two-capacitor $v_{a2}-v_{a1}$, Modulating signal M_b , Modulating signal M_c (d) Steady state Stator current.



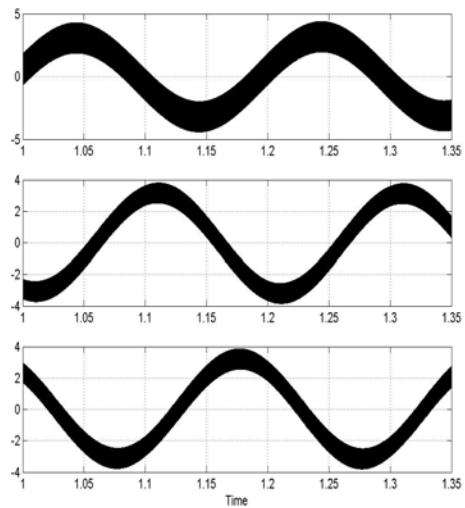
(a)



(b)

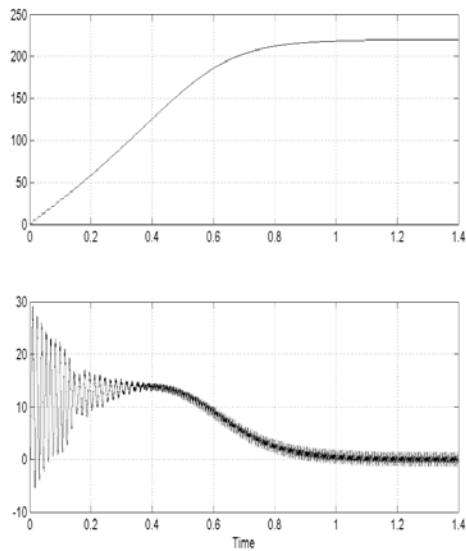


(c)

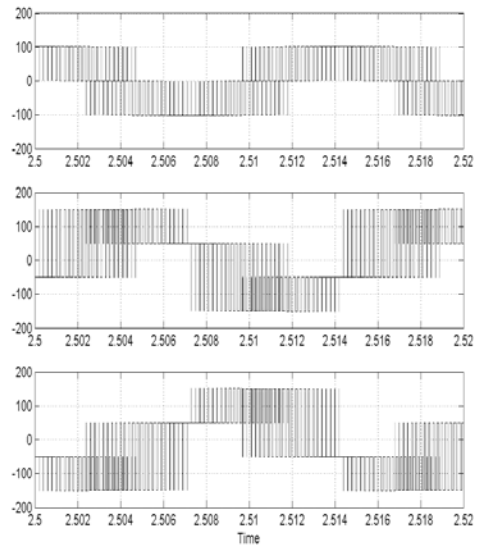


(d)

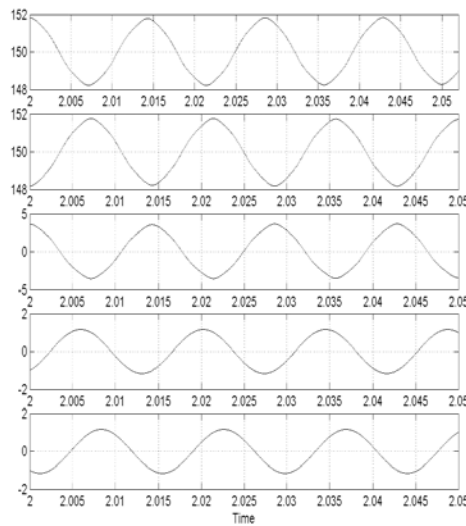
Figure 4. 6 Shows free acceleration characteristic of the Induction Machine at 5Hz (a) top: Speed, bottom: Torque (b) Stator phase Voltages from top: a,b,c (c) From Top: lower capacitor v_{a1} , upper capacitor v_{a2} , difference of the two-capacitor $v_{a2}-v_{a1}$, Modulating signal M_b , Modulating signal M_c (d) Steady state Stator current.



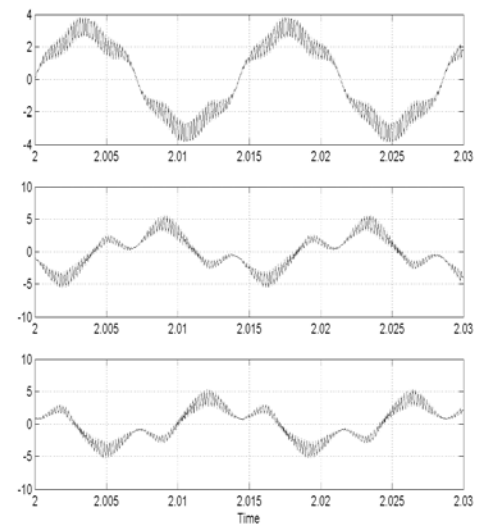
(a)



(b)

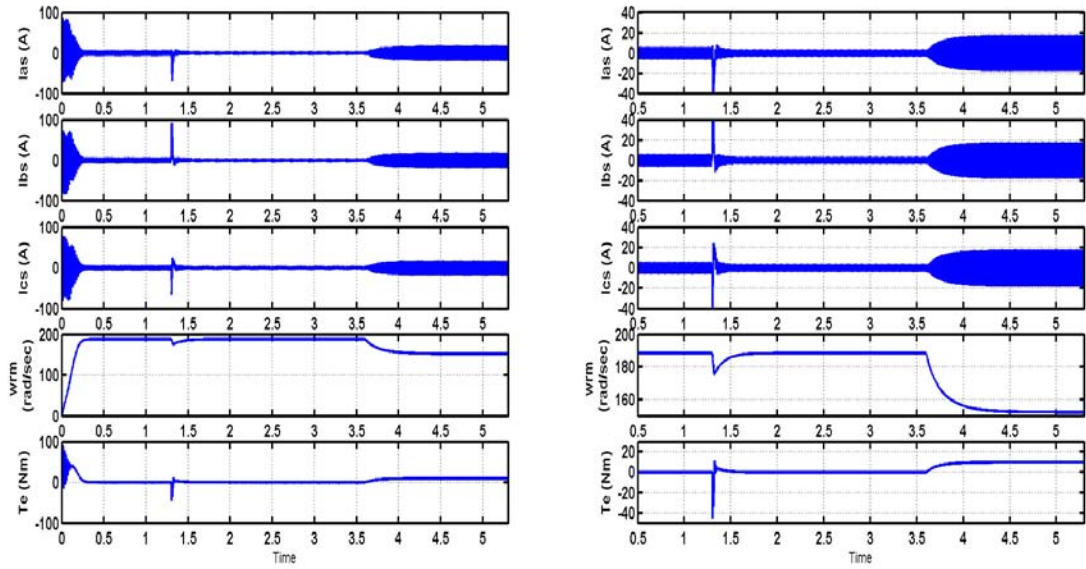


(c)

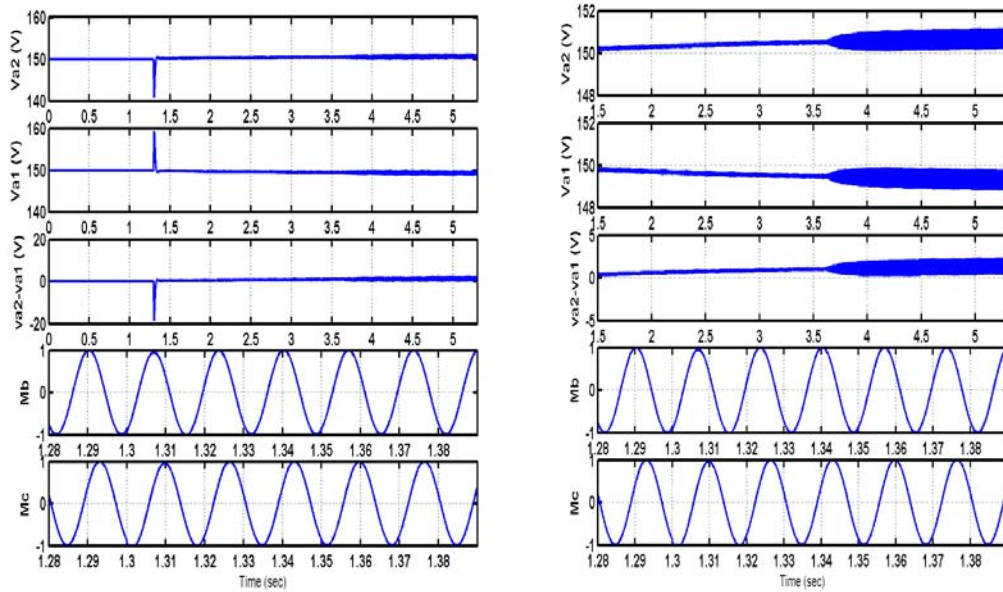


(d)

Figure 4. 7 Shows free acceleration characteristic of the Induction Machine at 70Hz (a) top: Speed, bottom: Torque (b) Stator phase Voltages from top: a,b,c (c) From Top: lower capacitor v_{a1} , upper capacitor v_{a2} , difference of the two-capacitor $v_{a2}-v_{a1}$, Modulating signal M_b , Modulating signal M_c (d) Steady state Stator current.



(a)



(b)

Figure 4. 8 Shows the transient and steady state response of the Induction Machine at 60Hz (a) top: phase “a” current; phase “b” current; phase “c” current; Speed w_{rm} ; Torque, T_e (b) From Top: lower capacitor v_{a1} , upper capacitor v_{a2} , difference of the two-capacitor $v_{a2}-v_{a1}$, Modulating signal M_b , Modulating signal M_c (c) Steady state Stator current.

CHAPTER 5

PARAMETER DETERMINATION

5.1 Introduction

Experimental tests on the two horsepower interior permanent magnet (IPM) synchronous machine to determine the parameters is reported in this chapter. Parameter determination is considered very important in order to carry out any analysis on the performance of the machine. Due to the effects of saturation at heavy load and demagnetization of the magnet at light loads, the parameters of the machine changes significantly as the load presented to it changes. Thus, the parameters, namely, the direct and quadrature axes inductances L_d and L_q and the magnet flux linkage, λ_m , created by the magnet, must be functions of the operating conditions.

Generally, when effects due to saturation are included in an analysis, the parameters are made functions of either the total mutual flux λ_m or the total stator current I_s . The decision was made to make the parameters functions of stator peak current because, when the parameters were plotted as a function of flux, there were regions in which two possible values of a particular parameter exists for a given value of flux (which could be problematic when solving equations to determine which of the value is right to be use). Since the magnet flux linkage λ_m is also a varying parameter which vary with load due to saturation, it is necessary to determine its variation for different load

conditions, hence, there is justification in making the parameters functions of the stator current.

An equivalent circuit of the interior permanent magnet (IPM) synchronous machine without the iron loss is considered in this analysis, hence the effects of iron loss on the flux level and the harmonic fields produced by saturation cannot be modeled in this circuit. No-load as well as loaded operating conditions of the machine (as a generator and motor) are taken into account for the determination of the machine parameters. A method of determining the magnet flux linkage with respect to the air gap voltage value at different operating conditions.

5.2 Experiments to Determine the Parameters

Figure 5.1 shows the d-q axes equivalent circuits of the IPMSM without considering the effect of iron loss.

The conventional d-q voltage equations in the synchronous reference frame for the IPMSM are

$$\begin{aligned} V_{qs} &= R_s I_{qs} + L_{qs} p I_{qs} + \omega_r \lambda_{ds} \\ V_{ds} &= R_s I_{ds} + L_{ds} p I_{ds} - \omega_r \lambda_{qs} \end{aligned} \quad (5.1)$$

where

$$\lambda_{ds} = L_{ds} I_{ds} + \lambda_m, \quad \lambda_{qs} = L_{qs} I_{qs} . \quad (5.2)$$

Under steady-state (when the damper transients have decayed to negligible levels, hence not included in the analysis of the IPM), the derivatives of the state variables of Equation (5.1) are zero so, at steady state the voltage equations may be written as

$$\begin{aligned} V_{qs} &= R_s I_{qs} + \omega_r \lambda_{ds} = R_s I_{qs} + \omega_r L_{ds} I_{ds} + \omega_r \lambda_m \\ V_{ds} &= R_s I_{ds} - \omega_r \lambda_{qs} = R_s I_{ds} - \omega_r L_{qs} I_{qs} . \end{aligned} \quad (5.3)$$

The stator resistive values R_s was found by applying a dc voltage across two terminals of the stator and measuring both the voltage and the current which flowed through the terminals (shown in Figure 5.2). The stator resistance for a single phase is given as

$$R_s = \frac{V_{dc}}{2I_{dc}} . \quad (5.4)$$

The value of the stator resistance was found to be 1.5 Ω .

The voltage and currents in Equation (5.3) were found by varying a three phase balanced resistive load from a high value to a low value and recording the terminal voltage and the current output from the machine when running as a generator.

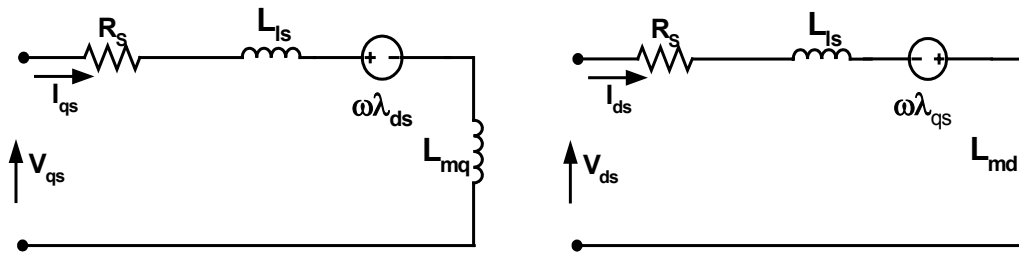


Figure 5. 1 Electric equivalent circuit model of an Interior Permanent Magnet Synchronous Motor (IPMSM) without iron-loss.

The measurements made were line to line voltages and phase currents. In order to convert the voltages and currents to their dq components, the torque angle δ was needed. The power factor of the machine is also needed in parameter determination, but, since the generator was feeding a resistive load, the current out of the generator was in phase with the voltage at the terminals, so the power factor was unity. The torque angle was found by measuring the difference in angle of the voltages of the search coil located across phase “A” of the stator and the terminal voltage appearing at the stator terminal of phase “A.” This method was not an ideal way to measure the torque angle because the oscilloscope used to measure the angle between the two voltages gave a varying readout even though the load and speed of the generator were constant. An average of the numbers was taken and used as the torque angle. It would have been much easier (probably more accurate) to have a commercially available torque angle measuring device, stroboscope; however, no such device was available. Nevertheless, the strong corroboration between measured and predicted results suggests that the method used was

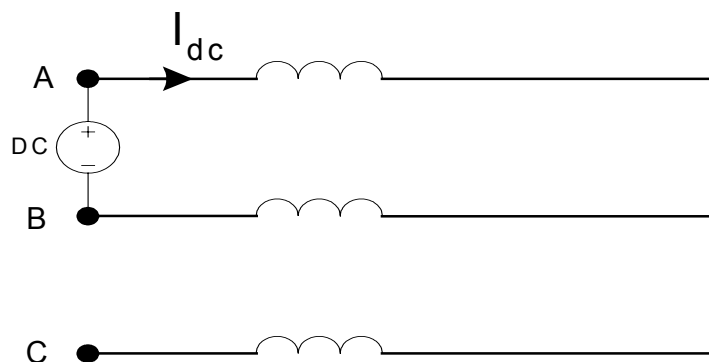


Figure 5. 2 schematic diagram of dc test used to determine the stator resistance

an acceptable means of obtaining the torque. Once the stator voltages, currents, and torque angle are known, the dq voltages and currents can be found as follows:

$$\begin{aligned}
 V_{qs} &= V_s \cos(\delta) \\
 V_{ds} &= -V_s \sin(\delta) \\
 I_{qs} &= I_s \cos(\gamma) \\
 I_{ds} &= -I_s \sin(\gamma)
 \end{aligned} \tag{5.5}$$

where V_s is the peak line to neutral voltage, I_s is the peak stator current, and γ is the sum of the torque angle δ and the power factor angle θ . Since the power factor is unity (since the generator is feeding a purely resistive load), then γ is equal to δ .

With the dq voltages and currents and the stator resistance known, the inductance in the q axis can easily be found and is given as

$$L_{qs} = -\frac{V_{ds} - R_s I_{ds}}{\omega_r I_{qs}} \tag{5.6}$$

The inductance in the d axis and the magnet flux linkage are not easy to find as the q axis inductance. As stated in [77], it is not possible to separate the induced magnet EMF ($\omega_r \lambda_m = E_o$) from the product of I_{ds} and X_{ds} ($\omega_r L_{ds}$) at load.

One method of finding the magnet flux involves running a no load test on the PM machine for a range of frequencies and measuring the terminal voltage of the machine and the voltage across the terminals of the search coil. An empirical relationship between the search coil voltage and the magnet (and thus the magnet flux linkage) can be developed since, at a no load condition, the terminal voltage of the machine is equal to

the magnet voltage. Figure 5.3 shows the plot of the rms voltage of the magnet vs. the air gap voltage for both the series connection (high voltage) and parallel connection (low voltage) of the stator winding of the PM machine while Table 5.1 shows the experimental data.

The low voltage connection was not used in any of the experiments reported in this thesis (except for the one just described). The main reason for this is that, since the machine is being operated in generator mode, one would normally like a high terminal voltage and the low voltage is, as one would expect, one half of the terminal voltage of the high voltage connection for any particular operating frequency.

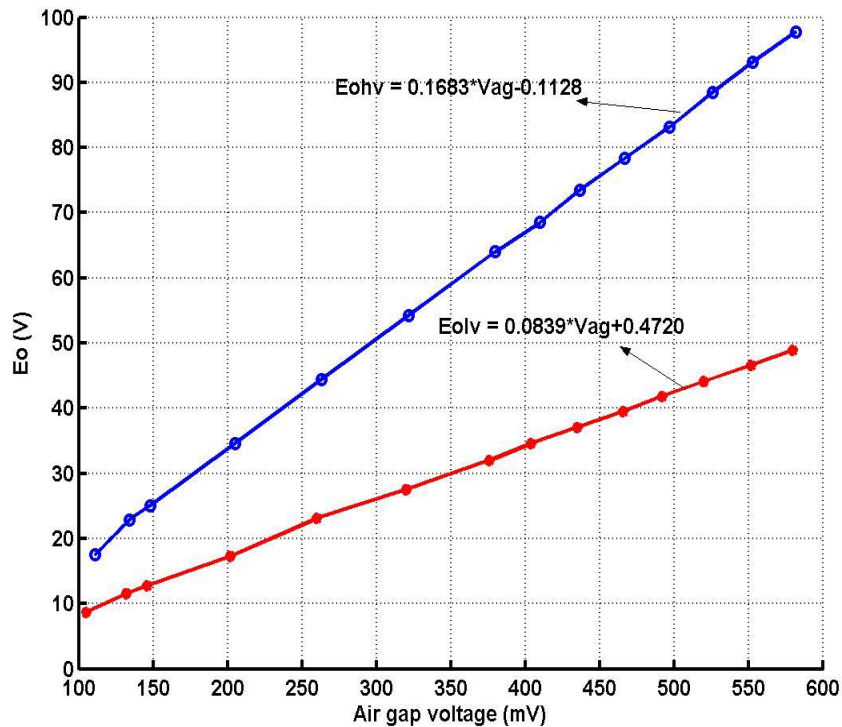


Figure 5. 3 Measured line to neutral terminal generator voltage (rms) vs air gap voltage for no load condition for machine connected in high and low voltage stator connections

Table 5. 1 Experimental measurements at no-load condition

Low voltage connection				
V _{ab} (rms)	V _{bc} (rms)	V _{ca} (rms)	V _{ag} (rms)	f _s (Hz)
15	15	15	105	7
20	20	20	132	9
22	22	22	146	10
30	30	30	202	14
40	40	40	260	18
49	47	47	320	22
56	55	55	376	26
60	59	60.5	404	28
64.5	64	64	435	30
69	68	68	466	32
73	71	73	492	34
77	76	76	520	36
81	80	81	552	38
85	84	85	580	40
High voltage connection				
29	31	31	111	7
39	40	40	134	9
42	44	44	148	10
60	60	60	205	14
77	77	77	263	18
95	93	94	322	22
112	110	110.5	380	26
120	117	119	410	28
129	126	127	437	30
137	134	136	467	32
146	142	144	497	34
154	152	154	526	36
162	160	162	553	38
170	168	170	582	40

This brings up one other interesting point, which is that one would ideally like to have a generator having a magnet voltage greater than 120 volts rms when operating at 60 Hertz since most loads were designed to operate at or near that particular voltage. Although not shown explicitly on Figure 5.3, the machine is operating at 60 Hertz when the air gap voltage is approximately 520mV.

This operating point corresponds to a magnet voltage of about 88 Volts line to neutral rms which is certainly low if one wanted to drive, for example an induction motor with it. Incidentally, the lower voltage of this IPM machine is not an indication of poor design; rather, it is an indication that it was designed to be used as a motor.

The empirical relationship between the air gap voltage (V_{ag}) and the magnet voltage on a per phase rms basis (E_o) was found to be

$$E_o = 0.1683 * V_{ag} - 0.1128 . \quad (5.7)$$

With this relationship established, the magnet voltage (and thus the magnet flux) could be approximated under load conditions by measuring the air gap voltage at each operating condition. While this is not entirely accurate since, under load conditions, the voltage across the search coil is also affected by the current flowing in the mutual inductances of the d and q windings of the stator, the approximation seems reasonable.

After the magnet flux term has been determined (by $\lambda_m = E_o / \omega_r$), then L_{ds} can be found by

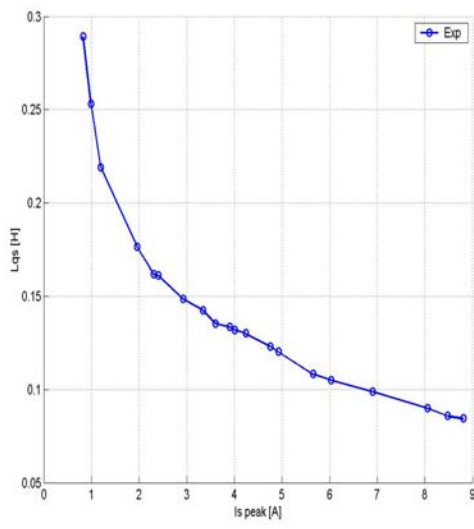
$$L_{ds} = \frac{V_{qs} - R_s I_{qs} - \omega_r \lambda_m}{\omega_r I_{ds}} . \quad (5.8)$$

The plots of L_{qs} , L_{ds} , and λ_m are given in Figure 5.4, while Table 5.2 shows the experimental data for load test with measurements of the line voltages (rms), phase

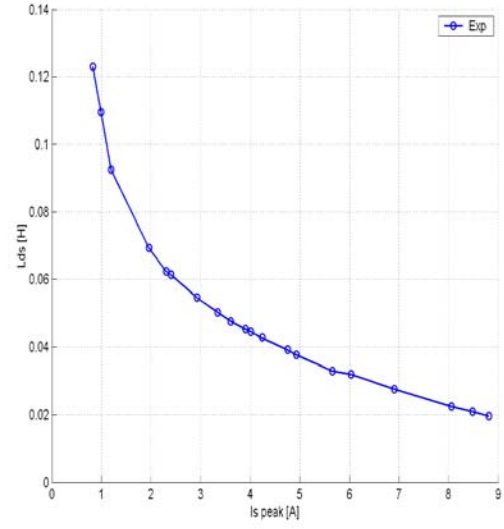
current (rms), air gap voltage (rms), and the torque angle δ recorded. The empirical relationships of the parameters as a function of peak stator current I_s are given as

$$\begin{aligned}\ln\left(\frac{1}{L_{qs}}\right) &= -0.013I_s^4 + 0.0293I_s^3 - 0.2303I_s^2 + 0.8684I_s + 0.790 \\ \ln\left(\frac{1}{L_{ds}}\right) &= -0.011I_s^4 + 0.0251I_s^3 - 0.210I_s^2 + 0.9096I_s + 1.505 \\ \lambda_m &= 0.0002I_s^3 - 0.0041I_s^2 + 0.0208I_s + 0.1863 .\end{aligned}\quad (5.9)$$

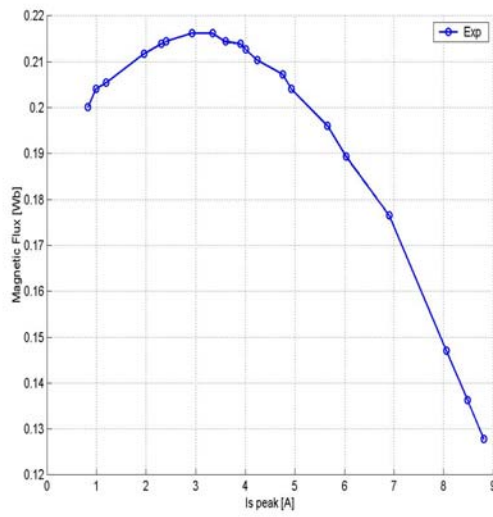
As described earlier, burying the magnets inside the rotor of the IPM synchronous motor has several important effects on the machine's electromagnetic characteristics—some rather obvious and others subtler. The key to understanding these effects is recognition that covering each magnet with an iron pole piece creates high-permeance paths for the magnetic flux across these poles and orthogonal to the magnet flux. This saliency effects on the IPM motor distinguishes it from conventional wound-rotor salient synchronous machines by the fact that the IPM stator phase inductance with direct-axis (magnet) alignment L_{ds} is less than the quadrature-axis inductance L_{qs} as shown in Figure 5.4. This phenomenon, called inverse saliency, is simply caused by the magnet depth appearing as basically an air gap in the d-axis since the incremental permeability of ceramic and rare-earth magnet materials is nearly that of free space, the magnet thicknesses appear as large series air gap in the d-axis magnetic flux paths.



(a)



(b)



(c)

Figure 5. 4 Stator q and d axis inductances and magnet flux (a) L_{qs} , (b) L_{ds} , (c) λ_m

Table 5. 2 Experimental measurements of the load test

$V_{ab}(V)$	$V_{bc}(V)$	$V_{ca}(V)$	$I_z(A)$	$I_b(A)$	$I_c(A)$	$-39^\circ-\delta$	$V_{ag}(V)$
23	23	23	6.2	6.2	6.3	44.5	287
37	38	38	6	6	6	42	306
54	54	54	5.7	5.7	5.7	39.4	330
90	90	90	4.9	4.85	4.9	33	396
100	100	104	4.25	4.3	4.25	30	425
112	112	114	4.0	4.0	4.0	27.5	440
120	122	121	3.55	3.5	3.4	25.6	458
123	123	124	3.35	3.4	3.35	25	465
127	127	128	3	3	3	23.1	472
129	129	130	2.82	2.85	2.84	21.8	477
130	130	133	2.73	2.75	2.8	21.2	480
131	131	133	2.5	2.6	2.55	19.5	481
134	134	135	2.35	2.4	2.35	18.5	485
135	135	136	2.05	2.1	2.05	16	485
135	135	137	1.7	1.7	1.7	13	481
135	135	137	1.6	1.7	1.6	12	480
135	134	136	1.35	1.4	1.4	10	475
133	132	132	0.81	0.88	0.85	3	461
131	132	131	0.7	0.7	0.7	2	458
129.5	130	130	0.55	0.6	0.6	1	449

CHAPTER 6
THE INFLUENCE OF MAGNETIC SATURATION AND ARMATURE
REACTION ON THE PERFORMANCE INTERIOR PERMANENT
MAGNET MACHINES

6.1 Introduction

The employment of vector-controlled ac motors, especially induction motor, permanent magnet synchronous motor, synchronous reluctance motor has become standard in industrial drives, the improvement of ac motor drives has been important issue. For this reason, several authors have made an attempt to consider iron loss in vector controlled ac motor drives.

This thesis makes use of finite element method to determine the q and d axis inductance of this interior permanent magnet synchronous motor; modeling and analysis of the machine; investigate the influence of the parameters variation and iron losses on the efficiency of the interior permanent magnet synchronous motor based on the developed mathematical model using both simulations and experiment. In this model, the iron loss resistance is defined, hence there is need to determine its values experimentally.

6.2 Parameters Determination using Finite Element Method

Figure 6.1 shows the d-q axes equivalent circuits of the IPMSM which are traditionally utilized to consider iron loss. In this circuit, an iron loss resistance R_c is inserted in parallel with the armature inductance. Thus, the d-q axes line currents (I_{ds}, I_{qs}) are divided into iron loss currents (I_{cd}, I_{cq}) and magnetizing currents (I'_{ds}, I'_{qs}) .

The voltage equation of these circuits is expressed as

$$\begin{aligned} V_{qs} &= R_s I_{qs} + V_{cq} \\ V_{ds} &= R_s I_{ds} + V_{cd} \end{aligned} \quad (6.1)$$

$$\begin{aligned} V_{cq} &= L_{qs} p I'_{qs} + \omega_r \lambda_{ds} = I_{cq} R_c \\ V_{cd} &= L_{ds} p I'_{ds} - \omega_r \lambda_{qs} = I_{cd} R_c \end{aligned} \quad (6.2)$$

where

$$\begin{aligned} I_{cq} &= \frac{V_{qs} - R_s I_{qs}}{R_c} = \frac{L_{qs} p I'_{qs} + \omega_r \lambda_{ds}}{R_c} \\ I_{cd} &= \frac{V_{ds} - R_s I_{ds}}{R_c} = \frac{L_{ds} p I'_{ds} - \omega_r \lambda_{qs}}{R_c} \end{aligned} \quad (6.3)$$

$$I_{qs} = I'_{qs} + I_{cq}, \quad I_{ds} = I'_{ds} + I_{cd} \quad (6.4)$$

$$\lambda_{ds} = L_{ds} I'_{ds} + \lambda_m, \quad \lambda_{qs} = L_{qs} I'_{qs} \quad (6.5)$$

where V_{ds} and V_{qs} are the d- and q-axis components of the terminal voltage, L_{ds} and L_{qs} are the d- and q-axis components of armature self-inductance, λ_{ds} and λ_{qs} are the d- and

q-axis components of the flux linkage, λ_m is the magnet flux, and p is differential operator define as $\frac{d}{dt}$.

Under steady state operation, the q-d variables are constant given in Equations (6.1- 6.5), and their derivatives with respect to time are zero.

The measured values of the load-dependent parameters, d- and q-axis inductance as well as the magnet flux linkage due to the magnet, have been determined experimentally as described in Chapter 5 earlier. These measurements uses Equations (6.1-6.5) in steady-state to estimate the parameters. The measured values are shown in Figure 5.4 plotted against the peak stator current.

In Figure 6.2(a-c) (with Figure 5.4 included), the variation of the d- and q-axis inductances and the magnet flux linkage are shown indicating that both the inductances are current dependent reflecting the influence of current distribution on the air-gap flux density. The magnet flux linkage also changes due to the influence of stator current armature reaction. It is observed that at low currents when the d-axis currents are

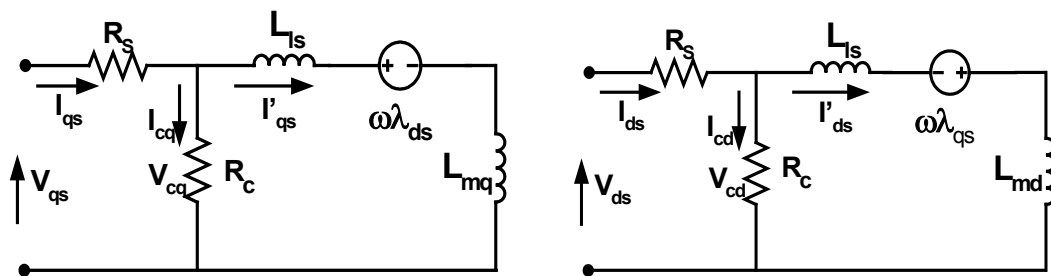


Figure 6. 1 Electric equivalent circuit model of an Interior Permanent Magnet Synchronous Motor (IPMSM) with core-loss included.

generally negative, the axis inductances are larger due to the demagnetization of the buried magnets and they tend to be smaller and relatively constant at high load currents when both the d- and q- axis currents are generally positive with the magnet operating in the magnetization mode. The shape of the magnet flux is determined by both the influence of d-axis current and the saturation of the bridge and steel parts surrounding the magnet.

The accurate calculation of saturated machine performance can be accomplished through the use of finite element magnetic field solution techniques.

As rather large values of current flow in the stator circuits of a permanent magnet motor, a sort of flux redistribution occurs due to saturation (even at no-load operations), hence, the d- and q-axis inductances changes with the armature current. The armature reaction effect on the values of the magnet flux is also noticed using this method

Figure 6.3 schematically shows the rotor design of the experimental IPM machine under consideration. The parameter and material characteristics of the 2hp, interior permanent magnet motor (in the Appendix A) was specified in the RMxpert software. By changing the rated power input in order to obtain different loading conditions of the interior permanent magnet synchronous machine, the RMxpert software (Ansoft product) is executed to determine the steady state value of the q and d axis inductance under different full load current.

There is close correlation between calculated and measured parameters at high load currents as shown in Figure 6.2(a-c) but could substantially deviate when the phase current is relatively small as the magnet is likely demagnetizing. While in almost all

published papers, the magnet flux and the q-axis inductance are considered to be constant, our experimental results and Finite Element Analysis indeed show that significant variations can be experienced by these parameters.

The air-gap flux density (B_g) is composed of three components due to the armature currents and rotor buried magnets: q and d axis flux densities (B_{aq} and B_{ad} respectively), due to the three-phase armature currents and the flux density due to the buried magnets, B_f . These components which influence the saturation of the main iron parts of the machine affect the magnitudes of the axis inductances as magnitudes and signs of the q and d-axis currents change due to changes in operating points. Of these components, the sign of the d-axis currents influences the magnitude of the d-axis flux density B_{ad} as the armature changes from magnetizing (positive d-axis current) to demagnetizing (negative d-axis current) in the process of which the permeability in the steel bridges and flux density of the magnet are greatly influenced. Consequently the axis inductances and the magnet voltage (open circuit voltage) vary [3].

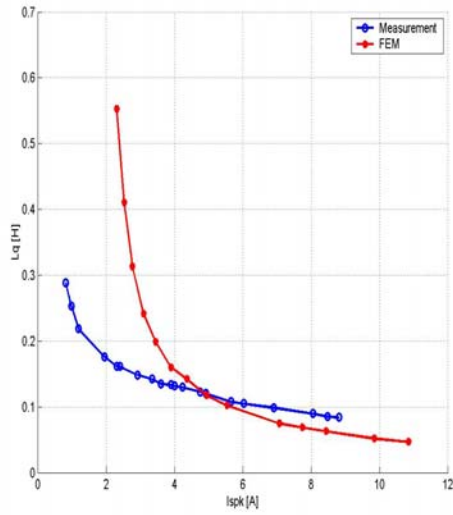
By injecting d and q axis stator current (the current define in Ansoft software called Maxwell 2D has to be ampere turns) in the stator winding of the one-quarter geometry created by the RMxpert software, the flux density plots in Figure 6.4 were obtained. Flux density plots in Figure 6.4 demonstrate the impact of current distribution in the air-gap flux density and hence, the machine parameters changes when the rated current is applied to the d-axis (the flux density diminishes) compared to when applied to the q-axis. Since the flux density is directly proportional to machine inductance, the d-axis inductance is less than the q-axis inductance. This is because the d-axis current

significantly demagnetizes the magnet and hence influences the air-gap flux. Compared to the no-load current, which reflects essentially the influence of the buried magnet, magnetization and demagnetization due to armature current increase the harmonics of the air gap flux when under load condition. The depression observed on the flux density is due to the nature of the geometry of the IPM machine, as the flux flows through the rotor and stator slots opening.

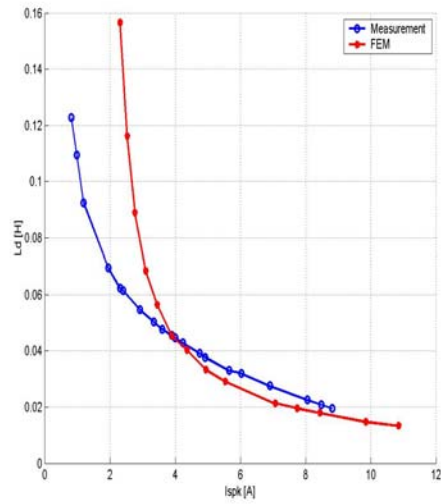
At rated condition, the steady state characteristics of the IPM synchronous machine are as shown in Figure 6.5 (a-d) and Figure 6.6 (a-d). These steady state plots confirm the advantages of the IPM synchronous motor, which is why it is being use in several application which require high acceleration and a good torque quality (as shown in Figure 6.5 (a)), the torque comprise the magnet torque and the reluctance torque; an excellent power factor close to unity (Figure 6.5 (b)), since the copper losses are essentially located only in the stator, hence, an IPM is an highly efficient machine as shown in Figure 6.5 (d). In the applications of continuous long time operation such as electric vehicles and compressor drives, the efficiency is one of the most important performances and as it is obvious from Figure 6.5 (d), the efficiency of this machine cover a wide range of operation with sufficiently high efficiency.

Figure 6.6 (b) shows the air gap flux density at no load, this is mainly the fundamental of the magnet flux density since at no-load, the magnet is the only component that contribute to the flux density along the air-gap. Figure 6.6 (d) shows the induced coil voltages at no load, which is mainly due to the magnet and this voltage is

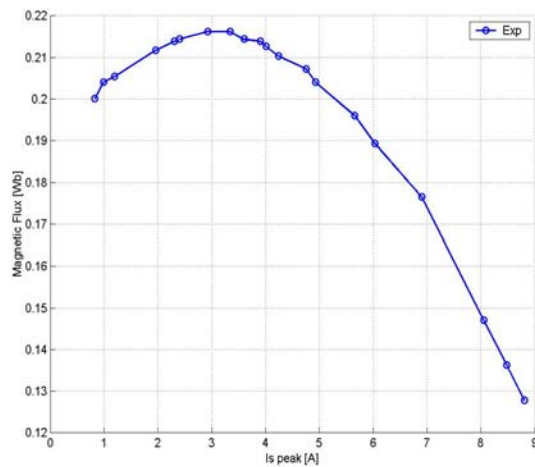
referred to as the magnet voltage; and in a slot winding, the total induced voltage is the sum of the induced voltages in one turn times the winding turns in a slot (Figure 6.5 (b)).



(a)



(b)



(c)

Figure 6. 2 Experimental and Finite Element Analysis results for a 2hp IPM. (a) q-axis inductance, (b) d-axis inductance, (c) magnet flux linkage.

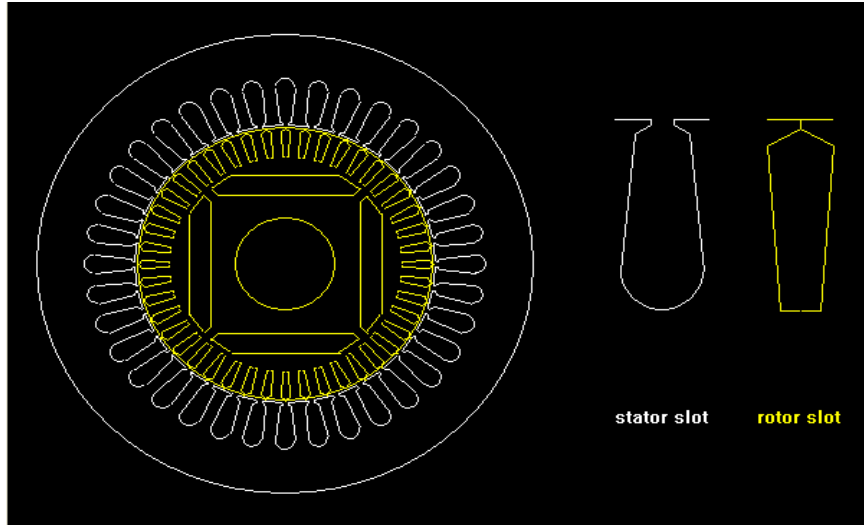
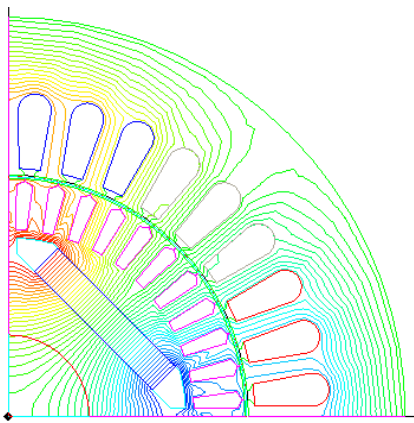
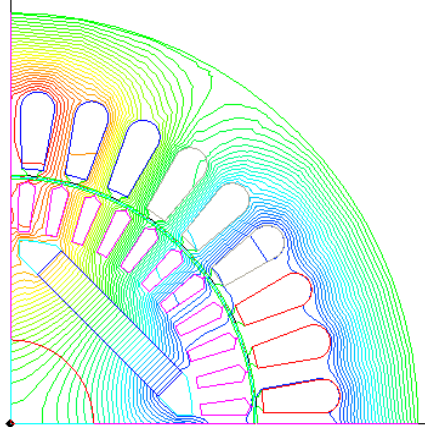
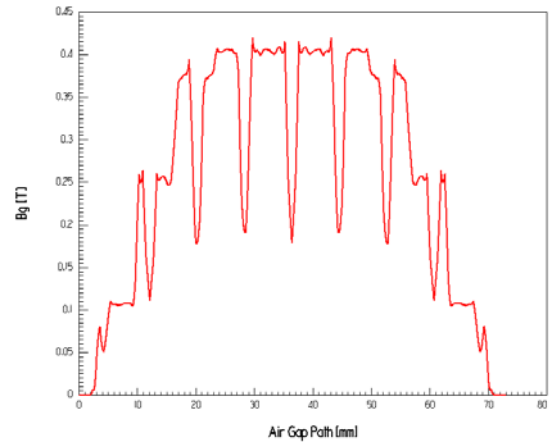


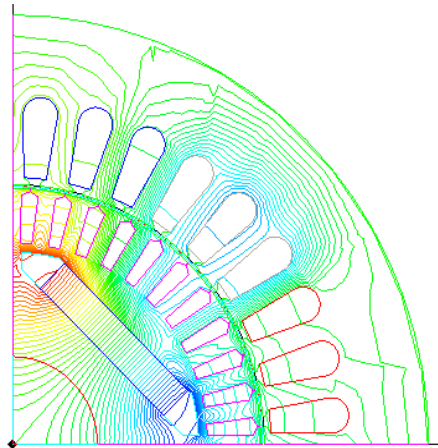
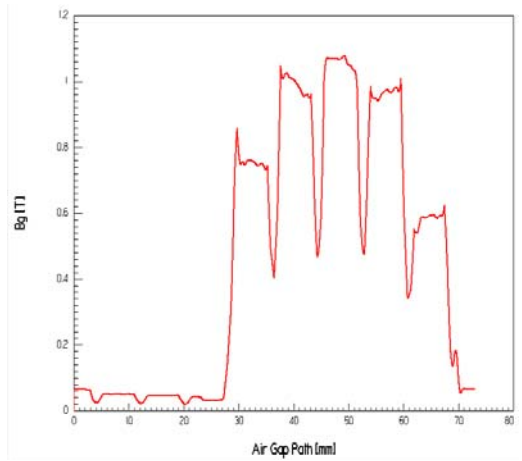
Figure 6. 3 Shows the cross section of the four-pole 2hp interior permanent magnet motor



(a)



(b)



(c)

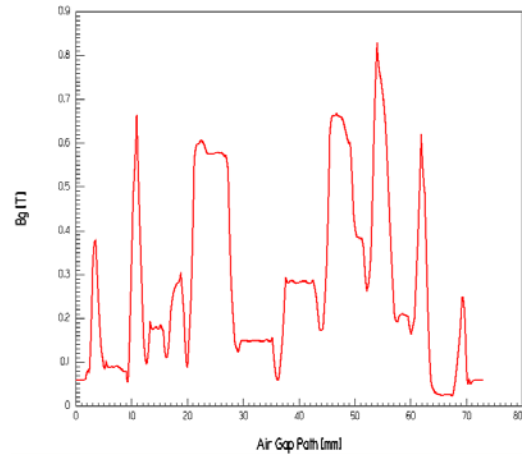


Figure 6. 4(a-c): flux path and air-gap flux density, (b) no-load current, (c) q-axis rated current, (d) d-axis rated current.

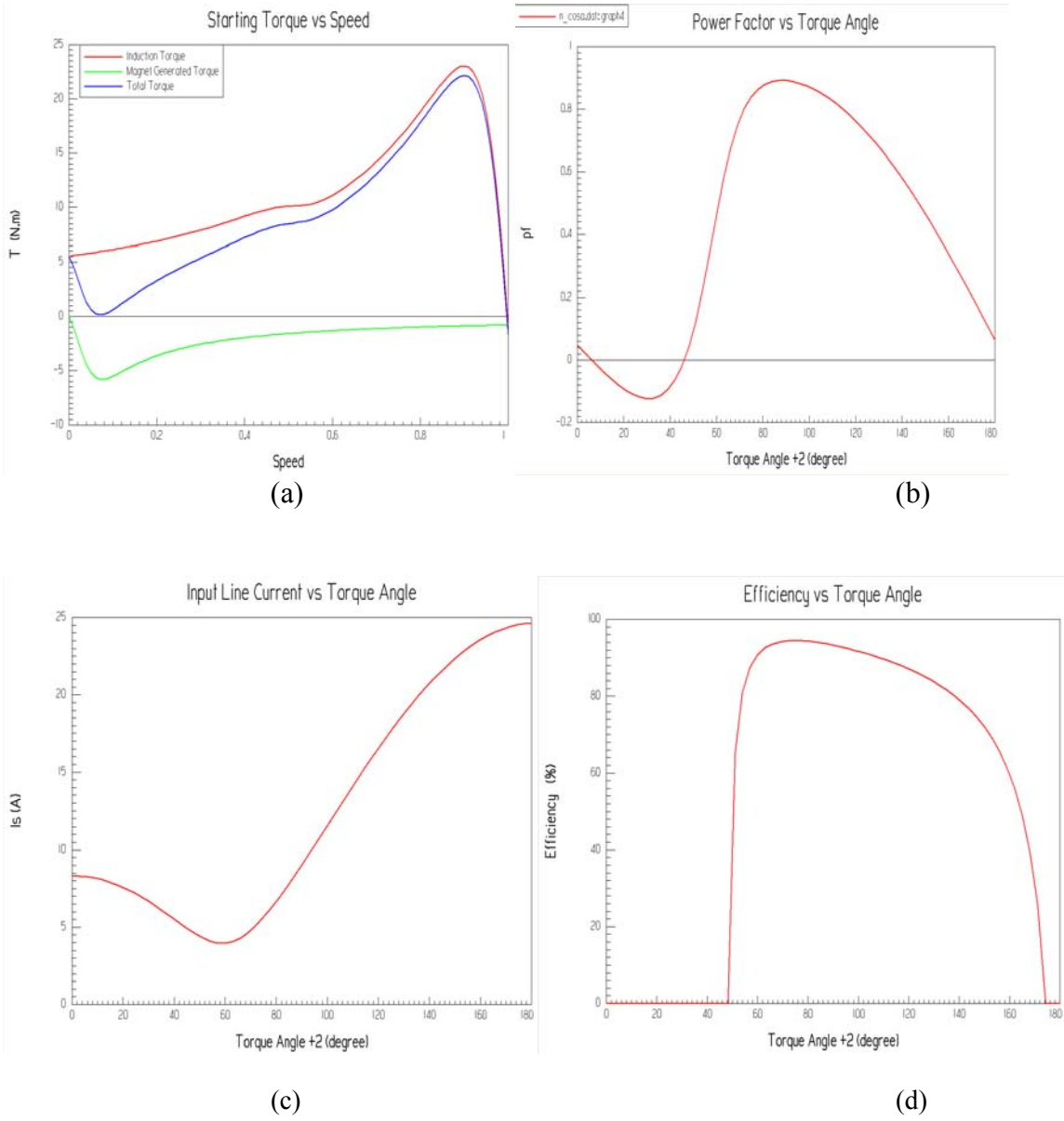


Figure 6. 5: (a) Torque vs. speed, (b) power factor vs. torque angle (c) Input line current vs. torque angle (d) efficiency vs. torque angle

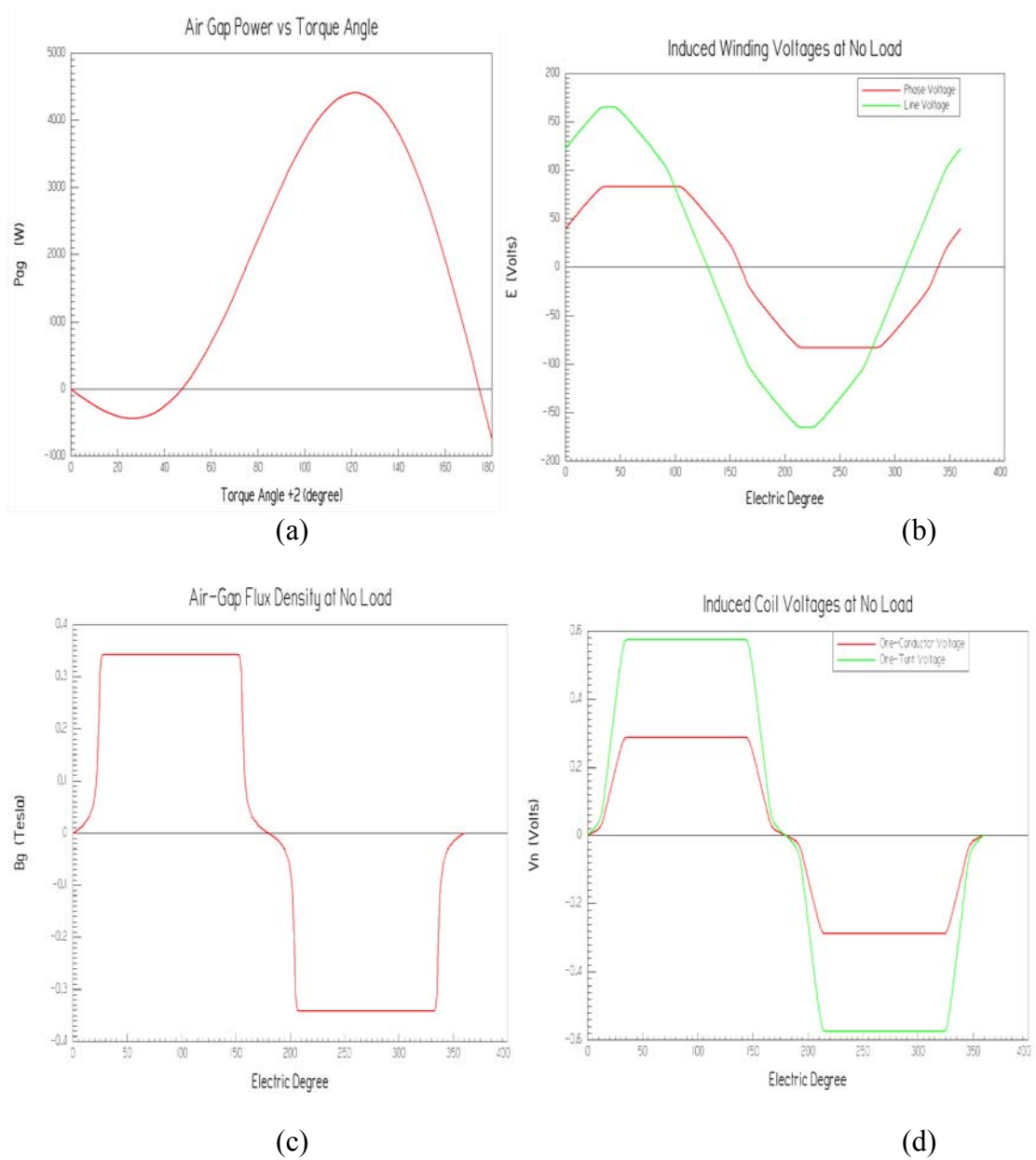


Figure 6. 6: (a) Air gap power vs. torque angle (b) Induced winding voltage at no-load vs. electrical degree (c) Air gap flux density at no-load vs. electric degree (d) Induced coil voltage vs. electric degree

6.3 Determination of Iron Loss Resistance

In steady state condition, the electrical input power P_{in} is the sum of the copper loss P_c and iron loss P_i when the IPMSM is running on no-load condition as given by Equation (6.6):

$$P_{in} = P_c + P_i \quad (6.6)$$

$$P_c = 3I_{ph}^2 R_s \quad (6.7)$$

The iron loss resistance is determined by the following procedure:

- (1) The IPMSM operates at constant speed at no-load condition
- (2) Several input power P_{in} , input voltage V_{rms} , input current $I_{ph}(rms)$, and power factor are measured.
- (3) Using the measurement data by step 2, the iron loss is calculated as

$$P_i = P_{in} - P_c \quad (6.8)$$

- (4) The armature resistance voltage drop is approximately negligible, i.e. $I_{ph}R_s \approx 0$, hence, the voltage across the core loss resistance is given as

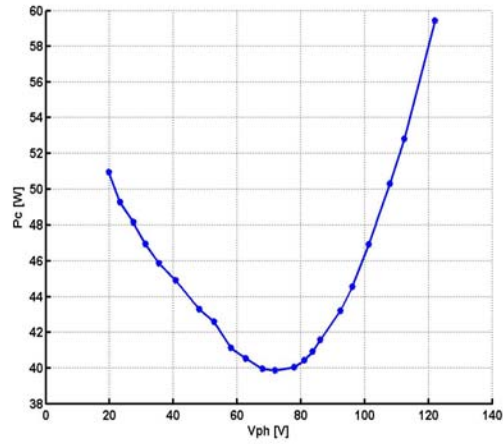
$$V_c \approx V_{ph} \quad (6.9)$$

- (5) The iron loss resistance R_c is straightforwardly calculated from the core loss P_c as follows:

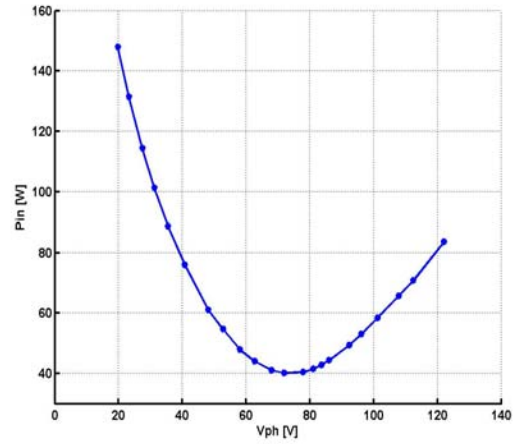
$$R_c = 3V_c^2/P_i \quad (6.10)$$

Figures 6.7(a-d) shows the various plot of the no-load experimental test. Figure 6.7(a) shows the plot of the iron loss, P_i , as it varies with input voltage; Figure 6.7(b)

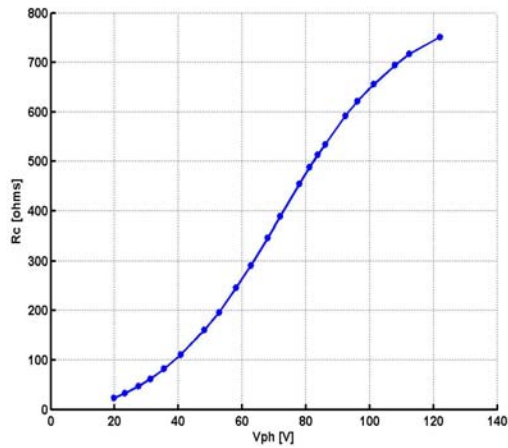
shows the variation of the input power, P_{in} , versus the input voltage; Figure 6.7 (c) shows iron loss resistance against input voltage and Figure 6.7(d) shows the terminal current versus the input voltage.



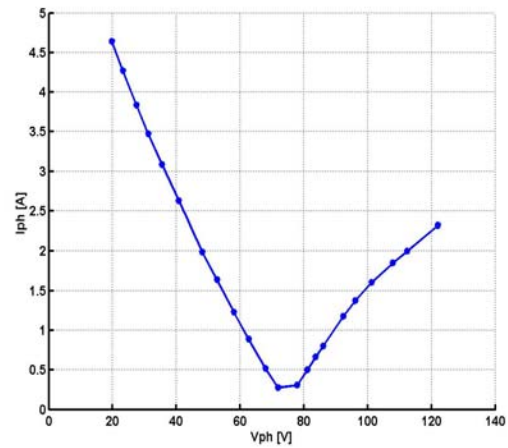
(a)



(b)



(c)



(d)

Figure 6. 7: (a) Iron loss against input voltage (b) Input power against input voltage (c) Iron loss resistance against input voltage (d) Terminal phase current against input voltage.

The iron loss resistance is a function of the terminal input voltage for this operating speed (rated speed). It can be seen that the iron loss has a minimum value as the terminal voltage equals the no-load EMF E_o (minimum stator current or negligible stator current), then it increases again as the input voltage decreases.

6.4 Influence of the Iron Loss and Parameter Variations on the Efficiency of IPMSM

By computation, the influence of the iron losses and parameter variation on the efficiency of the IPMSM is determined for different load conditions at rated speed.

The steady state voltage equation of this model is expressed as

$$V_{cq} = \omega_r \lambda_{ds} = \omega_r L_{ds} I'_{ds} + \omega_r \lambda_m = I_{cq} R_c$$

$$V_{qs} = R_s I_{qs} + V_{cq} \quad (6.11)$$

$$V_{cd} = -\omega_r \lambda_{qs} = -\omega_r L_{qs} I'_{qs} = I_{cd} R_c$$

$$V_{ds} = R_s I_{ds} + V_{cd} \quad (6.12)$$

The electromagnetic torque equation is given by

$$T_e = \frac{3P}{4} [\lambda_{ds} I'_{qs} - \lambda_{qs} I'_{ds}]$$

$$= \frac{3P}{4} [\lambda_m I'_{qs} + (L_{ds} - L_{qs}) I'_{ds} I'_{qs}] \quad (6.13)$$

Note that the magnetizing currents in the IPMSM model can be expressed as follows:

$$I'_s = I'^2_{qs} + I'^2_{ds}$$

$$I_{qs}'^2 = I_s'^2 - I_{ds}'^2 \quad . \quad (6.14)$$

Equation (6.13) can be rewritten as:

$$\left(\frac{4T_e}{3P} \right)^2 = I_{qs}'^2 [\lambda_m + (L_{ds} - L_{qs}) I_{qs}']^2 \quad (6.15)$$

Substitute Equation (6.14) in (6.15) gives the following expression:

$$\left(\frac{4T_e}{3P} \right)^2 = (I_s'^2 - I_{ds}'^2) [\lambda_m + (L_{ds} - L_{qs}) I_{qs}']^2 \quad . \quad (6.16)$$

The following procedure is taken in the computation of the efficiency, total loss, copper loss, and core loss of the IPMSM for different torque generated by the motor considering the influence of parameter variation and iron loss:

- (1) With the assumption that the magnetizing current magnitude is less than the rated current, that is

$$0 \leq I_s' \leq I_{\text{rated}} \quad . \quad (6.17)$$

- (2) Determine the parameters of the motor (L_{qs} , L_{ds} and λ_m) depending on the magnetizing current I_s' .

- (3) For a given torque, solve for I_{ds}' by varying I_s' in Equation (6.16) .

- (4) Determine the value of the q-axis magnetizing current I_{qs}' from Equation (6.14).

- (5) Determine the core loss resistance voltages (V_{cd} and V_{cq}) using Equations (6.11) and (6.12).

- (6) Compute the magnitude of the core loss resistance voltage V_c

$$V_c^2 = V_{cq}^2 + V_{cd}^2 \quad . \quad (6.18)$$

(7) Determine the corresponding core loss resistance by interpolation using Figure 6.7(c).

(8) Determine the iron loss currents using:

$$I_{cq} = \frac{V_{cq}}{R_c}, I_{cd} = \frac{V_{cd}}{R_c} . \quad (6.19)$$

(9) Compute the terminal currents using Equation (6.4).

(10) Compute the total loss of the IPMSM, ignoring frictional and mechanical losses, as follows:

$$P_c = \frac{3}{2} R_s (I_{ds}^2 + I_{qs}^2) \quad (6.20)$$

$$P_i = \frac{3}{2} R_c (I_{cd}^2 + I_{cq}^2) \quad (6.21)$$

$$P_{Loss} = P_c + P_i . \quad (6.22)$$

(11) The efficiency of the IPMSM is given by

$$\eta = \frac{T_e \left(\frac{\omega_r}{2} \right)}{T_e \left(\frac{\omega_r}{2} \right) + P_{Loss}} . \quad (6.23)$$

Figures (6.8) shows the computational result of the influence of the iron losses and parameter variation on the performance of the IPMSM at the rated speed.

The range of operation decreases with increase in load, hence, as the load increases the current demand increases and also the total losses as shown by Figure 6.8 (a).

This computation shows that a high efficiency can be achieved for different load torque by proper selection of the q- and d- axis currents as shown by Figures 6.8 (b) and (d). An

efficiency of above 90% is obtainable up to the rated torque which is possibly due to the consideration of saturation and iron-loss in the computation of the performance of the IPM.

The point of minimum current does not necessarily has to be the most efficient point of operation as shown in Figure 6.8(b). Hence, for a given torque, the proper determination of the d and q axis current with optimize the performance of the machine. Figure 6.8(c) shows that the iron loss becomes approximately constant at a high current for different load, showing that the core loss is independent of the armature current at high values.

Figure 6.9 shows the experimental result for different loads, the result follow similar trends confirming that by operating at the required voltage, better performance based on the efficiency of the system can be attained. The experiment was carried out using the 2hp IPM for two different loads and the procedure for determining the efficiency and performance of the IPM are as follows:

- (1) The IPMSM operates at constant speed.
- (2) Several input power P_{in} , input voltage V_{phrms} , input current $I_{ph}(rms)$, and power factor are measured.
- (3) Compute the voltage across the core loss resistance by :

$$V_c = V_{ph} - I_{ph}R_s . \quad (6.24)$$

- (4) Estimate the core loss resistance from Figure 6.7(c).
- (5) Compute the core loss as

$$P_i = 3V_c^2/R_c . \quad (6.25)$$

(6) Compute the copper loss as

$$P_c = 3I_{ph}^2 R_c \quad . \quad (6.26)$$

(7) Total losses, ignoring the mechanical losses, is therefore given as

$$P_L = P_i + P_c \quad . \quad (6.27)$$

(8) Compute the output power as

$$P_{out} = P_{in} - P_L \quad . \quad (6.28)$$

(9) Determine the efficiency of the motor as

$$\eta = \frac{P_{out}}{P_{in}} 100 \quad . \quad (6.29)$$

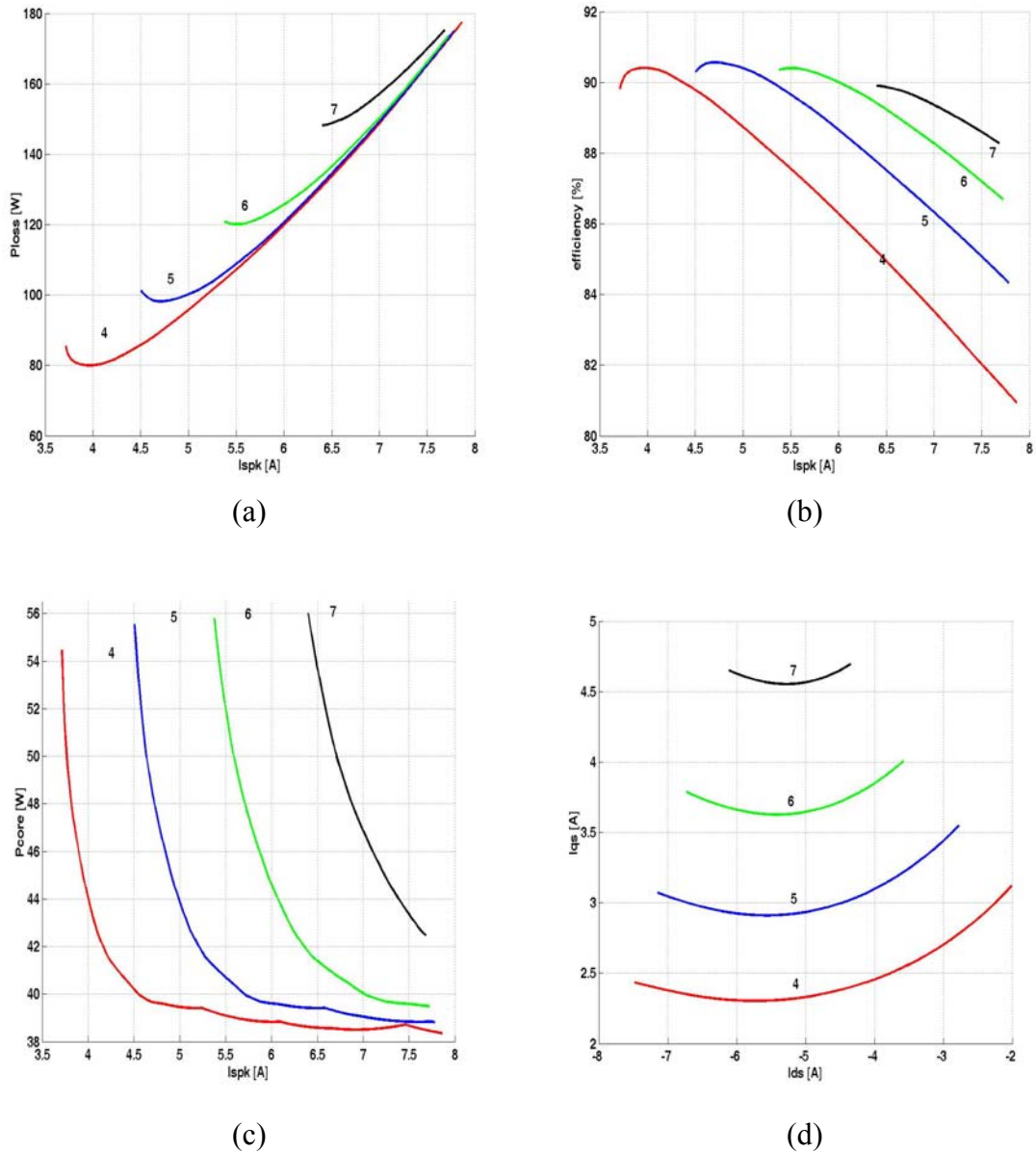
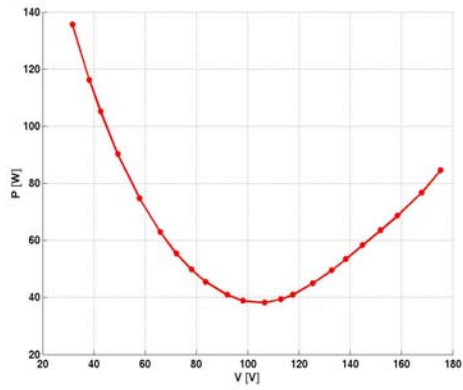
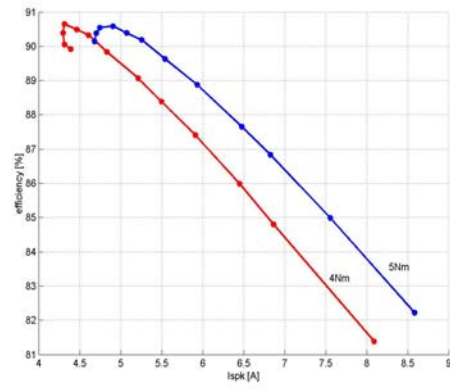


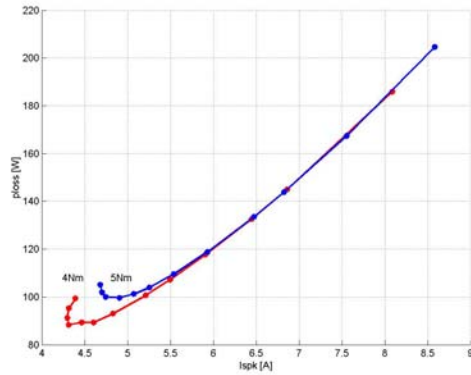
Figure 6. 8: Performance curves of the IPM. (a) Total losses, (b) efficiency (c) core loss (d) q-d current for torque values of 4Nm, 5Nm, 6Nm, and 7Nm for 60 Hz supply frequency.



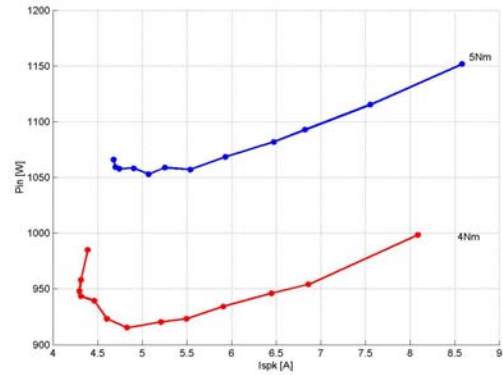
(a)



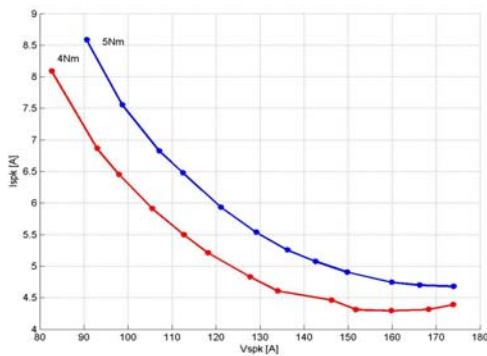
(b)



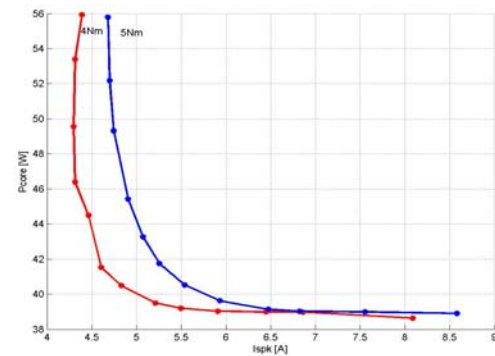
(c)



(d)



(e)



(f)

Figure 6. 9: Measured performance curves of the IPM for supply frequency of 60 Hz. (a) No-load loss against input voltage, (b) efficiency against input current, (c) total loss against input current, (d) Input power against input current (e) input current against input voltage, (d) core losses against input current.

CHAPTER 7
EFFICIENCY OPTIMIZATION OF THE INTERIOR PERMANENT MAGNET
SYNCHRONOUS MACHINE

7.1 Introduction

In the past few years, nonlinear control theory has been used in some electrical machine control systems [48,69,83,84]. The main reason of using nonlinear control techniques is to improve the existing control system and achieve high performance. The principles of nonlinear control input-output linearization with decoupling are used to design the controllers [60,71,80-85]. The literature in [60] has successfully used this control technique to control the torque as well as to reduce the total loss of a synchronous reluctance motor, while literature in [71] has implemented experimentally the torque-per-amp operation using this control technique for a permanent magnet synchronous motor.

The attention in this chapter is focus on the speed control and total loss minimization. The concept of input-output linearization control technique is sets forth in the implementation of the speed control of the interior permanent magnet motor drives which simultaneously ensures the minimization of the losses – the copper and core losses. This control scheme is unique in that saturation dependent parameters such as the d and q axis inductances and the armature reaction dependent magnet flux linkage are included in the controller structure formulation and implementation. The proposed control scheme differs from known schemes which are either based on perturbation and search methods

or on steady curve fitted graphs that map the command q and d axis currents based on reference torque. Unlike these methods, an optimization formulation that dynamically determines the reference currents/voltages required to achieve high performance speed control and total loss minimization is used. The control structure methodology, the nature of the variations of the machine parameters and how they influence the machine efficiency are clearly laid out .

7.2 Interior Permanent Magnet Synchronous Machine (IPMSM) Model including Iron Losses

Figure 7.1 shows the d- and q-axis equivalent circuits in the d-q coordinate, which rotate synchronously with an electrical angular velocity ω_r . The equivalent circuits include the effects of the copper loss and the iron loss. R_s represents the armature copper loss resistance. The iron loss consists of hysteresis loss and eddy current loss, but here they are added into a single quantity and the iron loss is represented by the iron loss resistance R_c inserted in parallel with the armature inductance [33,34,40,67,68,71]. Thus, the d-q axis line currents (I_{ds}, I_{qs}) are divided into iron loss currents (I_{cd}, I_{cq}) and magnetizing currents (I'_{ds}, I'_{qs}) .

From Figure 7.1, the voltage equations of the interior permanent magnet synchronous motor is expressed as

$$V_{qs} = R_s I_{qs} + V_{cq}$$

$$V_{ds} = R_s I_{ds} + V_{cd} \quad (7.1)$$

$$V_{cq} = L_{qs} p I'_{qs} + \omega_r \lambda_{ds} = I_{cq} R_c$$

$$V_{cd} = L_{ds} p I'_{ds} - \omega_r \lambda_{qs} = I_{cd} R_c \quad (7.2)$$

where

$$I_{cq} = \frac{V_{qs} - R_s I_{qs}}{R_c} = \frac{L_{qs} p I'_{qs} + \omega_r \lambda_{ds}}{R_c}$$

$$I_{cd} = \frac{V_{ds} - R_s I_{ds}}{R_c} = \frac{L_{ds} p I'_{ds} - \omega_r \lambda_{qs}}{R_c} \quad (7.3)$$

$$I_{qs} = I'_{qs} + I_{cq}, \quad I_{ds} = I'_{ds} + I_{cd} \quad (7.4)$$

$$\lambda_{ds} = L_{ds} I'_{ds} + \lambda_m, \quad \lambda_{qs} = L_{qs} I'_{qs} \quad (7.5)$$

where V_{ds} and V_{qs} are the d- and q-axis components of the terminal voltage, L_{ds} and L_{qs} are the d- and q-axis components of armature self-inductance, λ_{ds} and λ_{qs} are the d- and q-axis components of the flux linkage, λ_m is the magnet flux linkage, and p is differential operator define as $\frac{d}{dt}$.

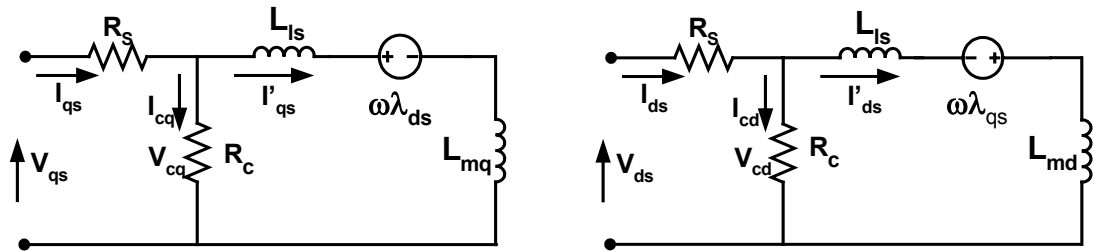


Figure 7.1: Electric equivalent circuit model of an Interior Permanent Magnet Synchronous Motor (IPMSM) with core-loss included.

Expressing the terminal voltage equations in terms of the magnetizing currents rather than terminal currents, hence substituting Equations (7.2)-(7.5) in Equation (7.1) gives

$$\begin{aligned} V_{qs} &= R_s I'_{qs} + L_{qs} pI'_{qs} \left(1 + \frac{R_s}{R_c}\right) + \omega_r \lambda_{ds} \left(1 + \frac{R_s}{R_c}\right) \\ V_{ds} &= R_s I'_{ds} + L_{ds} pI'_{ds} \left(1 + \frac{R_s}{R_c}\right) - \omega_r \lambda_{qs} \left(1 + \frac{R_s}{R_c}\right). \end{aligned} \quad (7.6)$$

By choosing d- and q-axes magnetizing currents as the state variable, the Interior permanent magnet synchronous motor model given by Equation (7.6) can be written in the following explicit form:

$$\begin{aligned} pI'_{qs} = \sigma_{qs} &= \frac{V_{qs}}{L_{qss}} - \frac{R_s I'_{qs}}{L_{qss}} - \frac{\omega_r L_{ds}}{L_{qs}} I'_{ds} - \frac{\omega_r \lambda_m}{L_{qs}}, \quad L_{qss} = L_{qs} \left(1 + \frac{R_s}{R_c}\right) \\ pI'_{ds} = \sigma_{ds} &= \frac{V_{ds}}{L_{dss}} - \frac{R_s I'_{ds}}{L_{dss}} + \frac{\omega_r L_{qs}}{L_{ds}} I'_{qs}, \quad L_{dss} = L_{ds} \left(1 + \frac{R_s}{R_c}\right). \end{aligned} \quad (7.7)$$

From the equivalent circuit, the electromagnetic torque T_e is proportional to the vector product of flux linkages and currents and can be obtained as (7.8), where P denotes the number of poles. Since R_c supplies an additional current path to each axis equivalent circuit, the torque depends not on measured terminal currents, I_{ds} and I_{qs} , but on the magnetizing currents, I'_{ds} and I'_{qs} . Therefore, the terminal currents can no longer directly govern the torque; hence, the electromagnetic torque equation is given by

$$\begin{aligned} T_e &= \frac{3P}{4} [\lambda_{ds} I'_{qs} - \lambda_{qs} I'_{ds}] \\ &= \frac{3P}{4} [\lambda_m I'_{qs} + (L_{ds} - L_{qs}) I'_{ds} I'_{qs}]. \end{aligned} \quad (7.8)$$

The equation for the motor dynamics are given by

$$p\delta = \omega_e - \omega_r \quad (7.9)$$

$$J\left(\frac{2}{P}\right)p\omega_r = T_e - T_L \quad (7.10)$$

where δ is the rotor position, ω_e is the inverter frequency, J is the motor inertia, and T_L is the load torque.

The state variables of the nonlinear dynamic model for the IPMSM considering iron losses have been chosen as the magnetizing currents, I'_{ds} and I'_{qs} , the rotor speed, ω_r and rotor angle, δ .

Note that the interaction among the d- and q-axes torque currents and the IPMSM angular speed are modeled, and the whole system is nonlinear and coupled.

7.3 Steady State Conditions

The development of voltage equations that express the transient behavior of the interior permanent magnet synchronous motors including the stator iron loss is the first object presented in this thesis, but the appropriate approximations for development are necessary. In order to understand the nature of equivalent circuit parameters and to get parameter approximations in the transient condition, voltage equations in the steady state are developed.

From the model Equations (7.1)-(7.7), each current is constant under steady state conditions. Accordingly, substituting zero into the differential operator p , the magnetizing currents can be written as

$$\begin{bmatrix} I'_{qs} \\ I'_{ds} \end{bmatrix} = \frac{1}{R_c^2 + \omega_r^2 L_{qs} L_{ds}} \left(\begin{bmatrix} R_c^2 & -\omega_r L_{ds} R_c \\ \omega_r L_{qs} R_c & R_c^2 \end{bmatrix} \begin{bmatrix} I_{qs} \\ I_{ds} \end{bmatrix} - \begin{bmatrix} \omega_r \lambda_m R_c \\ \omega_r^2 \lambda_m L_{qs} \end{bmatrix} \right) \quad (7.11)$$

As shown in Equation (7.11), the value of R_c approaching infinity makes I'_{ds} and I'_{qs} identical to I_{ds} and I_{qs} , regardless of the rotational speed ω_r . The magnetizing currents, I'_{ds} and I'_{qs} , are calculated or estimated from the measurable terminal d- and q-axis components of the armature current.

Similarly, the d- and q-axis components of the iron loss current can be express in steady state as follows:

$$\begin{aligned} I_{cq} &= \frac{V_{qs} - R_s I_{qs}}{R_c} = \frac{\omega_r \lambda_{ds}}{R_c} = \frac{\omega_r L_{ds} I'_{ds} + \omega_r \lambda_m}{R_c} \\ I_{cd} &= \frac{V_{ds} - R_s I_{ds}}{R_c} = \frac{-\omega_r \lambda_{qs}}{R_c} = \frac{-\omega_r L_{qs} I'_{qs}}{R_c} \end{aligned} \quad (7.12)$$

7.4 Power Losses of the IPMSM

The copper losses P_c and iron losses P_i of the IPMSM can be calculated as given by Equations (7.13) and (7.14), respectively:

$$P_c = \frac{3}{2} R_s (I_{ds}^2 + I_{qs}^2) \quad (7.13)$$

$$P_i = \frac{3}{2} R_c (I_{cd}^2 + I_{cq}^2). \quad (7.14)$$

Substituting Equation (7.12) in (7.4), the copper losses P_c can be written as

$$\begin{aligned} P_c = & \left(\frac{3}{2}\right) R_s (I_{qs}'^2 + I_{ds}'^2) + \left(\frac{3}{2}\right) \frac{\omega_r^2}{R_c^2} R_s (L_{ds}^2 I_{ds}'^2 + L_{qs}^2 I_{qs}'^2) + \left(\frac{3}{2}\right) \frac{\omega_r^2 \lambda_m^2}{R_c^2} R_s \\ & + 3\omega_r I_{qs}' I_{ds}' \frac{R_s}{R_c} (L_{ds} - L_{qs}) + 3\omega_r \lambda_m I_{qs}' \frac{R_s}{R_c} + 3\omega_r^2 L_{ds} \lambda_m I_{ds}' \frac{R_s}{R_c^2} \end{aligned} \quad (7.15)$$

Substituting Equation (7.12) in (7.14), the iron losses P_i can be written as

$$P_i = \left(\frac{3}{2}\right) \frac{\omega_r^2}{R_c} (L_{ds}^2 I_{ds}'^2 + L_{qs}^2 I_{qs}'^2) + \left(\frac{3}{2}\right) \frac{\omega_r^2 \lambda_m^2}{R_c} + \frac{3\omega_r^2 L_{ds} \lambda_m I_{ds}'}{R_c} \quad (7.16)$$

Thus, the total power losses of the IPMSM, P_L , can be expressed as

$$\begin{aligned} P_L = & \left(\frac{3}{2}\right) R_s (I_{qs}'^2 + I_{ds}'^2) + \left(\frac{3}{2}\right) \frac{\omega_r^2}{R_c^2} (R_s + R_c) (L_{ds}^2 I_{ds}'^2 + L_{qs}^2 I_{qs}'^2) + \left(\frac{3}{2}\right) \frac{\omega_r^2 \lambda_m^2}{R_c^2} (R_s + R_c) \\ & + 3\omega_r I_{qs}' I_{ds}' \frac{R_s}{R_c} (L_{ds} - L_{qs}) + 3\omega_r \lambda_m I_{qs}' \frac{R_s}{R_c} + 3\omega_r^2 L_{ds} \lambda_m I_{ds}' \frac{(R_s + R_c)}{R_c^2} \end{aligned} \quad (7.17)$$

7.5 Input-Output Feedback Linearization Control and Speed Controller Design

The design based on exact linearization consist of two steps: In the first step, a nonlinear compensation which cancels the nonlinearities included in the IPM (as shown in Equations (7.6) through (7.10)) is implemented as an inner feedback loop. In the second step, a controller which ensures stability and some predefined performance is designed based on conventional linear theory, and this linear controller is implemented as an outer feedback loop [88].

Consider a nonlinear system:

$$\begin{aligned}\dot{x} &= f(x) + g(x)u \\ y &= h(x)\end{aligned}\tag{7.18}$$

where $x \in R^n$, $u \in R^m$, and $y \in R^p$ are the state, input, and output (controllable variables) vectors, respectively. $f: R^n \times R^m \rightarrow R^n$, and $h: R^n \rightarrow R^p$ are smooth maps, and $f(x, \cdot)$ is a smooth vector field at R^n for any constant input.

Using the conventional notation, where the Lie derivative of h along the vector field f is defined as

$$L_f \phi(\cdot) = \sum_{i=1}^n \frac{\partial \phi}{\partial x_i} f_i(\cdot),\tag{7.19}$$

for the Lie derivative of the analytical function $\phi: R^n \rightarrow R$ along the vector field $f = [f_1, f_2, \dots, f_n]^T$ and

$$L_f^k \phi(\cdot) = \frac{\partial (L_f^{k-1} \phi)}{\partial x} f(\cdot), \quad k > 1,\tag{7.20}$$

for k-tuple application of the Lie derivative operator L_f .

Taking the time derivatives of these outputs, respectively, until inputs $u_i, i = 1, 2$, appear in the derivative expressions of each output variable are as follows:

$$\begin{aligned}\begin{bmatrix} \dot{y}_1 \\ \dot{y}_2 \end{bmatrix} &= \begin{bmatrix} L_f y_1 \\ L_f y_2 \end{bmatrix} + \begin{bmatrix} L_{g1} y_1 & L_{g2} y_1 \\ L_{g1} y_2 & L_{g2} y_2 \end{bmatrix} \begin{bmatrix} u_1 \\ u_2 \end{bmatrix} \\ &= \begin{bmatrix} L_f y_1 \\ L_f y_2 \end{bmatrix} + E(x)u\end{aligned}\tag{7.21}$$

where $L_f y_i$, $i = 1, 2$, is the Lie derivative of y_i with respect to f . where, $E(x)$ is the decoupling matrix and it is required to be found nonsingular over all operating regions; hence the input-output feedback linearization and the decoupling control law can be selected as follows:

$$u = E^{-1} \begin{bmatrix} v_1 - L_f h_1 \\ v_2 - L_f h_2 \end{bmatrix} \quad (7.22)$$

By the input-output feedback linearization control, the original nonlinear and coupled IPM system can be transformed to an exact linear and decoupled closed-loop system with each pole at the origin of the transformed state space as

$$\begin{aligned} \dot{y}_1 &= v_1 \\ \dot{y}_2 &= v_2 \end{aligned} \quad (7.23)$$

In the dynamic system given in Equations (7.6) through (7.17), the system possesses two independent inputs (V_{qs} and V_{ds}); hence, two independent objectives can be achieved for the control of the machine. One objective is the rotor speed control, ω_r , and the other is the reduction of the total losses, P_L , subject to command torque, $T_e = T_L$, while maximizing along the way the conversion of the electrical energy (limited by the maximal values of the voltages and currents delivered by the inverter feeding the motor) to mechanical energy.

Hence, the outputs are then

$$J \left(\frac{2}{P} \right) p \omega_r = T_e - T_L = \frac{3P}{4} [\lambda_m I'_{qs} + (L_{ds} - L_{qs}) I'_{ds} I'_{qs}] - T_L \quad (7.24)$$

$$\begin{aligned}
P_L &= \left(\frac{3}{2}\right)R_s(I'_{qs}{}^2 + I'_{ds}{}^2) + \left(\frac{3}{2}\right)\frac{\omega_r^2}{R_c^2}(R_s + R_c)(L_{ds}^2 I'_{ds}{}^2 + L_{qs}^2 I'_{qs}{}^2) + \left(\frac{3}{2}\right)\frac{\omega_r^2 \lambda_m^2}{R_c^2}(R_s + R_c) \\
&\quad + 3\omega_r I'_{qs} I'_{ds} \frac{R_s}{R_c}(L_{ds} - L_{qs}) + 3\omega_r \lambda_m I'_{qs} \frac{R_s}{R_c} + 3\omega_r^2 L_{ds} \lambda_m I'_{ds} \frac{(R_s + R_c)}{R_c^2} \\
&= \left(\frac{3}{2}\right)R_s(I'_{qs}{}^2 + I'_{ds}{}^2) + \left(\frac{3}{2}\right)(L_{ds}^2 I'_{ds}{}^2 + L_{qs}^2 I'_{qs}{}^2) \frac{\omega_r^2}{R_c} \left(1 + \frac{R_s}{R_c}\right) + \left(\frac{3}{2}\right)\frac{\omega_r^2 \lambda_m^2}{R_c} \left(1 + \frac{R_s}{R_c}\right) \\
&\quad + 3\omega_r I'_{qs} I'_{ds} \frac{R_s}{R_c}(L_{ds} - L_{qs}) + 3\omega_r \lambda_m I'_{qs} \frac{R_s}{R_c} + 3\omega_r^2 L_{ds} I'_{ds} \frac{\lambda_m}{R_c} \left(1 + \frac{R_s}{R_c}\right) . \tag{7.25}
\end{aligned}$$

In order to optimized the total losses (copper losses and iron losses) for any given constant torque, another constraints which is the total differential of the total losses along a constant torque trajectory is therefore proposed [60, 19]; hence, defining

$$\gamma = \begin{vmatrix} \frac{\partial P_L}{\partial I'_{qs}} & \frac{\partial P_L}{\partial I'_{ds}} \\ \frac{\partial T_e}{\partial I'_{qs}} & \frac{\partial T_e}{\partial I'_{ds}} \end{vmatrix} = 0 \tag{7.26}$$

The new outputs for the system are now $p\omega_r$ and γ . The objective of the nonlinear controller is to force the output (γ) to zero, so that the reached operating point corresponds to an extremum of P_L along a constant torque trajectory.

Executing the minimization/optimization Equation (7.26), the following partial derivatives are obtained as follows.

Differentiating Equation (7.25) with respect to I'_{qs} gives

$$\begin{aligned}
\frac{\partial P_L}{\partial I'_{qs}} &= 3R_s I'_{qs} + 3\frac{\omega_r^2}{R_c^2}(R_s + R_c)L_{qs}^2 I'_{qs} + 3\omega_r I'_{ds} \frac{R_s}{R_c}(L_{ds} - L_{qs}) + 3\omega_r \lambda_m \frac{R_s}{R_c} \\
&= 3R_s I'_{qs} + 3\frac{\omega_r^2}{R_c} \left(1 + \frac{R_s}{R_c}\right) L_{qs}^2 I'_{qs} + 3\omega_r I'_{ds} \frac{R_s}{R_c}(L_{ds} - L_{qs}) + 3\omega_r \lambda_m \frac{R_s}{R_c} . \tag{7.27}
\end{aligned}$$

Differentiating Equation (7.25) with respect to I'_{ds} gives

$$\begin{aligned} \frac{\partial P_L}{\partial I'_{ds}} &= 3R_s I'_{ds} + 3 \frac{\omega_r^2}{R_c^2} (R_s + R_c) L_{ds}^2 I'_{ds} + 3\omega_r I'_{qs} \frac{R_s}{R_c} (L_{ds} - L_{qs}) + 3\omega_r^2 L_{ds} \lambda_m \frac{(R_s + R_c)}{R_c^2} \\ &= 3R_s I'_{ds} + 3 \frac{\omega_r^2}{R_c} \left(1 + \frac{R_s}{R_c}\right) L_{ds}^2 I'_{ds} + 3\omega_r I'_{qs} \frac{R_s}{R_c} (L_{ds} - L_{qs}) + 3\omega_r^2 L_{ds} \frac{\lambda_m}{R_c} \left(1 + \frac{R_s}{R_c}\right). \end{aligned} \quad (7.28)$$

Differentiating Equation (7.24) with respect to I'_{qs} gives

$$\frac{\partial T_e}{\partial I'_{qs}} = \frac{3P}{4} \left[\lambda_m + (L_{ds} - L_{qs}) I'_{ds} \right]. \quad (7.29)$$

Differentiating Equation (7.24) with respect to I'_{ds} gives

$$\frac{\partial T_e}{\partial I'_{ds}} = \frac{3P}{4} (L_{ds} - L_{qs}) I'_{qs}. \quad (7.30)$$

Substituting Equations (7.27)-(7.30) in Equation (7.26) gives

$$\gamma = \frac{9P}{4} \left[\begin{aligned} &R_s (L_{ds} - L_{qs}) (I_{qs}'^2 - I_{ds}'^2) + \omega_r^2 L_{ds} L_{qs} I'_{ds} \frac{\lambda_m}{R_c} \left(1 + \frac{R_s}{R_c}\right) - \omega_r^2 L_{ds} \frac{\lambda_m^2}{R_c} \left(1 + \frac{R_s}{R_c}\right) \\ &+ \omega_r^2 L_{ds}^2 L_{qs} I_{ds}'^2 \frac{1}{R_c} \left(1 + \frac{R_s}{R_c}\right) - 2\omega_r^2 L_{ds}^2 \lambda_m I'_{ds} \frac{1}{R_c} \left(1 + \frac{R_s}{R_c}\right) - R_s \lambda_m I'_{ds} \\ &- \omega_r^2 L_{qs}^3 I_{qs}'^2 \frac{1}{R_c} \left(1 + \frac{R_s}{R_c}\right) + \omega_r^2 L_{qs}^2 L_{ds} I_{qs}'^2 \frac{1}{R_c} \left(1 + \frac{R_s}{R_c}\right) - \omega_r^2 L_{ds}^3 I_{ds}'^2 \frac{1}{R_c} \left(1 + \frac{R_s}{R_c}\right) \end{aligned} \right]. \quad (7.31)$$

Applying the input-output linearization techniques to the system, by taking the time derivatives of these outputs ($p\omega_r$ and γ), the original nonlinear and coupled IPMSM system can be transformed to an exact linear and decoupled closed-loop system.

Differentiating Equation (7.24) with respect to time gives

$$\left(\frac{8J}{3P^2} \right) p^2 \omega_r = \frac{dT_e}{dt} = pI'_{qs} \left[\lambda_m + (L_{ds} - L_{qs}) I'_{ds} \right] + pI'_{ds} (L_{ds} - L_{qs}) I'_{qs} = \sigma_w$$

$$\sigma_w = \left(\frac{8J}{3P^2} \right) p^2 \omega_r = \frac{dT_e}{dt} = a_{11} p I'_{qs} + a_{12} p I'_{ds} . \quad (7.32)$$

Differentiating Equation (7.31) with respect to time gives

$$\frac{d\gamma}{dt} = \frac{9P}{4} \left[\begin{aligned} & 2R_s(L_{ds} - L_{qs}) (I'_{qs} p I'_{qs} - I'_{ds} p I'_{ds}) + \omega_r^2 L_{ds} L_{qs} p I'_{ds} \frac{\lambda_m}{R_c} \left(1 + \frac{R_s}{R_c} \right) \\ & + 2\omega_r^2 L_{ds}^2 L_{qs} I'_{ds} p I'_{ds} \frac{1}{R_c} \left(1 + \frac{R_s}{R_c} \right) - 2\omega_r^2 L_{ds}^2 \lambda_m p I'_{ds} \frac{1}{R_c} \left(1 + \frac{R_s}{R_c} \right) \\ & - 2\omega_r^2 L_{qs}^3 I'_{qs} p I'_{qs} \frac{1}{R_c} \left(1 + \frac{R_s}{R_c} \right) + 2\omega_r^2 L_{qs}^2 L_{ds} I'_{qs} p I'_{qs} \frac{1}{R_c} \left(1 + \frac{R_s}{R_c} \right) \\ & - 2\omega_r^2 L_{ds}^3 I'_{ds} p I'_{ds} \frac{1}{R_c} \left(1 + \frac{R_s}{R_c} \right) - R_s \lambda_m p I'_{ds} \end{aligned} \right] \quad (7.33)$$

$$\sigma_\gamma = \frac{d\gamma}{dt} = a_{21} p I'_{qs} + a_{22} p I'_{ds}$$

where

$$a_{11} = \lambda_m + (L_{ds} - L_{qs}) I'_{ds}, \quad a_{12} = (L_{ds} - L_{qs}) I'_{qs}$$

$$a_{21} = \frac{9P}{4} \left[2R_s(L_{ds} - L_{qs}) I'_{qs} - 2\omega_r^2 L_{qs}^3 I'_{qs} \frac{1}{R_c} \left(1 + \frac{R_s}{R_c} \right) + 2\omega_r^2 L_{qs}^2 L_{ds} I'_{qs} \frac{1}{R_c} \left(1 + \frac{R_s}{R_c} \right) \right]$$

$$a_{22} = \frac{9P}{4} \left[\begin{aligned} & -2R_s(L_{ds} - L_{qs}) I'_{ds} + \omega_r^2 L_{ds} L_{qs} \frac{\lambda_m}{R_c} \left(1 + \frac{R_s}{R_c} \right) \\ & + 2\omega_r^2 L_{ds}^2 L_{qs} I'_{ds} \frac{1}{R_c} \left(1 + \frac{R_s}{R_c} \right) - 2\omega_r^2 L_{ds}^2 \lambda_m \frac{1}{R_c} \left(1 + \frac{R_s}{R_c} \right) \\ & - 2\omega_r^2 L_{ds}^3 I'_{ds} \frac{1}{R_c} \left(1 + \frac{R_s}{R_c} \right) - R_s \lambda_m \end{aligned} \right] \quad (7.34)$$

Solving Equations (7.32) and (7.33) for $p I'_{qs}$ and $p I'_{ds}$, the following expression are obtained:

$$p I'_{qs} = \frac{(a_{22} \sigma_\omega - a_{12} \sigma_\gamma)}{\Delta} = \sigma_{qs} \quad (7.35)$$

$$pI'_{qs} = \frac{(a_{22}\sigma_\omega - a_{12}\sigma_\gamma)}{\Delta} = \sigma_{qs} \quad (7.36)$$

where

$$\Delta = a_{11}a_{22} - a_{21}a_{12}$$

$$\Delta = \frac{9P}{4} \begin{bmatrix} -3R_s \lambda_m L_{dq} I'_{ds} + 2\omega_r^2 L_{ds}^2 R_{cc} (L_{qs} \lambda_m I'_{ds} - \lambda_m^2 - L_{ds} \lambda_m I'_{ds}) \\ + \omega_r^2 L_{dq} R_{cc} (2L_{qs}^3 I_{qs}'^2 - 2L_{qs}^2 L_{ds} I_{qs}'^2 + L_{ds} L_{qs} \lambda_m I'_{ds} + 2L_{ds}^2 L_{qs} I_{ds}'^2 \\ - 2L_{ds}^2 \lambda_m I'_{ds} - 2L_{ds}^3 I_{ds}'^2) - 2L_{dq}^2 R_s (I_{qs}'^2 + I_{ds}'^2) - R_s \lambda_m^2 + \omega_r^2 L_{ds} L_{qs} \lambda_m^2 R_{cc} \end{bmatrix} \quad (7.37)$$

where

$$R_{cc} = \frac{1}{R_c} \left(1 + \frac{R_s}{R_c} \right), \quad L_{dq} = L_{ds} - L_{qs} \quad (7.38)$$

If Equations (7.35-7.36) are to be viable, the determinant Δ must not be identically equal to zero. Non-singularity of Δ is maintained for all motor operability region which is ensured especially when the stator and/or core loss resistances are included in the model.

Hence, the voltage equations can be written as

$$V_{qs} = L_{qss}(\sigma_{qs} + R_s I'_{qs}/L_{qss} + w_r L_{ds} I'_{ds}/L_{qs} + w_r \lambda_m/L_{qs})$$

$$V_{ds} = L_{dss}(\sigma_{ds} + R_s I'_{ds}/L_{dss} - w_r L_{qs} I'_{qs}/L_{ds}) \quad (7.39)$$

As R_c becomes infinity, Equation (7.31) becomes minimization of copper loss, which can also be referred to as torque/ampere, since the core loss component of Equation (7.25) becomes negligible. Hence, Equations (7.35) and (7.36) can be expressed as

$$pI_{qs} = \frac{(a_{22}\sigma_\omega - a_{12}\sigma_\gamma)}{\Delta} = \sigma_{qs} \quad (7.40)$$

$$pI_{ds} = \frac{(a_{11}\sigma_\gamma - a_{21}\sigma_\omega)}{\Delta} = \sigma_{ds} \quad (7.41)$$

where

$$\begin{aligned} \Delta &= a_{11}a_{22} - a_{21}a_{12} \\ a_{11} &= \lambda_m + (L_{ds} - L_{qs})I_{ds}, \quad a_{12} = (L_{ds} - L_{qs})I_{qs}, \\ a_{21} &= \frac{9P}{2} R_s (L_{ds} - L_{qs})I_{qs} \\ a_{22} &= \frac{9P}{4} [-2R_s (L_{ds} - L_{qs})I'_{ds} - R_s \lambda_m]. \end{aligned}$$

The q-d command voltages required to achieve the control can be expressed as

$$\begin{aligned} V_{qs} &= R_s I_{qs} + L_{qs} \sigma_{qs} + \omega_r \lambda_{ds} \\ V_{ds} &= R_s I_{ds} + L_{ds} \sigma_{ds} - \omega_r \lambda_{qs}. \end{aligned} \quad (7.45)$$

7.6 Input-Output Feedback Linearization Control and Torque Controller Design

Following the procedure for the input-output linearization techniques laid out above for speed control, in this case, the outputs are the electromagnetic torque and total loss minimization, then similar equations from Equations (7.24) through (7.45) can be obtained.

Defining the torque equation as

$$T_e - T_L = \frac{3P}{4} [\lambda_m I'_{qs} + (L_{ds} - L_{qs}) I'_{ds} I'_{qs}] - T_L. \quad (7.46)$$

Rewritten the optimization Equation (7.31):

$$\gamma = \frac{9P}{4} \left[\begin{array}{l} R_s (L_{ds} - L_{qs}) (I_{qs}'^2 - I_{ds}'^2) + \omega_r^2 L_{ds} L_{qs} I_{ds}' \frac{\lambda_m}{R_c} \left(1 + \frac{R_s}{R_c}\right) - \omega_r^2 L_{ds} \frac{\lambda_m^2}{R_c} \left(1 + \frac{R_s}{R_c}\right) \\ + \omega_r^2 L_{ds}^2 L_{qs} I_{ds}'^2 \frac{1}{R_c} \left(1 + \frac{R_s}{R_c}\right) - 2\omega_r^2 L_{ds}^2 \lambda_m I_{ds}' \frac{1}{R_c} \left(1 + \frac{R_s}{R_c}\right) - R_s \lambda_m I_{ds}' \\ - \omega_r^2 L_{qs}^3 I_{qs}'^2 \frac{1}{R_c} \left(1 + \frac{R_s}{R_c}\right) + \omega_r^2 L_{qs}^2 L_{ds} I_{qs}'^2 \frac{1}{R_c} \left(1 + \frac{R_s}{R_c}\right) - \omega_r^2 L_{ds}^3 I_{ds}'^2 \frac{1}{R_c} \left(1 + \frac{R_s}{R_c}\right) \end{array} \right] \quad (7.47)$$

Applying the input-output linearization techniques to the system, by taking the time derivatives of these outputs (T_e and γ), the original nonlinear and coupled IPMSM system can be transformed to an exact linear and decoupled closed-loop system.

Differentiating Equation (7.46) with respect to time gives

$$\sigma_{T_e} = \frac{dT_e}{dt} = \frac{3P}{4} [a_{11} pI_{qs}' + a_{12} pI_{ds}'] \quad (7.48)$$

Differentiating Equation (7.47) with respect to time gives

$$\frac{d\gamma}{dt} = \frac{9P}{4} \left[\begin{array}{l} 2R_s (L_{ds} - L_{qs}) (I_{qs}' pI_{qs}' - I_{ds}' pI_{ds}') + \omega_r^2 L_{ds} L_{qs} pI_{ds}' \frac{\lambda_m}{R_c} \left(1 + \frac{R_s}{R_c}\right) \\ + 2\omega_r^2 L_{ds}^2 L_{qs} I_{ds}' pI_{ds}' \frac{1}{R_c} \left(1 + \frac{R_s}{R_c}\right) - 2\omega_r^2 L_{ds}^2 \lambda_m pI_{ds}' \frac{1}{R_c} \left(1 + \frac{R_s}{R_c}\right) \\ - 2\omega_r^2 L_{qs}^3 I_{qs}' pI_{qs}' \frac{1}{R_c} \left(1 + \frac{R_s}{R_c}\right) + 2\omega_r^2 L_{qs}^2 L_{ds} I_{qs}' pI_{qs}' \frac{1}{R_c} \left(1 + \frac{R_s}{R_c}\right) \\ - 2\omega_r^2 L_{ds}^3 I_{ds}' pI_{ds}' \frac{1}{R_c} \left(1 + \frac{R_s}{R_c}\right) - R_s \lambda_m pI_{ds}' \end{array} \right] \quad (7.49)$$

$$\sigma_\gamma = \frac{d\gamma}{dt} = a_{21} pI_{qs}' + a_{22} pI_{ds}' \quad (7.50)$$

where

$$a_{11} = \frac{3P}{4} [\lambda_m + (L_{ds} - L_{qs}) I_{ds}'], \quad a_{12} = \frac{3P}{4} (L_{ds} - L_{qs}) I_{qs}'$$

$$\begin{aligned}
a_{21} &= \frac{9P}{4} \left[2R_s (L_{ds} - L_{qs}) I'_{qs} - 2\omega_r^2 L_{qs}^3 I'_{qs} \frac{1}{R_c} \left(1 + \frac{R_s}{R_c} \right) + 2\omega_r^2 L_{qs}^2 L_{ds} I'_{qs} \frac{1}{R_c} \left(1 + \frac{R_s}{R_c} \right) \right] \\
a_{22} &= \frac{9P}{4} \left[\begin{aligned} &- 2R_s (L_{ds} - L_{qs}) I'_{ds} + \omega_r^2 L_{ds} L_{qs} \frac{\lambda_m}{R_c} \left(1 + \frac{R_s}{R_c} \right) \\ &+ 2\omega_r^2 L_{ds}^2 L_{qs} I'_{ds} \frac{1}{R_c} \left(1 + \frac{R_s}{R_c} \right) - 2\omega_r^2 L_{ds}^2 \lambda_m \frac{1}{R_c} \left(1 + \frac{R_s}{R_c} \right) \\ &- 2\omega_r^2 L_{ds}^3 I'_{ds} \frac{1}{R_c} \left(1 + \frac{R_s}{R_c} \right) - R_s \lambda_m \end{aligned} \right]. \quad (7.51)
\end{aligned}$$

Solving Equations (7.48) and (7.50) for pI'_{qs} and pI'_{ds} , the following expressions are obtained:

$$pI'_{qs} = \frac{(a_{22}\sigma_\omega - a_{12}\sigma_\gamma)}{\Delta} = \sigma_{qs} \quad (7.52)$$

$$pI'_{ds} = \frac{(a_{22}\sigma_\omega - a_{12}\sigma_\gamma)}{\Delta} = \sigma_{qs} \quad (7.53)$$

where

$$\Delta = a_{11}a_{22} - a_{21}a_{12} \quad .$$

7.7 Controller Structure

The overall block diagram of the proposed control algorithm is shown in Figure 7.2. As the system is input-output linearizable, any dynamic can be imposed by means of a linear controller. An integrator-proportional (IP) controller is chosen as the linear controller in order to cancel any static error. Thus, the imposed linear control signals, σ_w

and σ_γ , is the output of the speed controller and total losses minimization controller.

Therefore, the proposed linear control law is, of the following form:

$$\sigma_w = (\omega_r^* - \omega_r)k_\omega - sk_{\omega 1}\omega_r = \frac{8Js^2\omega_r}{3P^2} \quad (7.54)$$

$$\sigma_\gamma = (\gamma^* - \gamma)\frac{k_{p\gamma}}{s} - \gamma k_{\gamma 1} = s\gamma \quad (7.55)$$

where ω_r^* represents the reference rotor speed, γ^* represents the total losses minimization reference; k_ω and $k_{\omega 1}$ are the speed controller gains; $k_{p\gamma}$ and $k_{\gamma 1}$ are the total losses minimization ($\gamma^*=0$) gains.

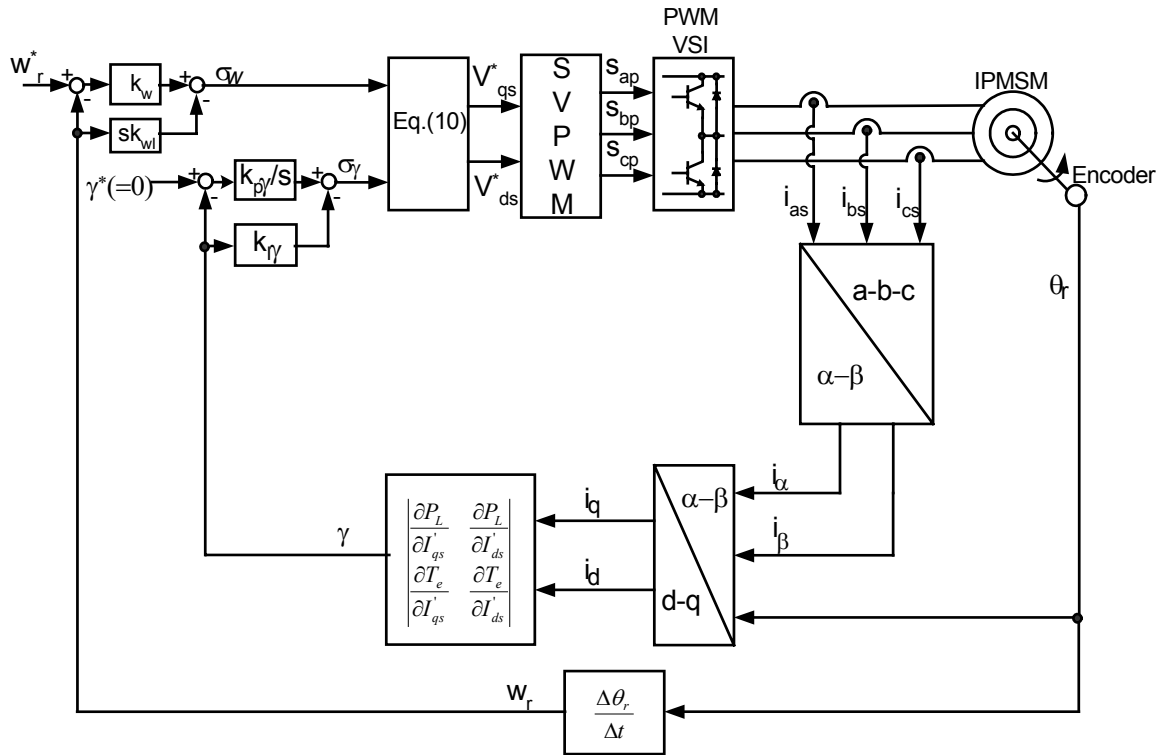


Figure 7. 2: Controller Structure for the IPM Motor Drive

However, the same controller structure can be used to implement torque control by changing the control variable from speed to torque and modify the output variable equations, respectively.

The transfer function of the closed-loop dynamics of each output of Figure 7.3 can be expressed as follows:

$$\frac{w_r}{w_r^*} = \frac{k_{wI}}{(8J/3P^2)p^2 + pk_{wI} + k_w} \quad (7.56)$$

$$\frac{\gamma}{\gamma^*} = \frac{k_{p\gamma}}{p^2 + pk_{\gamma I} + k_{p\gamma}} \quad (7.57)$$

The parameters of transfer functions k_{ω} , $k_{\omega I}$, $k_{p\gamma}$, and $k_{\gamma I}$ are chosen to optimize the closed-loop eigenvalue locations using the Butterworth polynomial. The Butterworth method locates the eigenvalues uniformly in the left-half S-plane on a circle of radius ω_0 (natural frequency), with its centre at the origin. The Butterworth polynomials for a transfer function with a second order denominator is given as

$$p^2 + 2\zeta\omega_0 p + \omega_0^2 = 0 \quad (7.58)$$

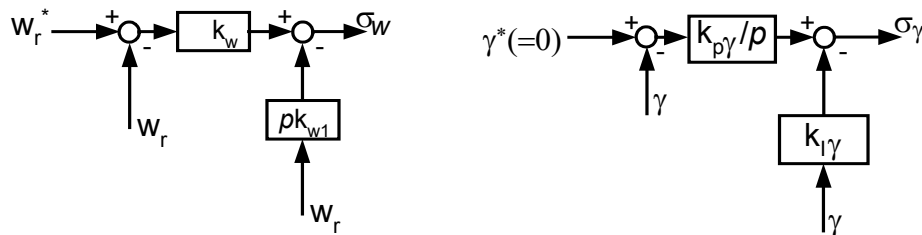


Figure 7.3: The structure of the Controllers

When the natural frequency ω_0 and damping ratio ζ in the feedback system in Figure 7.3 are designed, the PI gains are automatically determined by

$$k_{wI} = \omega_0 \zeta J / 3 \quad (7.59)$$

$$k_w = \omega_0^2 J / 6 \quad (7.60)$$

$$k_{\gamma I} = 2\omega_0 \zeta \quad (7.61)$$

$$k_{p\gamma} = \omega_0^2 \quad (7.62)$$

7.8 Simulation Results

The simulations for the minimization of total losses and minimization of copper losses (by making the core loss resistance infinite, $R_c = 10^6$) are done to compare the results of the two control schemes.

The inductances vary due to magnetic saturation, the L_{qs} , L_{ds} and λ_m , varies as a function of the armature current, Figure 7.5 shows the plot of these parameters against the peak stator current. The iron loss resistance R_c is dependent on the operating speed because the iron loss consists of hysteresis loss and eddy current loss, also at rated speed operating condition, the value of R_c changes with voltage as confirmed in chapter 6. However, a constant value of R_c (400 ohms) is used in these simulations.

Figure 7.6(i) shows the simulation results for the speed control and total loss minimization while Figure 7.6(ii) shows the results for the speed control and copper loss minimization. As shown in both results, the speed tracks its reference with little error, as

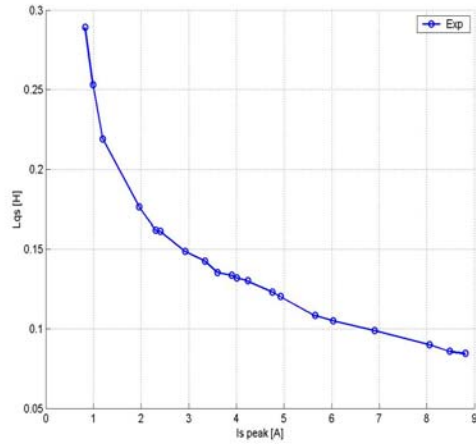
shown in Figure 7.7 (i) and Figure 7.7(ii). The loss minimization reference is zero, $\gamma^* = 0$, which is the second control variable, is found that the controller try to meet this constraint at all point when there is load (applied at 12.5sec) and without load. The error noticed in the simulation is found to be oscillating around the reference of zero, Figure 7.7 (i) and Figure 7.7(ii) shows this results; and when a step load is applied, the response of the controller was quite fast to go back to its reference. The total loss in the control scheme is reduced in Figure 7.6(i) compare to Figure 7.6(ii). The q- and d-axis current is also shown in Figure 7.6, and there is little difference in the stator current of the IPMSM. Figure 7.8 shows the online computation of the machine parameters, which is determined by the stator current at each time of the course of the simulation.

Figure 7.8 shows the q and d-axis voltages. Figure 7.8(ii) shows that more voltage is demanded by the scheme with copper loss minimization compare to the total loss minimization scheme in Figure 7.8(i).

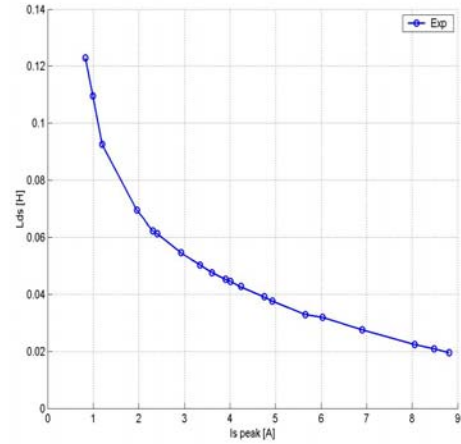
Figure 7.9 is the simulation results for the total loss minimization using constant machine parameters. Figure 7.9 confirms that the chattering and oscillations produce in Figures (7.5) – (7.8) are due to the effort of the controllers to instantaneously account for the varying machine parameters. And as shown in Figure 7.9, the two control variables did track their reference with little or no error produce at all times.

Using the same control structure, the speed reference is changed to torque; hence torque control scheme can be implemented along with the minimization of total losses, or copper losses minimization also refer to as torque per ampere operation by modifying the

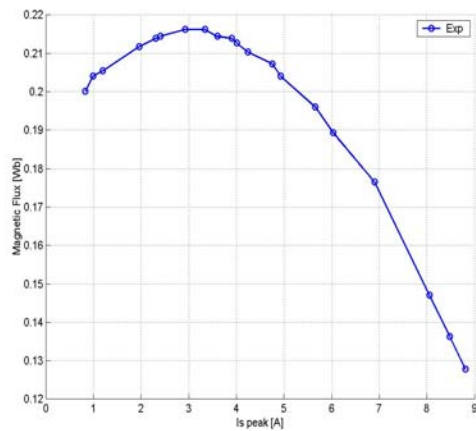
output variable (Equations 7.52 and 7.53). Figure 7.10-7.12 shows the simulation results for the torque control with varying parameters.



(a)

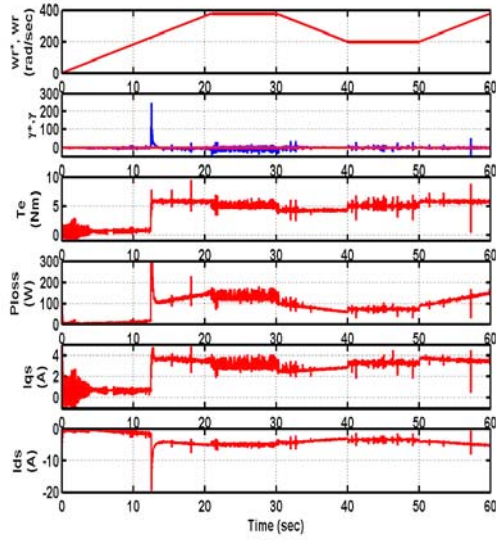


(b)

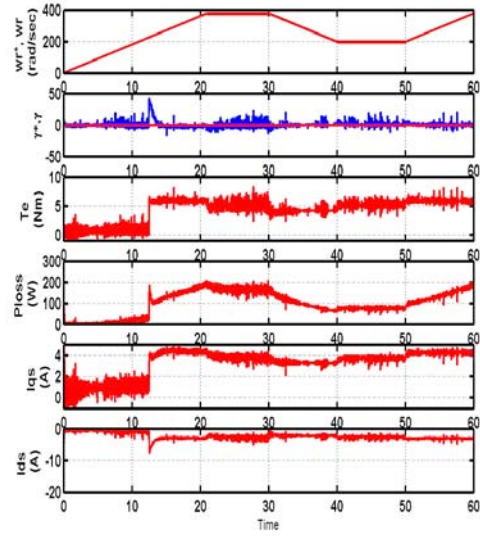


(c)

Figure 7. 4: Stator q and d axis inductances and magnet flux (a) L_q , (b) L_d , (c) λ_m

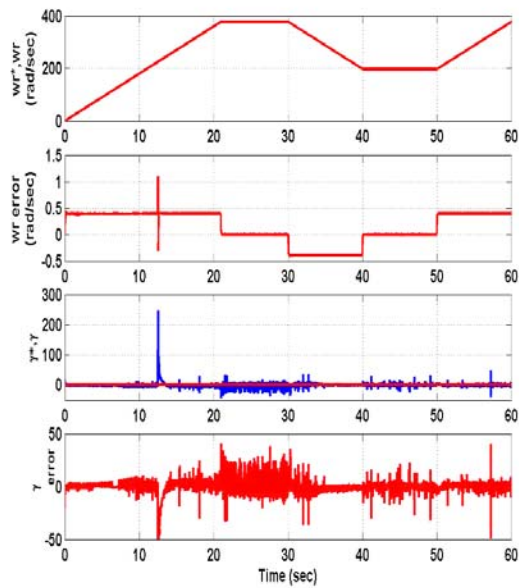


(i) Total loss minimization

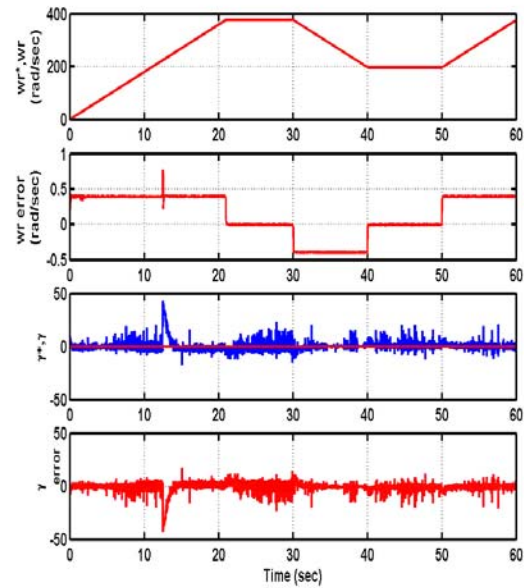


(ii) copper loss minimization

Figure 7. 5 Shows from top: (a) reference speed, and rotor speed, (b) γ^*, γ minimization constraint (c) electromagnetic torque, (d) total loss, (e) q-axis current, (f) d-axis current

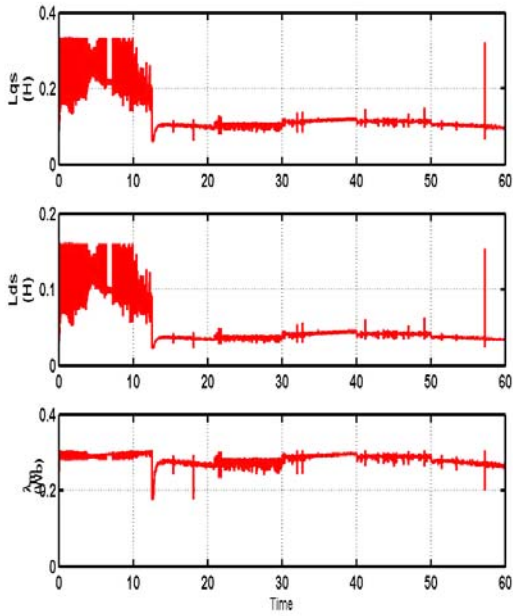


(i) Total loss minimization

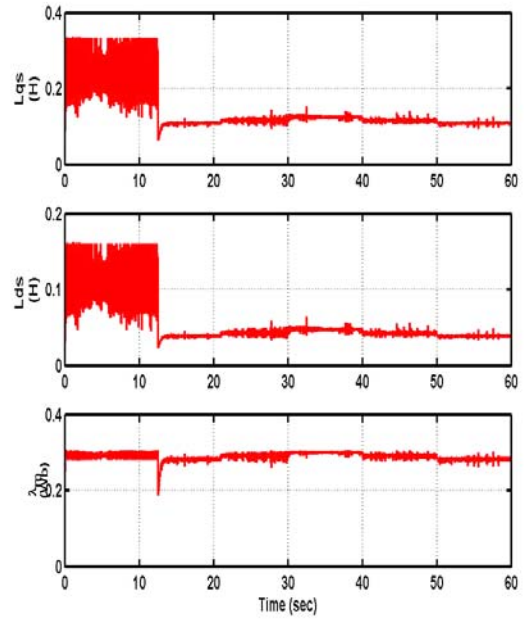


(ii) copper loss minimization

Figure 7. 6 Shows from top: (a)reference speed, and rotor speed, (b) speed error (c) γ^*, γ minimization constraint (d) minimization error

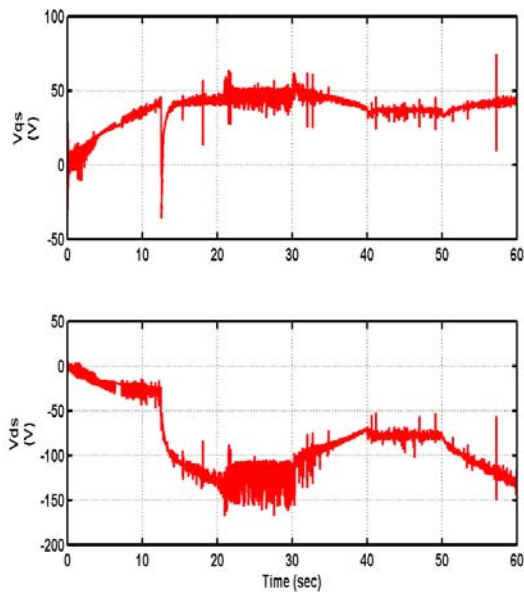


(i) Total loss minimization

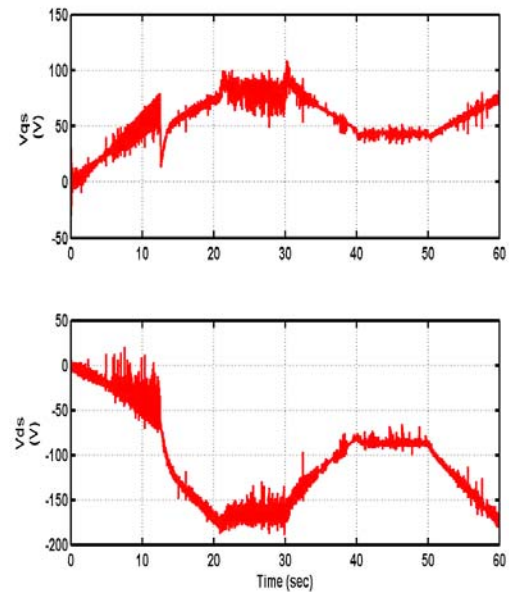


(ii) copper loss minimization

Figure 7. 7 shows from top: (a) q-axis inductance, (b) d-axis inductance (c) magnet flux



(i) Total loss minimization



(ii) copper loss minimization

Figure 7. 8 shows from top: (a)q-axis voltage, (b) d-axis voltage

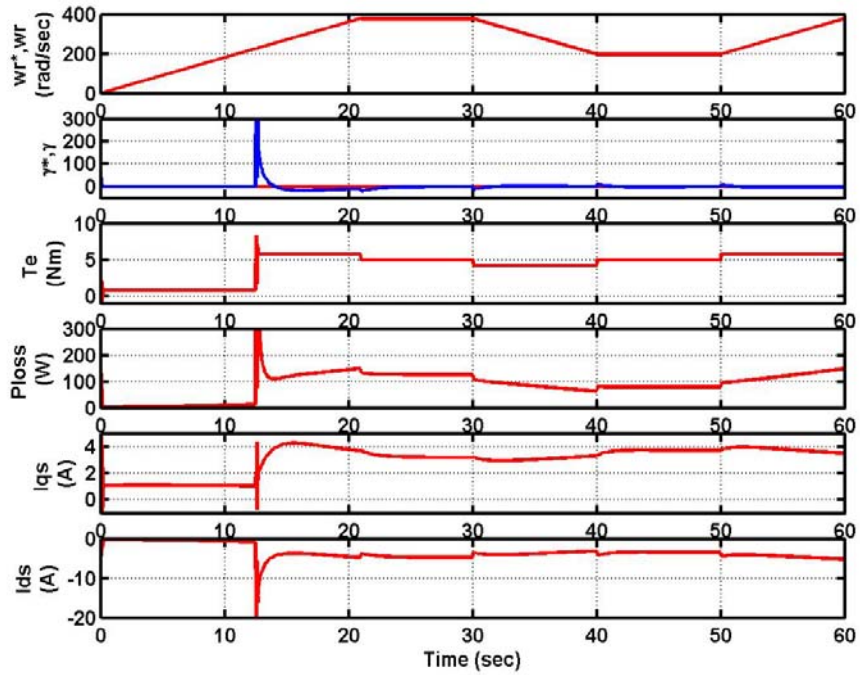
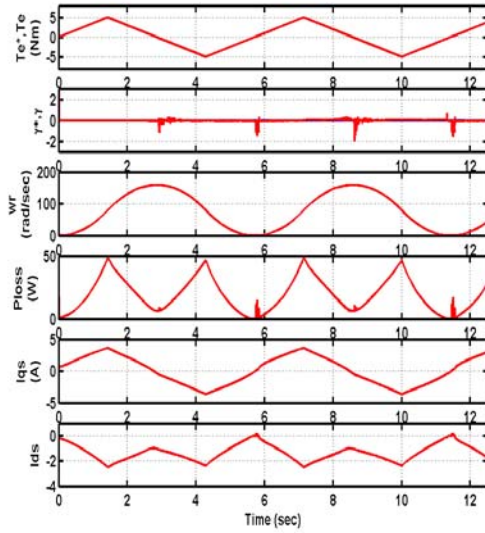
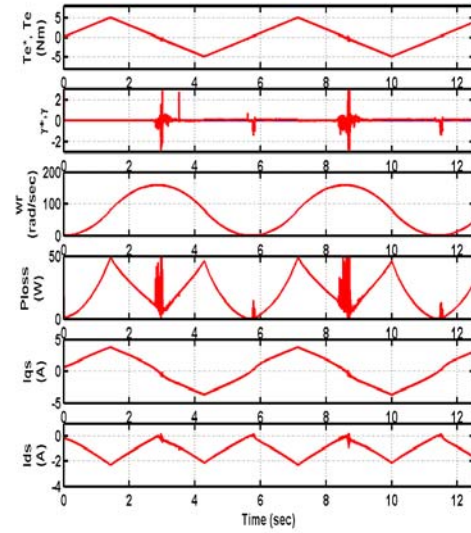


Figure 7. 9 shows total loss minimization control using constant parameters from top: (a) reference speed, and rotor speed, (b) γ^*, γ minimization constraint (c) electromagnetic torque, (d) total loss, (e) q-axis current, (f) d-axis current

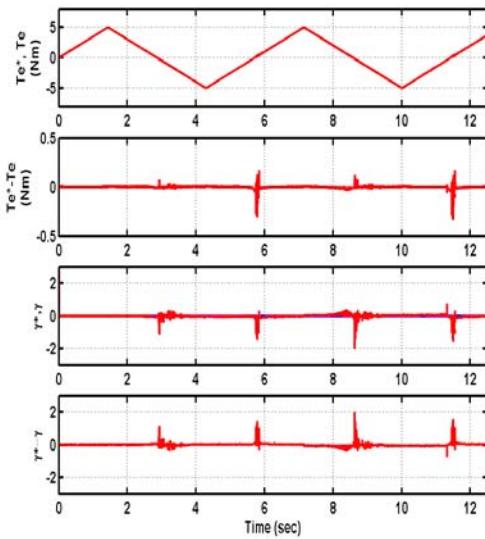


(i) minimum total loss

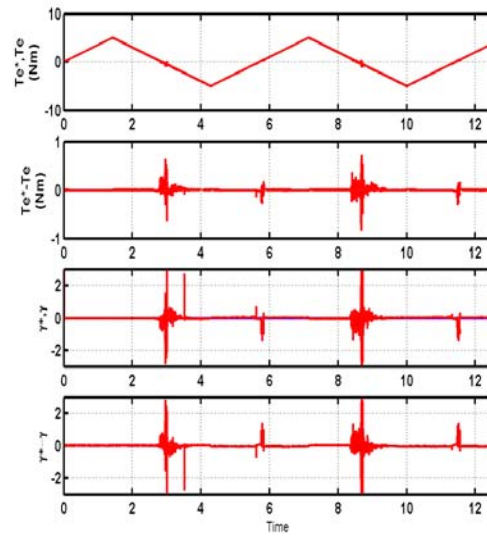


(ii) maximum torque per ampere

Figure 7. 10: Torque control and minimum total loss tracking of IPM motor drive, from top: (a) reference torque, and electromagnetic torque, (b) speed, (c) total loss, (d) q-axis current, (e) d-axis current

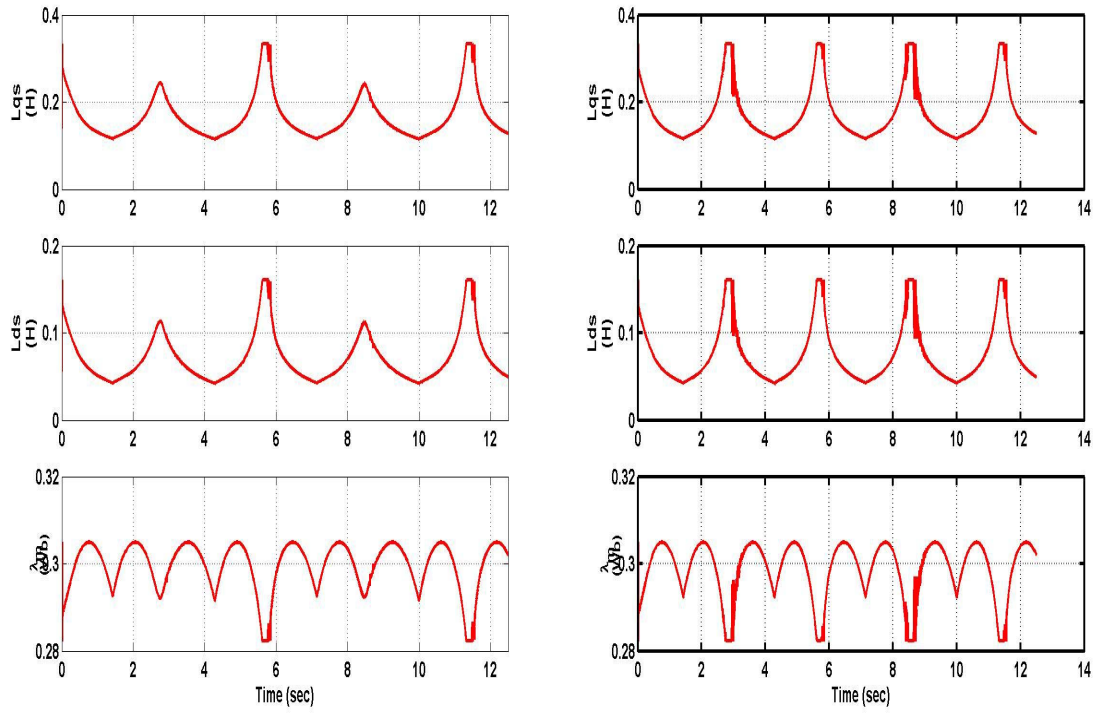


(i) minimum total loss



(ii) maximum torque per ampere

Figure 7. 11 shows from top: (a) reference torque, and electromagnetic torque, (b) torque error (c) γ^*, γ minimization constraint (d) minimization error



(i) minimum total loss

(ii) maximum torque per ampere

Figure 7. 12 shows from top: (a) q-axis inductance, (b) d-axis inductance (c) magnet flux

CHAPTER 8

CONCLUSIONS

An interior permanent magnet synchronous machine has been extensively analyzed during the course of this thesis research. Various fault situations on the interior permanent magnet synchronous machine and induction machine with the stator winding connected in star and delta form have been analyzed using a stationary reference frame. During the course of the research, it was found by simulation that delta-connected machines are more fault tolerant compared to star-connected machines. To some degree the machine was able to operate at rated speed with some oscillations despite the occurrence of a fault in one or more phases of the machine. The faults considered here are mainly either at the terminal of the machine or in the stator of the machine.

In the occurrence of a critical fault, such as the loss of one inverter phase leg, there might be a need to keep operation going instead of rendering the machine redundant. The modulation schemes of VSI-PWM were re-configured for the remaining two inverter phases while the third leg was replaced with a split DC capacitor. A balanced three-phase voltage was successfully generated without any loss of operation.

The influence of magnetic saturation and armature reaction on the performance of an interior permanent magnet including iron loss in the model was modeled. The iron loss resistance was found to be a function of the phase voltage which is rather varying instead of being constant as assumed in some literature. The efficiency of the machine is found to be improved which might be due to the saturation effects included in the computation.

The result is also validated by experimental results which shows similar trends of result observed in the computer simulation.

The parameter determination using finite element method shows similar results at high current with results earlier obtained from experimental method. The saturation nature of the parameters were observed using both methods, and it was shown that the parameters varies as a function of the stator current.

The last part of this work is on loss minimization which uses the input-output linearization techniques in the derivation of the control scheme. The IPM synchronous machine model includes the iron loss and saturation effects of the parameters in its implementation. It was shown that some level of improvement was obtained by minimizing the total loss compared to the torque per ampere operation. The last part of this work is the experimental validation of the simulation which is in progress.

REFERENCES

- [1] R. Krishnan, *Electric Motor Drives: modeling, analysis, and control*, Prentice Hall, Upper Saddle River, NJ, 2001.
- [2] T.M. Jahns, G.B. Kliman, and T.W. Neumann, "Interior permanent-magnet synchronous motor for adjustable-speed drives," *IEEE Transactions on Industry Applications*, vol. IA-22, pp.738-747, July/Aug. 1986.
- [3] V. B. Honsinger, "The fields and parameters of interior type ac permanent magnet machines," *IEEE Transactions on Power Apparatus and Systems*, PAS-101, vol. 4, pp. 867-875, 1982.
- [4] A. Consoli and G. Renna, "Interior type permanent magnet synchronous motor analysis by equivalent circuits," *IEEE Transactions on Energy Conversion*, vol. 4, no. 4, pp. 681-689, December 1989.
- [5] B. J. Chalmers, S.A. Hamed, and G.D. Baines, "Parameters and performance of a high-field permanent-magnet synchronous motor for variable-frequency operation," *IEE Proceedings*, vol. 132, pt B, no. 3, page 117-124, May 1985.
- [6] B. J. Chalmers, "Performance of Interior-Type permanent-magnet alternator," *IEE Proceedings Electric Power Applications*, vol. 141, no. 4, page 186-190, July, 1994.
- [7] C. D. Dicenzo, H. Ahmad and N.K. Sinha, "Optimum design of permanent generators for control applications," *IEEE Transactions on Industrial Electronics and Control Instrumentation*, vol. IECI-22, no. 2, page 214-218, May, 1975.
- [8] K. J. Binns, and W. R. Barnard, "Computation of the magnetic field of permanent magnets in iron cores," *IEE Proceedings*, vol. 122, no. 12, page 1377-1381, December, 1975.
- [9] R. Schiferl, *Design considerations for salient-pole permanent magnet synchronous motors in variable-speed drive applications*, PhD Thesis, University of Wisconsin-Madison, 1987.
- [10] R. Rabinovici, "Magnetic field analysis of permanent magnet motor," *IEEE Transactions on Magnetics*, vol. 32, no. 1, page 267-270, January, 1996.
- [11] N. A. O. Demerdash and M. A. Alhamadi, "Three-dimensional finite element analysis of permanent magnet brushless DC motor drives-status of the state of the art," *IEEE Transactions on Industrial Electronics*, vol. 43, no. 2, page 268-276, April, 1996.

- [12] L. H. Lewis, J. Gao, D.C. Jiles, and D.O Welch, "Modeling of permanent magnets: Interpretation of parameters obtained from the Jiles-Atherton hysteresis model," *Journal of Applied Physics*, vol. 79, no. 8, page 6470-6473, April, 1996.
- [13] M. A. Rahman and A. M. Osheiba, "Effect of parameter variations on the performance of permanent magnet motors," *IEEE Industrial Applications Society Annual Meeting Conference Record*, 1986, pp. 787-793.
- [14] R. Schiferl and T. A. lipo, "Power capability of salient-pole permanent magnet synchronous motors in variable speed drive applications," *IEEE Industrial Applications Society Annual Meeting Conference Record*, 1988, pp. 23-31.
- [15] A. Consoli and A. Raciti, "Analysis of permanent magnet synchronous motors," *IEEE Transactions on Industry Applications*, vol. 27, no. 2, pp. 350-354, Mar./Apr. 1991.
- [16] R. Schiferl and T. A. lipo, "Core loss in buried magnet permanent magnet synchronous motors," *IEEE Transactions on Energy Conversion*, vol. 4, no. 2, pp. 279-284, June 1989.
- [17] S. Morimoto, Y. Tong, Y. Takeda, and T. Hirasu, "Loss minimization control of permanent magnet synchronous motor drives," *IEEE Transactions on Industrial Electronics*, vol. 41, no. 5, pp. 511-517, Oct. 1994.
- [18] S. Vaez – Zadeh, "Variable flux control of permanent magnet synchronous motor drives fo constant torque operation," *IEEE Transactions on Power Electronics*, vol. 16, no. 4, pp. 527-534, July 2001.
- [19] C. Mademlis and N. Margaris, "Loss minimization in vector-controlled interior permanent magnet synchronous motor drives," *IEEE Transactions on Industrial Electronics*, vol. 49, no. 6, pp. 1344-1347, December 2002.
- [20] I. Kisheridis and C. mademlis, "Energy efficiency optimization in synchronous reluctance motor drives," *IEE Proceedings – Electric Power Applications*, vol. 150, no. 2, pp. 201-209, March 2003.
- [21] N. Urasaki, T. Senjyu, and K. Uezato, "Investigation of influences of various losses on electromagnetic torque for surface-mounted permanent magnet synchronous motors," *IEEE Transactions on Power Electronics*, vol. 18, no. 1, Jan. 2003.
- [22] A. Jack and M. C. Mecrow, "A comparative study of permanent magnet and switched reluctance motors for high performance fault-tolerant applications," *IEEE Transactions on Industry Applications*, vol. 32, no. 4, pp. 889-895, July/August 1996.

- [23] B. Welchiko and T. Jahns, "IPM synchronous machine drive response to a single-phase open circuit," Conference Proceedings of the 16th Annual Applied Power Electronics Conference, pp. 421-427, March 2001.
- [24] N. Bainchi and S. Bolognani, "Analysis of PM synchronous motor drives during flux weakening operation," Proceedings of the IEEE Power Electronics Specialist Conference, pp. 1542-1548, June 1996.
- [25] S. Bolognani, M. Zordan, M. Zigliotto, " Experimental fault tolerant control of PMSM drive," IEEE Transactions on Industrial Electronics, vol. 47, no. 5, pp. 1134- 1141, October 2000.
- [26] R. Spee and A. K. Wallace, "Remedial strategies for brush-less DC drive failures," IEEE Transactions on Industry Applications, vol. 27, pp. 259-266, March/April 1990.
- [27] R. J. Kerkman, "Machine analysis with unbalanced terminal constraints by d-q harmonic balance," IEE Proceedings, vol. 128, Part B, no. 6, pp.343-357, November 1981.
- [28] R. J. Kerkman, P. C. Krause and T. A. Lipo, " Simulation of a synchronous machine with an open phase," Electric Machines and Electro mechanics, vol. 1, pp. 245-254, 1977.
- [29] A. Consoli and T. A. Lipo, "Orthogonal axis models for asymmetrical connected induction machines," IEEE Transactions on Power Apparatus and Systems, vol. PAS-101, no. 12, pp. 4518-4526, December 1982.
- [30] G. Kim and T.A. Lipo, "VSI-PWM rectifier/inverter system with a reduced switch count," IEEE Transactions on Industrial Applications, vol. 32, no. 6, pp. 1331-1337, Nov./Dec. 1996.
- [31] G. L. Peters, G. A. Covic and J. T. Boys, "Eliminating output distortion in four-switch inverters with three-phase loads," IEE Proceedings - Electric Power Applications, vol. 145, Part B, no. 4, pp. 326-332, July 1998.
- [32] C. B. Jacobiana, M. B. de Rossiter Correa, E. R. C. da Silva, and A. M. N. Lima, " Induction motor drive system for low power applications," IEEE Transactions on Industry Applications, vol. 35, no. 1, pp. 52-60, Jan./Feb. 1999.
- [33] S. R. MacMinn, T. M. Jahns, "Control techniques for improved high-speed performance of interior permanent motor drives," IEEE Transactions on Industry Applications, vol. 27, no. 5, pp. 997 - 1004, September/October 1991.

- [34] T. H. Liu, J. R. Fu, and T. A. Lipo, "A strategy for improving reliability of field-oriented controlled induction motor drives," *IEEE Transactions on Industry Applications*, vol. 29, pp. 910-918, Sept./Oct. 1993.
- [35] A. Kusko and D. Galler, "Control means for minimization of losses in ac and dc motor drives," *IEEE Transactions on Industry Applications*, vol. IA-19, pp. 561-570, July/Aug. 1983.
- [36] R. S. Colby and D. W. Novotny, "Efficient operation of surface mounted PM synchronous motors," *IEEE Transactions on Industry Applications*, vol. IA-23, pp. 1048-1054, Nov./Dec. 1987.
- [37] S. Morimoto, Y. Takeda, and T. Hirasu, "Current phase control methods for permanent magnet synchronous motors," *IEEE Transactions on Power Electronics*, vol. 5, pp.133-139, Apr. 1990.
- [38] B. Sneyers, D.W. Novotny, and T.A. Lipo, "Field weakening in buried magnet ac motor drives," *IEEE Transactions on Industry Applications*, vol. IA-21, pp. 398-407, Mar./Apr. 1985.
- [39] T. M. Jahns, "Flux-weakening regime operation of an interior permanent-magnet synchronous motor drives," *IEEE Transactions on Industry Applications*, vol. IA-23, pp.681-689, July/Aug. 1987.
- [40] B. K. Bose, "A high performance inverter-fed drive system of an interior permanent magnet synchronous machine," *IEEE Transactions on Industry Applications*, vol. IA-24, pp.987-997, Nov./Dec. 1988.
- [41] S. Morimoto, Y. Takeda, T. Hirasu, and K. Taniguchi, "expansion of operating limits for permanent magnet motor by current vector control considering inverter capacity," *IEEE Transactions on Industry Applications*, vol. 26, pp. 866-871, Sept./Oct. 1990.
- [42] A. Isidori, *Nonlinear Control Systems, an Introduction*. Berlin, Germany: Springer-Verlag, 1985.
- [43] B. K. Bose, "Technology trends in microcomputer control of electrical machines," *IEEE Transactions on Industrial Electronics*, vol. 35, pp. 160-177, Feb. 1988.
- [44] H. Le-Huy, "Microprocessor and digital IC's for motion control," *Proc. IEEE*, vol. 82, pp. 1140-1163, Aug. 1994.

- [45] A. Kaddouri, O. Akhrif, H. Le Huy, and M. Ghribi, "Nonlinear feedback control of permanent magnet synchronous motors," in Proceedings 1994 Canadian Conference Electrical and Computer Engineering, Halifax, N.S., Canada, Sept. 25-28, 1994, pp. 77-80.
- [46] B. Le Pioufle, "Comparison of speed nonlinear control strategies for the synchronous servo-motor," *Elec. Mech. Power Syst.*, vol. 21, pp. 151-169, 1993.
- [47] M. Zribi and J. Chiasson, "Position control of a PM stepper motor by exact linearization," *IEEE Transactions on Automatic Control*, vol. 36, pp. 620-625, May 1991.
- [48] M. Bodson, J.N. Chiasson, R.T. Novotnak, and R.B. Rekowski, "High-performance nonlinear feedback control of a permanent magnet stepper motor," *IEEE Transactions on Control System Technology*, vol. 1, pp. 5-13, Mar. 1993.
- [49] M. Illic-Spong, R. Marino, S. Peresada, and D. Taylor, "Feedback linearizing control of switched reluctance motors," *IEEE Transactions on Automatic Control System Technology*, vol.32, pp. 371-379, May 1987.
- [50] A. De Lucas and G. Ulivi, "Full linearization of induction motor via nonlinear state feedback," in Proceedings 26th IEEE Conf. Decision and Control, Los Angeles, CA, 1987, pp. 1765-1770.
- [51] D. Taylor, "Nonlinear control of electric machines: An overview," *IEEE Transactions Control System Technology*, vol. 2, pp. 41-51, Dec. 1994.
- [52] S. H. Chu and I. J. Ha, "Control of hybrid step motors via a simplified linearization technique," *International Journal of Control*, vol. 61, no. 5, pp. 1143-1167, May, 1995.
- [53] H. Le-Huy, K. Slimani, and P. Viarouge, "Analysis and implementation of a real-time predictive current controller for permanent magnet synchronous servo drive," *IEEE Transactions on Industrial Electronics*, vol. 41, pp. 110-117, Feb. 1993.
- [54] P. Pillay and R. Krishnan, " Modeling, simulation and analysis of permanent magnet motor drives, part 1: The permanent-magnet synchronous motor drive," *IEEE Transactiona on Industry Applications*, vol. 25, pp. 265-273, Mar./Apr. 1989.
- [55] L. Xu, X. Xu, T. A. Lipo, and D. W. Novotny, "Vector control of a synchronous reluctance motor including saturation and iron losses," *IEEE Transactions on Industry Applications*, vol. 27, pp. 977-984, Sept./Oct. 1991.

- [56] L. Xu and J. Yao, "A compensated vector control scheme of a synchronous reluctance motor including saturation and iron losses," *IEEE Transactions on Industry Applications*, vol. 28, pp. 1330-1338, Nov./Dec. 1992.
- [57] K. Uezato, T. Senjyu, and Y. Tomori, "Modeling and vector control of synchronous reluctance motors including stator iron loss," *IEEE Transactions on Industry Applications*, vol. 30, pp. 971-976, July/Aug. 1994.
- [58] S.J. Kang and S.K. Sul, "Highly dynamic torque control of synchronous reluctance motor," *IEEE Transactions on Power Electronics*, vol. 13, pp. 793-798, July 1998.
- [59] A. Vagati, M. Pastorelli, G. Franceschini, and V. Drogoreanu, "Flux-observer-based high-performance control of synchronous reluctance motors by including cross saturation," *IEEE Transactions on Industry Applications*, vol. 35, pp. 597-605, May/June 1999.
- [60] H.D. Lee, S.J. Kang, and S.K. Sul, "Efficiency-optimised direct torque control of synchronous reluctance motor using feedback linearization," *IEEE Transactions on Industrial Electronics*, vol. 46, pp. 192-198, Feb. 1999.
- [61] E. Levi, "Impact of iron loss on behavior of vector controlled induction machines," *IEEE Transactions on Industry Applications*, vol. 31, pp. 1287-1296, Nov./Dec. 1995.
- [62] E. Levi, M. Sokola, A. Boglietti, and M. Patorelli, "Iron loss in rotor-flux-oriented induction machines: Identification, assessment of detuning, and compensation," *IEEE Transactions on Power Electronics*, vol. 11, pp. 698-709, Sept. 1996.
- [63] T. Mizuno, J. Takayama, T. Ichioka, and M. Terashima, "Decoupling control method of induction motor taking stator core loss into consideration," in *Proceedings IPEC'90 Conference, Tokyo, Japan, 1990*, pp. 69-74.
- [64] J. Jung and K. Nam, "A vector control scheme for EV induction motors with a series iron loss model," *IEEE Transactions on Industrial Electronics*, vol. 45, pp. 617-624, Aug. 1998.
- [65] T. Senjyu, T. Shimabukuro, and K. Uezato, "Vector control of synchronous permanent magnet motors including stator iron loss," *International Journal of Electronics*, vol. 80, no. 2, pp. 181-190, 1996.
- [66] J. Kim and S. Sul, "Speed control of interior permanent magnet synchronous motor drive for the flux weakening operation", *IEEE Transactions on Industry Applications*, vol. 33, no. 1, pp. 43 - 48, January/February 1997.

- [67] H. Kim, J. Hartwig, R. D. Lorenz, “Using on-line parameter estimation to improve efficiency of IPM motor drives”, Conference Record of the 2002 IEEE-Power Electronics Specialist Conference, pp. 815 – 820, June 23-27th, 2002.
- [68] H. Kim and R. D. Lorenz, “Improved current regulators for IPM machine drives using on-line parameter estimation”, Conference Record of the 37th IAS Annual Meeting of the IEEE Industry Applications Society, pp. 86 – 91, October 13-18th, Oct. 2002.
- [69] R. E. Betz, R. Lagerquist, M. Jovanovic, T. J. E. Miller, and R. H. Middleton, “Control of synchronous reluctance machines,” IEEE Transactions on Industry Applications, vol. 29, no. 6, Nov./Dec. 1993.
- [70] J. D. Cox, Analysis of an interior permanent magnet machine operating in generator mode, MSc Thesis, Tennessee Technological University, 1996.
- [71] D. Grenier, L.A. Dessaint, O. Akhrif, Y. Bonnassieux, and B. Le Pioufle, “Experimental nonlinear torque control of a permanent magnet synchronous motor using saliency,” IEEE Transactions on Industrial Electronics, vol. 44, no. 5, Oct. 1997.
- [72] P. Vas, *Sensor-less Vector and Direct Torque Control*, Oxford University Press, New York, 1998.
- [73] P. C. Krause, *Analysis of Electric Machinery*, McGraw-Hill Publisher, New York, 1986.
- [74] P. C. Krause and C. H. Thomas, “Simulation of Symmetrical Induction Machinery,” IEEE Transactions on Power Apparatus and Systems, Vol. 84, pp. 1038-1053, November 1965.
- [75] L. J. Jacovides, “Analysis of induction motors with non-sinusoidal supply voltages using Fourier analysis,” IEEE Transactions on Industry Applications, Vol. IA-9, pp. 741-747, Nov/Dec 1973.
- [76] E. A. Klingshrin and H.E. Jordan, “Polyphase induction motor performance and losses on non- sinusoidal voltage supplies,” IEEE Transactions on Power Apparatus and Systems, Vol. PAS-87, pp. 624-631, March 1968.
- [77] S. R. Bowes and J. Clare, “Steady-state performance of PWM inverter drives,” Proceedings of the Institution of Electrical Engineers (IEE), Vol. 130, Part B, pp. 229-244, July 1983.

- [78] N. R. Namburi and Thomas Barton, "Time domain response of induction motors with PWM supplies," IEEE Transactions on Industry Applications, Vol. IA-21, pp. 448-455, March/April 1985.
- [79] T.J.E. Miller, "Method for testing permanent magnet polyphase AC motors," in Conference Record IEEE-IAS Annual Meeting, 1981, pp. 494-499.
- [80] J. Slotine and W. Li, **Applied Nonlinear Control**, Prentice-Hall, New York, 1991.
- [81] B. Friedland, **Control System Design, An Introduction to State-Space Methods**, McGraw- Hill, New York, 1986.
- [82] O. Ojo, "Field orientation control of a doubly-fed synchronous reluctance machine," Conference Record of the 29th Annual IEEE PESC Conference, pp. 1276-1282, 1998.
- [83] S. Monaco, D. Normand-Cyrot, and A. Chelouah, "Digital nonlinear speed regulation of a synchronous motor," Automation and remote control, vol. 58, no. 6, pp. 1003-1016, 1997.
- [84] S. Di Gennaro, "Adaptive output feedback control of synchronous motors," International Journal of Control, vol. 73, no. 16, pp. 1475-1490, 2000.
- [85] G. Zhu, A. Kaddouri, L. -A. Dessaint, and O. Akhrif, " A nonlinear state observer for the sensorless control of a permanent magnet AC machine," IEEE Transactions on Industrial Electronics, vol. 48, no. 6, Dec. 2001.
- [86] T. G. Park and K. S. Lee, "SMC-based adaptive input-output linearizing control of induction motors," IEE Proceedings Control Theory Application, vol. 145, no. 1, pp. 55-61, January 1998.
- [87] M. Tarbouchi and H. Le-Huy, "High-performance control by input-output linearization technique of an induction motor," IEEE Industry Application Annual Meeting, New York, pp. 373-378, 1996.
- [88] M. P. Kazmierkowski, R. Krishnan, and F. Blaabjerg, **Control in Power Electronics: Selected Problems**, Academic Press, California, 2002.

APPENDIX A

PARAMETERS AND MATERIAL CHARACTERISTICS OF THE TWO

HORSEPOWER, BURIED MAGNET TEST MOTOR

A.1 Motor Rating

A two horsepower, line-start, buried magnet, permanent magnet synchronous motor was tested in order to compare measured data with calculated results. The nameplate data for the test motor is given in Table A.1

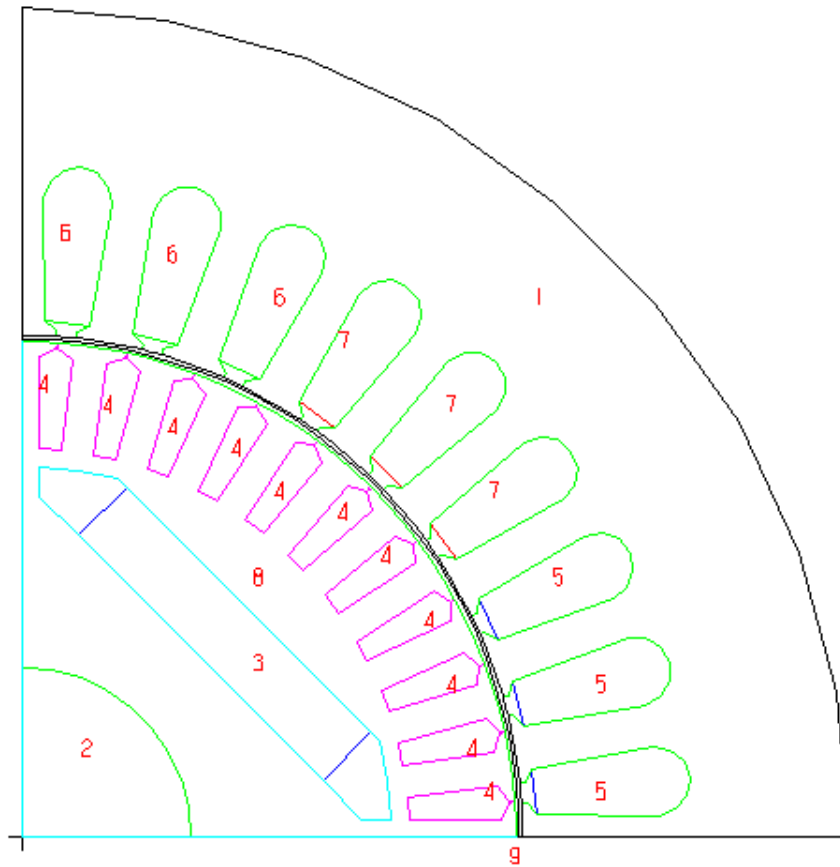
Table A. 1: Nameplate data for the two horsepower buried magnet test machine.

GENERAL DATA

Rated Output Power (kW):	1.492
Rated Voltage (V):	230
Number of Poles:	4
Frequency (Hz):	60
Frictional Loss (W):	15
Winding Connection:	Wye
Operating Temperature (C):	40

A.2 Motor Geometry

A cross section of one pole of the test motor showing the material types of various regions is given in Figure A.1. The motor has rectangular samarium cobalt permanent magnets. The rotor contains a cast aluminum starting cage which lies in slots above the magnets. Stator dimension and rotor damper dimension (and winding data, slot dimensions) are listed in Table A.2 and Table A.3, respectively. Figure A.2 and Figure A.3 shows the stator and rotor slot dimensions respectively.



Materials

1. Stator iron
2. Solid iron shaft
3. Permanent magnet
4. Rotor conductors
5. "A" phase conductors
6. "B" phase conductors
7. "-C" phase conductors
8. Rotor iron
9. Air gap

Figure A. 1 One pole cross section of a four pole, buried magnet, permanent magnet synchronous machine showing material boundaries.

Table A. 2: Stator Dimensions.

STATOR DATA

Outer Diameter of Stator (mm):	154.432
Inner Diameter of Stator (mm):	93.4212
Number of Stator Slots:	36
Skew Width (Slots):	1
Type of Stator Slot:	2
Stator Slot Dimensions	
Hs0 (mm):	0.508
Hs1 (mm):	0.762
Hs2 (mm):	11.43
Bs0 (mm):	1.9304
Bs1 (mm):	4.191
Bs2 (mm):	6.39572
Top Tooth Width (mm):	4.18319
Bottom Tooth Width (mm):	3.97339
Length of Stator Core (mm):	95.25
Stacking Factor of Stator Core:	0.93
Type of Steel:	STATOR_DEF
Slot Insulation Thickness (mm):	0.3
End Length Adjustment (mm):	0
Number of Parallel Branches:	1
Number of Conductors per Slot:	24

Winding Type:	12
Average Coil Pitch:	9
Number of Wires per Conductor:	5
Wire Diameter (mm):	0.6438
Wire Wrap Thickness (mm):	0
Stator Slot Fill Factor (%):	74.5748
Coil Half-Turn Length (mm):	220.87

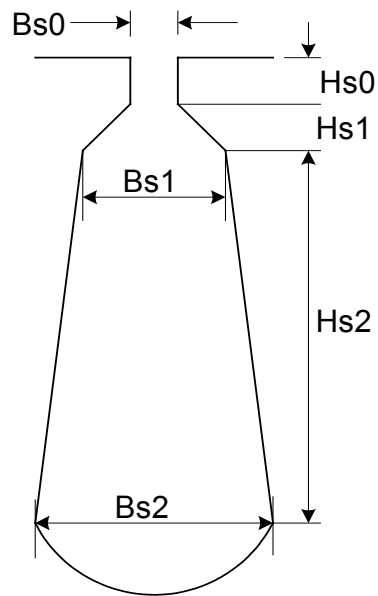


Figure A. 2: Stator slot dimensions of the buried magnet test motor.

Table A. 3: Damper Data

Damper Slots per Pole:	11
Type of Damper Slot:	3
Damper Slot Dimensions	
Hr0 (mm):	0.508003
Hr1 (mm):	0.888997
Hr2 (mm):	8.50902
Br0 (mm):	0.045
Br1 (mm):	3.175
Br2 (mm):	2.03199
Rr (mm):	0
End Length of Damper Bars (mm):	2.00001
End Ring Width (mm):	3.99999
End Ring Height (mm):	29.9999
Resistivity of Dampers	
at 75 Centigrade (ohm.mm ² /m):	0.017

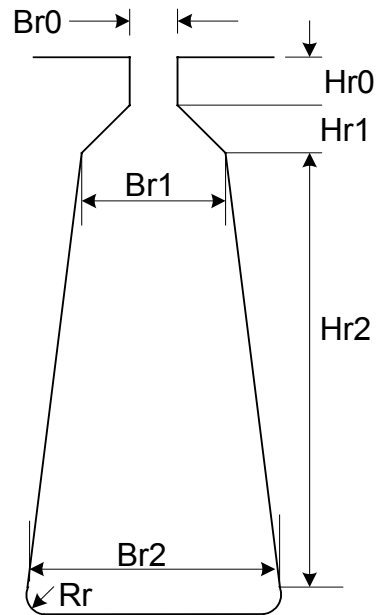


Figure A. 3: Rotor slot dimensions of the buried magnet test motor.

A.3 Material Characteristics

The finite element method using RMxpert software requires input material characteristics for all magnetic materials in the motor cross section. All linear materials (air gap, rotor slots and stator windings) were assigned the permeability of free space. The rotor overall dimensions and the samarium cobalt magnet was modeled as shown in Table A.4 and Table A.5 respectively. Figure A.4 shows the buried magnet duct dimension as laid in the rotor of the machine.

Figure A.5 (referred to as STATOR_DEF IN Table A.4) and Figure A.6 shows the plot of the stator and shaft lamination steel BH input data. The rotor and stator BH characteristics were assumed to be the same.

Table A. 4: Rotor Data

Air Gap (mm):	0.635
Inner Diameter of Rotor (mm):	31.496
Length of Rotor (mm):	95.25
Stacking Factor of Rotor Core:	0.93
Type of Steel:	STATOR_DEF
Type of Rotor:	4
Magnet Duct Dimensions	
D1 (mm):	69.073
O1 (mm):	23.5331
Rib (mm):	3.302
Magnet Type:	Samarium Cobalt
Magnet Thickness (mm):	6.35
Total Magnet Width (mm):	32.3088

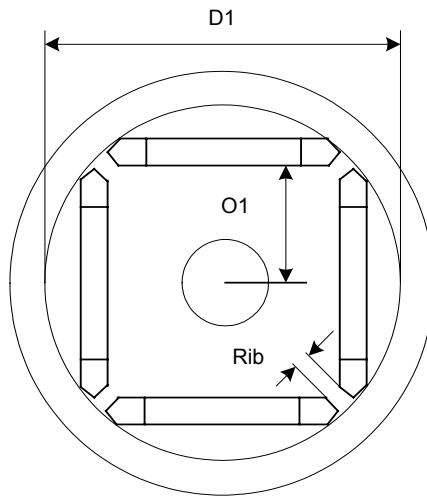


Figure A. 4: Magnet duct dimensions of the buried magnet test motor.

Table A. 5 Permanent Magnet Data

Residual Flux Density (Tesla):	0.85
Coercive Force (kA/m):	629
Maximum Energy Density (kJ/m ³):	133.67
Relative Recoil Permeability:	1.07528
Demagnetized Flux Density (Tesla):	0.531245
Recoil Residual Flux Density (Tesla):	0.849979
Recoil Coercive Force (kA/m):	629.055

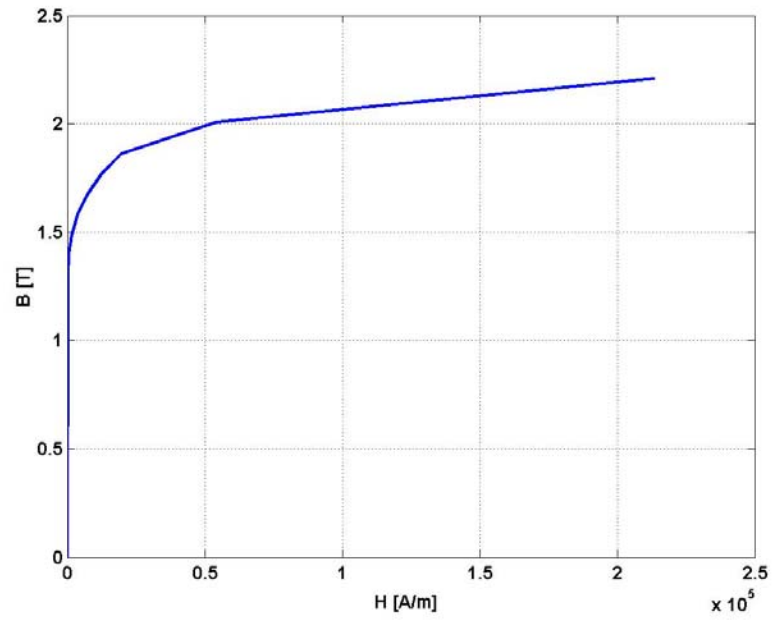


Figure A. 5: Stator and rotor lamination steel BH curve

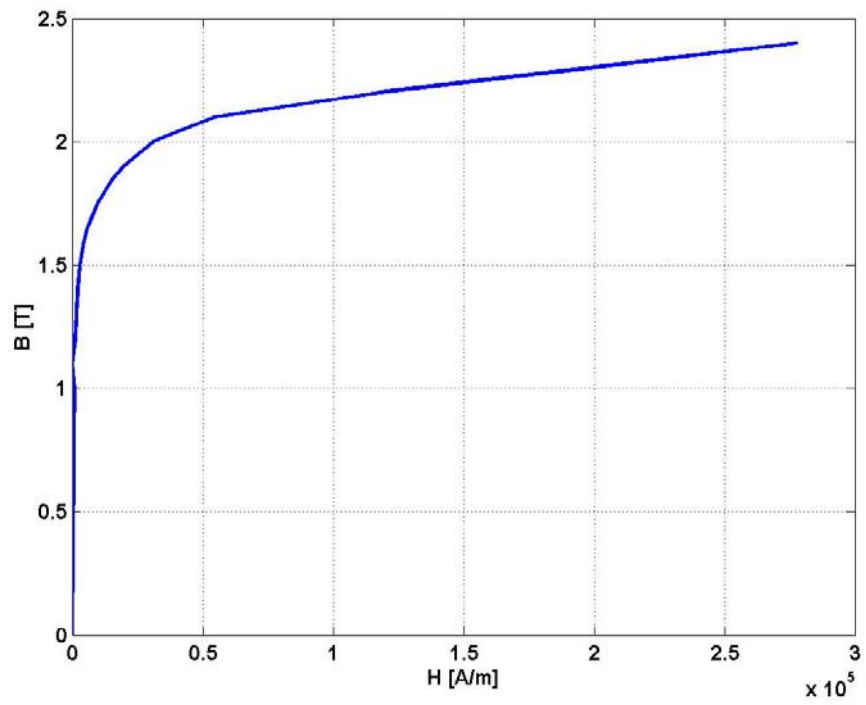


Figure A. 6: Solid rotor shaft BH curve (Stator_def)

VITA

Olufemi Osaloni was born in Owerri, Imo state, Nigeria, in 1975. He attended primary schools in Agege and Mushin, Lagos state, Nigeria, from 1980-1986. He graduated from Idi-Araba High School, Mushin, Lagos State, Nigeria, in 1992. He obtained Bachelor of Science degree in Electronic and Electrical Engineering at Obafemi Awolowo University, Ile-Ife, Osun State, Nigeria, in December 1998. After completing his National Youth Service Corps (NYSC) in Lagos State, he entered the graduate school at Obafemi Awolowo University as a Graduate Assistant in February 2000, and later got admission into Tennessee Technological University in August 2001 and is a candidate for Masters of Science degree in Electrical Engineering. His research interests include Power Electronics; Electric Motor Drives; Electric Machines Modeling, Analysis, Design, and Control; and Control Theory application to Power Electronics and Power Systems.